



HAL
open science

On the mechanisms resulting in the formation of the Quaternary staircase terrace systems in the valleys of the western Andean margin of Peru

Fritz Schlunegger, Ariel Do Prado, Kevin Norton, Romain Delunel

► **To cite this version:**

Fritz Schlunegger, Ariel Do Prado, Kevin Norton, Romain Delunel. On the mechanisms resulting in the formation of the Quaternary staircase terrace systems in the valleys of the western Andean margin of Peru. *Geomorphology*, In press, 10.1016/j.geomorph.2023.108923 . hal-04229034

HAL Id: hal-04229034

<https://hal.science/hal-04229034v1>

Submitted on 5 Oct 2023

HAL is a multi-disciplinary open access archive for the deposit and dissemination of scientific research documents, whether they are published or not. The documents may come from teaching and research institutions in France or abroad, or from public or private research centers.

L'archive ouverte pluridisciplinaire **HAL**, est destinée au dépôt et à la diffusion de documents scientifiques de niveau recherche, publiés ou non, émanant des établissements d'enseignement et de recherche français ou étrangers, des laboratoires publics ou privés.

1 **On the mechanisms resulting in the formation of the Quaternary staircase**
2 **terrace systems in the valleys of the western Andean margin of Peru**

3

4 Fritz Schlunegger

5 Institute of Geological Sciences

6 University of Bern

7 fritz.schlunegger@geo.unibe.ch

8

9 Ariel do Prado

10 Institute of Geological Sciences

11 University of Bern

12 ariel.doprado@geo.unibe.ch

13

14 Kevin Norton

15 School of Geography, Environment and Earth Sciences

16 Victoria University of Wellington

17 kevin.norton@vuw.ac.nz

18

19 Romain Delunel

20 Univ Lyon, Université Lumière Lyon 2, CNRS, UMR 5600 EVS, F-69635

21 romain.delunel@univ-lyon2.fr

22

23 **Abstract**

24 River terraces are among the most intriguing geomorphic features that have been reported from the
25 Peruvian Andes hosting some of the most classical staircase terrace systems. Here, we explore how
26 the large-scale tectonic architecture of the Andes in combination with cyclic variations of climate has
27 impacted the generation and routing of sediment and the formation of these terrace systems. We
28 invoke a hydroclimatic and geomorphic control where the landscape steepness and precipitation rates
29 need to exceed a threshold for the release of sediment stored on the hillslopes, so that aggradation
30 begins downstream in the valley. Once the sediment reservoirs on the hillslopes are void of material,
31 the trunk streams start to recycle the previously deposited material, thereby forming a terrace level.
32 Several of such out-of-phase cyclicities between water and sediment discharge have occurred during
33 the Quaternary, and they were synchronous with the glacial periods at the global scale. Most of these
34 climate shifts in Peru are explained by orbitally controlled changes in the solar insolation of the
35 southern American continent and the Altiplano, which impacted the strength of the Andean jet. On
36 its way towards the south, the jet becomes diverted towards the SE and thus away from the Andes
37 where it intercepts with the mountainous topography of the Bolivian Orocline on the eastern flank of
38 the Andes. These are also the latitudes where we mapped the thickest terrace deposits and the highest

39 frequency of terrace occurrence along the Peruvian coast. Accordingly, the large-scale tectonic
40 architecture of the Andes in combination with orbitally controlled variations in insolation has not only
41 influenced the cyclic change in the strength of the Andean jet, but it has also conditioned the region
42 along the Peruvian margin where the out-of-phase cyclicities between water and sediment discharge
43 was large enough for thick staircase terraces to form.

44

45 **1 Introduction**

46 River terrace staircases (Figure 1) are possibly the most intriguing geomorphic features that have been
47 reported from all over the world. They bear information not only on the sedimentary dynamics during
48 the time the sediments were deposited, but also on the morpho-tectonic development of the landscape
49 surrounding them (Bridgland and Westaway, 2014). They chronicle tectonic processes such as uplift,
50 and record the erosional and sedimentary response to both high- and low-frequency climatic
51 fluctuations, as a compilation of global data on terrace occurrence has shown (Bridgland and
52 Westaway, 2008). The surfaces of such terraces represent former floodplains that are situated above
53 the trunk stream's elevation, and they formed as a period of sediment accumulation was followed by
54 a phase of incision (e.g., Merritts et al., 1994; Pazzaglia and Gardner, 1993; Pazzaglia et al., 1998;
55 Vandermaelen et al., 2022a, b). Accordingly, most of the terrace systems parallel the course of
56 streams that formed them, particularly if they occur along the hillslope flanks at the bottom of valleys.
57 The formation of terraces has conventionally been related to changes in the elevation of a stream
58 where an increase in the base level causes an accumulation of sediments, whereas a lowering of the
59 base level of the same stream results in the dissection of the previously deposited fluvial sediments,
60 thereby forming a terrace level. This has been illustrated by Lewin and Gibbard (2010; Figure 1),
61 which shows that terrace levels can be formed by (i) a set of incisions into an already existing valley
62 fill (cut terraces), (ii) coupled cut-and-fill episodes (cut-and-fill terrace sequences), and by (iii)
63 progressive fluvial incision into the bedrock (strath terraces). These mechanisms at work have been
64 documented for various regions around the world (see review articles by Bridgland and Westaway,
65 2008; 2014) and mainly for Quaternary time scales (Lavé and Avouac, 2000; Antoine et al., 2007;
66 Wegmann and Pazzaglia, 2009; Viveen et al., 2013; Kothyari and Luirei, 2016; Schaller et al., 2016;
67 Tofelde et al., 2017; Claude et al., 2019; Rodríguez-Rodríguez et al., 2020; Tao et al., 2020, do Prado
68 et al., 2022; and many others), but Pliocene terraces particularly from hyperarid climates such as the
69 Western Escarpment of the Andes in northern Chile have also been reported (Schlunegger et al.,
70 2006).

71 Although the mechanisms by which a staircase terrace system can form has been well explored and
72 categorized in the literature, explorations of the mechanisms and particularly of the relative role of
73 water Q versus sediment discharge Q_s resulting in the formation of many staircase terrace systems
74 have been thwarted. This is the case either because a detailed chronological framework of the staircase
75 terrace systems has not been established, or because information on water and sediment discharge at
76 the time the terraces were formed has not been available. An exception are the Quaternary terrace
77 sequences situated in the western Andean margin of Peru (Figure 2a), for which a detailed

78 chronological framework has been reconstructed through numerous studies in the past years (Steffen
79 et al., 2009; 2010; Trauerstein et al., 2014; Viveen et al., 2022), and for which (yet limited)
80 information on paleo-water and sediment discharge has been presented (Bekaddour et al., 2014; Litty
81 et al., 2016).

82 Here, we focus our work on the Peruvian valleys that host some of the most spectacular examples of
83 cut-and-fill terraces globally. The formation of the terrace systems in these valleys has previously
84 been related to a combination of rock uplift and orbital climate changes (Viveen et al., 2022), or
85 climate-driven variations in sediment supply (Steffen et al., 2009; Bekaddour et al., 2014; Norton et
86 al., 2016). In addition to the topographically bound terraces in the valleys, terrace surfaces have also
87 been identified adjacent to the Pacific coast particularly along the Peruvian coastal margin south of
88 14.5°S latitude. These terrace levels have been interpreted as uplifted marine terraces or rasas (Regard
89 et al., 2010; 2021) and hence a tectonic driving force has been invoked to explain their formation.
90 Here, we present an overview of previous works that aimed to (i) date these terrace systems mainly
91 through IRSL (infrared-stimulated luminescence) and post infrared-stimulated luminescence methods
92 (pIR-IRSL), and to (ii) estimate modern surface erosion rates and sediment discharge in the geologic
93 past using concentrations of in-situ produced cosmogenic ^{10}Be , ^{21}Ne and ^{26}Al (Kober et al., 2007;
94 2009; Steffen et al., 2009; 2010; Trauerstein et al., 2014; Litty et al., 2019; Viveen et al., 2022). We
95 complement these datasets with information from other sources and particularly with a sediment
96 transport model to investigate how changes in the ratio between sediment supply Q_s and water
97 discharge Q can potentially explain the formation of the staircase terrace systems in the region (Figure
98 1). Following the model results, we invoke a hydroclimatic and geomorphic control where both the
99 landscape steepness and precipitation rates need to exceed a threshold for sediment to be released
100 from the hillslopes. This sediment pulse overwhelms the hydrological system, forming a new
101 aggradation level downstream in the valley. Once the sediment reservoirs on the hillslopes are void
102 of material, the trunk streams start to recycle the previously deposited material, thereby forming a
103 terrace level. Our geomorphic and geochronological data reveal that several of such cyclicities have
104 occurred during the Quaternary and are recorded by the spectacular staircase terrace systems in Peru,
105 and that they were synchronous with the glacial periods at the global scale.

106

107 **2 Setting**

108 2.1 Geomorphologic architecture of the western Andean margin of Peru

109 Along the western Andean margin, the Peruvian landscape has been categorized into two large-scale
110 geomorphic elements. These include a low-relief plateau or ‘meseta’ at elevations > 3000 m a.s.l.
111 where most of the Peruvian streams originate and finally discharge into the Pacific Ocean. The
112 hillslopes on these plateaus are generally flat ($<10^\circ$) and mantled by a m-thick regolith cover. Abbühl
113 et al. (2011) reported ^{10}Be -based catchment averaged denudation rates <0.02 mm/yr in this landscape
114 that are neither linked to precipitation rates nor to morphometric parameters such as hillslope angles.
115 The ‘meseta’ or plateau is bordered to the west by a distinct break-in-slope, also defined as a
116 knickzone (dotted line on Figure 2, and illustrated in Figure 3a) that marks a sharp transition to a

117 steep landscape to the West. The establishment of this knickzone was initiated in response to a period
118 of uplift during the Late Miocene. Since that time the Andean streams have responded to this uplift
119 pulse by headward retreat, thereby forming this distinct topographic step particularly on the western
120 Andean margin (e.g., Schlunegger et al., 2006; Schildgen et al., 2007; Norton and Schlunegger, 2011).
121 This knickzone also defines the eastern boundary of the Western Escarpment (e.g., Wörner et al.,
122 2002; Norton and Schlunegger, 2011), which constitutes the second major geomorphic element,
123 linking the plateau with the lowlands adjacent to the Pacific Ocean. In the upper part of the Western
124 Escarpment, the headward retreat of the Andean streams has resulted in the shaping of a landscape
125 that is characterized by narrow valleys and steep to oversteepened hillslopes (Trauerstein et al., 2013).
126 In the lower part of the Western Escarpment, the Andean landscape gradually tapers towards the
127 Pacific Ocean, and the valleys widen to several kilometers, giving way to a broad floodplain and a
128 flat coastal plain. South of 15° latitudes, however, the streams have cut hundreds of meters-deep
129 valleys into the Coastal Cordillera, and evidence for a broad coastal plain is absent (Reber et al., 2017).
130 Farther west of the coastal margin and north of 14.5°, the offshore topography dips gently westward
131 at <0.5°. The shelf stretches over >100 km to a ledge at c. 500-800 m depth (offshore break-in-slope,
132 Figure 2a) where the offshore landscape steeply dips towards the trench at a depth of >5000 m
133 (Kukowski et al., 2008). South of 15°S, a broad shelf is absent, and the offshore landscape
134 continuously dips towards the trench. At 15°S, a submarine mountain belt, referred to as the Nazca
135 ridge (Figure 2a), intercepts with trench and the South American continent (Hampel et al., 2004).

136

137 2.2 Drainage network, drainage basin morphometries and surface erosion

138 A total of 40-45 drainage basins, extending from the meseta/plateau down to the Pacific Ocean,
139 occupy the western Andean margin of Peru (Reber et al., 2017). These basins have an area between
140 700 and 17'000 km², a hypsometric integral ranging from ~0.2 to 0.6 and a mean slope ranging
141 between 10° and 20° (Reber et al., 2017). The slopes are steepest at the boundary between the plateau
142 and the Western Escarpment, where hillslope angles can reach values up to 60° and more (Trauerstein
143 et al., 2013). Also, in the Western Escarpment, the local relief of these basins ranges between 1 and
144 2 km and positively correlates with mean annual precipitation rates (Trauerstein et al., 2013). These
145 basins host trunk streams that collect and route water from the meseta/plateau to the Pacific Ocean
146 over a downstream length of >150 km. Water discharge in these streams is perennial and ranges, on
147 an annual basis, from approximately 2 to 90 m³/s (Reber et al., 2017). The discharge depends not only
148 on the drainage basins' size, but also on the mean annual precipitation rates and thus on the latitudes
149 where these catchments are situated (Reber et al., 2017). For instance, south of c. 20 and 21°S
150 latitudes, the climate is so dry (< 100 mm/yr, Jordan et al., 2014) that water discharge in the streams
151 with an origin in the high Andes starts to become ephemeral. However, this latitudinal shift from
152 perennial to ephemeral not only depends on the precipitation amounts but also on the size of the
153 catchments (Nester et al., 2007).

154 Recently, basin averaged denudation rates were measured at the basin scale along the entire western
155 Andean margin of Peru using concentrations of cosmogenic ¹⁰Be in riverine quartz minerals. The

156 rates range from 0.03 and 0.2 mm/yr (Reber et al., 2017, Starke et al., 2021) and positively correlate
157 with environmental parameters such as the steepness of the Western Escarpment, the precipitation
158 rates, water discharge in the trunk stream, and the vegetation cover in the region (Abbühl et al., 2011;
159 Trauerstein et al., 2013; Reber et al., 2017; Starke et al., 2021). The same positive correlations have
160 also been identified when suspension loads of sediment are used to estimate basin-averaged sediment
161 yields (Rosas et al., 2023). Yet, a tectonic conditioning on the occurrence of large landslides
162 (Margirier et al., 2015) and a seismic control on the production and release particularly of coarse-
163 grained material (McPhillips et al., 2014) cannot be completely excluded. Considering the
164 aforementioned results, it is evident to infer that environmental parameters could have controlled
165 temporal variations of surface erosion and landscape form in the Peruvian Andes (Montgomery et al.,
166 2001; Trauerstein et al., 2013) and sediment discharge in the Peruvian streams, and that changes in
167 these parameters could have driven the formation of stair-case terrace systems in some of the Peruvian
168 valleys. It is the scope of this contribution to explore this further.

169

170 2.3 Climate in the western Peruvian Andes

171 The climatic conditions in the western Andean margin are strongly controlled by the position of the
172 Intertropical Convergence Zone (ITCZ) and the strength of the Andean jet (Garreaud et al., 2003;
173 2010; Bookhagen and Strecker, 2008; Viveen et al. 2022) (Figure 2b). During austral summer
174 between December and February (DJF, Figure 2b), a stronger insolation of the southern hemisphere
175 results in a southward shift of the ITCZ, with the consequence that atmospheric moisture is transferred
176 from the tropical Amazon basin to the eastern margin of the Altiplano (Garreaud et al. 2003; 2010).
177 These winds parallel the Andes on their eastern flank where the largest portion of the moisture is
178 released as rain. Between approximately 10°S and 18°S latitudes, the Andean jet is deflected towards
179 the SE by the Bolivian Orocline, thereby shifting the Altiplano and the western Andean margin farther
180 south to hyperarid conditions (Figure 2a). These are also the latitudes where the seasonality in
181 precipitation rates is highest as >40% of the annual rain falls during Austral summer in this region
182 (Figure 2b), whereas dry conditions prevail there during Austral winter (season between June and
183 August, JJA in Figure 2c). Accordingly, while the Andes attract the Andean jet and thus moisture due
184 to the strong insolation of its elevated plateau, the same mountain belt and particularly the Bolivian
185 Orocline diverts the winds away from the orogen.

186 Some of the moisture also reaches the western Andean margin of Peru in the form of rainfall, but with
187 a decreasing rate towards the Pacific Ocean and with distinct N-S decreasing trends in the mean
188 annual rainfall rate (Figure 2a). In particular, in the headwaters of the western Peruvian streams, the
189 mean annual precipitation decreases towards the South, from >1000 mm in the headwaters of the
190 Piura River at 5°S latitude (Abbühl et al., 2010), to ~400 mm in the source area of the Pisco River
191 (Bekaddour et al., 2014), and finally to <200 mm in the headwaters of the Lluta River near Arica (Figure
192 2a) at the border between Peru and Chile (Abbühl et al., 2011; Reber et al., 2017). Likewise, in the
193 knickzone areas and farther downstream along the Western Escarpment, the mean annual
194 precipitation rates decrease towards the Pacific coast from ~1000 mm to 200 mm in the Piura basin,

195 400 mm to <100 mm in the Pisco basin, and finally from <100 mm to zero in the Lluta basin (Abbühl
196 et al., 2011). During Austral winter, however, the Altiplano experiences a subsidence of dry air
197 masses due to a more equatorial position of the ITCZ. This results in a dry season not only on the
198 Altiplano but also along the entire western Andean margin of Peru. Research on palaeosoils (Rech et
199 al., 2019) and sedimentological archives (Schlunegger et al., 2017) in the Atacama Desert together
200 with palaeoaltimetry (Ghosh et al., 2006; Garziona et al., 2008) and geodynamic analyses across the
201 Andes of northern Chile (Evenstar et al., 2023) have shown that these mechanisms have been at work
202 since the Late Miocene. At that time, the Andes were considered to have reached an elevation that
203 was sufficiently high to intercept with the wind pattern (Ehlers and Poulsen, 2009; Evenstar et al.,
204 2023), which in turn was also interpreted to have changed the erosion and sedimentation processes
205 on both margins of the Andes (Norton and Schlunegger, 2011).

206 On orbital time scales, shifts in the solar insolation have been considered to result in larger regional
207 heat contrasts, thereby strengthening the Andean jet. This resulted in the transfer of more moisture
208 towards the Altiplano (Hou et al., 2020), as recorded by lake level highstands on the plateau (e.g.,
209 Ouki, Minchin and Tauca pluvial periods; see Baker et al., 2001a, 2001b; Fritz et al., 2004; Placzek
210 et al., 2006; 2013), and by $\delta^{18}\text{O}$ records measured in speleothems in a cave in northern Peru at 6°S
211 latitudes (Cheng et al., 2013). These were also the time periods of glacial advances in the Andes
212 (Bromley et al., 2016; D'Arcy et al., 2019; Rodbell et al., 2022), and globally (e.g., Raymo and
213 Huybers, 2008).

214 Every 2-10 years, the northern margin of Peru experiences El Niño (ENSO) conditions with high
215 precipitation rates up to 3000 mm per year (DeVries, 1987). Such events are reported as triggering
216 larger runoff and even severe flooding in northern Peru (Mettier et al., 2009; Rosas et al., 2020). This
217 is particularly the case during years of extreme conditions (Dewitte and Takahashi, 2019), when
218 sediment suspension loads of Peruvian streams was documented to increase by 3-60 times compared
219 to normal years (Morera et al., 2017), as was particularly the case in 1982/1983 and 1997/1998
220 (Mettier et al., 2009). Whereas ENSO conditions have affected the entire western Andean margin,
221 the largest deviations from the average sea surface temperatures are mainly found north of c. 10°S
222 latitudes (e.g., NOAA Climate.gov, 27th of December 1997) (see Figure 1b).

223

224 2.4 Terraces in the valleys of western Peru and along the Pacific coast

225 Staircase terraces (e.g., Figures 3b, 3c) have been mapped by various authors in several places of
226 Peru. Such geomorphic features occur either as a staircase of cut-and-fill sequences (e.g., Steffen et
227 al., 2009, Ratnayaka et al., 2018; Viveen et al., 2021; Figures 3b, 3c), strath and cut terraces (Viveen
228 et al., 2022), strath terraces (Schlunegger et al., 2006; Figure 3d), hanging scree deposits in valleys
229 (Veit et al., 2016), and as 'rasas' along the coast (Regard et al., 2010). The most prominent terrace
230 sequences, which occur in the valleys, have been reported from the Majes valley at Acroy (Steffen et
231 al., 2010), the Pisco valley (Steffen et al., 2009), the Cañete valley upstream of Herbay Bajo (Viveen
232 et al., 2021), and the Pativilca valley (Trauerstein et al., 2014) (see Figure 2a for location). The city
233 of Lima itself is built on a large fan delta (Karakouzian et al., 1996) that towers 50 m above the Pacific

234 Ocean and that stretches several tens of kilometres into the Rimac valley farther upstream. In other
235 locations, however, the valley floor is flat with angular contacts to the bordering valley floor, and
236 evidence for the occurrence of thick terrace sequences is absent (Figure 3e).

237 The sediments in the Peruvian valleys and particularly the terraces have been the subject of many
238 studies in the past years with the aim of identifying the controlling mechanisms for sediment delivery
239 and terrace formation. These studies can be broadly categorized into those focusing on climatic and
240 tectonic factors, respectively. For instance, Steffen et al. (2009; 2010), Norton et al., (2016) and
241 Viveen et al. (2021) interpreted the formation of staircase terrace systems as a result of cyclic, most
242 likely orbitally driven changes in paleoclimate. This was considered to have resulted in cyclic shifts
243 of sediment supply and starvation, with the consequence that staircase terraces were formed (Figure
244 4a). The geomorphic and sedimentary responses to such climate changes have been intensively
245 explored in the Pisco valley (Steffen et al., 2009; Bekaddour et al., 2014; Norton et al., 2016; e.g.,
246 Figure 3c). Yet evidence for a precipitation control has also been provided for other Peruvian valleys
247 north of Pisco, for the sedimentation of alluvial fans in the Cordillera Oriental of Peru (Ratnayaka et
248 al., 2021), in the Atacama Desert (Nestor et al., 2007) and on the Altiplano (Farabaugh and Rigsby,
249 2005; Rigsby et al., 2003), as well as for the occurrence of large landslides (Trauth et al., 2003) and
250 terrace systems in Argentina (Tofelde et al., 2017). Interestingly, such climate controls have also been
251 used to explain the settlement of human cultures in the Nazca area (Eitel et al., 2005).

252 A direct tectonic driver was postulated by McPhillips et al., (2014) who provided evidence for a
253 seismic control on the release of sediment on the hillslopes. Others focused on exploring a longer-
254 term tectonic control. This mainly concerns the search for the origin of the ‘rasas’, which are
255 encountered along the Pacific coast south of c. 15°S and which were interpreted as uplifted marine
256 terraces (Regard et al., 2010; 2021). A tectonic control has also been invoked to explain the steps
257 between the terrace levels. For the Cañete valley (Figure 2a), for instance, Viveen et al. (2022)
258 suggested that while sediment accumulation was driven by orbital shifts from dry to wet conditions,
259 the subsequent phases of incision and thus the formation of a terrace level were rather controlled by
260 tectonic uplift. An argument that was put forward is that older terrace levels are located at higher
261 elevations than the younger terraces. This was used as evidence for inferring a systematic downcutting
262 by the Cañete River, driven by rock uplift (Figure 4b). As a further mechanism, it was proposed that
263 the occurrence of subsidence particularly along the coastal Peruvian margin north of 14.5°S latitudes
264 thwarted the formation of staircase terrace systems in the region surrounding the coastal plain (Viveen
265 and Schlunegger, 2018, and Figure 4c).

266

267 2.5 Bedrock geology, and origin of the detrital material in the Peruvian streams

268 The bedrock along the western Andean margin of Peru and northern Chile comprises a suite of
269 Quaternary sediments and low-grade metasediments of Mesozoic age (meta-sandstones,
270 limestones, and graywackes) that were intruded by the Cretaceous to early Tertiary Coastal
271 Batholith (granites and granodiorites). In the headwaters, these rocks are unconformably capped
272 by a several hundred metres-thick suite of Tertiary volcanoclastic deposits (Cobbing et al., 1981;

273 Fernández Dávila, 1993; García and Hérail, 2005). As summarized by Wipf (2006) and
274 documented by Pfiffner and Gonzales (2013), the rock units underlying the Tertiary ignimbrites
275 have experienced several phases of shortening and deformation since the Mesozoic. The
276 ignimbrites themselves, however, experienced only the latest period of deformation (i.e., the
277 Quechua phase), which also drove the surface uplift in the Late Miocene that itself initiated the
278 incision of gorges and the formation of the regional knickzone (see above).
279 Trauerstein et al. (2013) explored the potential controls of the rock type on the morphometric
280 properties of the western Andean margin. They found that on the plateau or ‘meseta’, which is
281 situated upstream of the regional knickzone (Figure 3a), the generally low hillslope angles (c.
282 12°) and channel steepnesses (c. 100 m^{0.9}) do not show any correlation with the lithology of the
283 bedrock. Downstream of the regional knickzone, the hillslope angles and channel steepnesses are
284 more variable and apparently higher (mean values ranging from 6 to 23° and 80 to 320 m^{0.9},
285 respectively). Yet, no particular relationships between the morphometric properties of the
286 landscape and the rock type were detected (Trauerstein et al., 2013). However, for the entire
287 Western Escarpment, Trauerstein and co-authors did report a positive correlation between the
288 landscape’s morphology and precipitation rates, and they documented that the distance between
289 the Pacific Coast and the upper boundary of the knickzones positively correlates to the size of
290 the drainage basin and particularly to the water discharge in the rivers. Also, downstream of the
291 regional knickzone, ¹⁰Be-based catchment averaged denudation rates (at the tributary basin scale <
292 200 km²) are ten times larger (0.2 - 0.3 mm/yr) than on the plateau, and they positively correlate with
293 precipitation rates (Abbühl et al., 2011). Apparently, the cosmogenic data suggests that the steep
294 upper part of the Western Escarpment has been the major sediment source in the region (Kober et al.,
295 2007; 2009; Carretier et al., 2015; Abbühl et al., 2011). This inferred material source was recently
296 confirmed by Litty et al. (2016; 2018) based on U-Pb ages, which were determined for riverine zircon
297 grains in the modern sediments and terrace deposits of the Pisco, Rio Rimac (near Lima), Pativilca
298 and Majes valleys (Figure 2a). In particular, Litty and co-authors found that the modern sediments in
299 these valleys have mainly been derived from the upper part of the steep knickzone area, whereas the
300 region close to the Pacific coast has been apparently too dry for erosion to influence the modern
301 provenance signal in the trunk stream. The terrace deposits, however, contain zircon grains that were
302 derived from the entire drainage basin including the tributary basins situated in the lower part of the
303 Western Escarpment. This provenance interpretation is consistent with the ¹⁰Be-based sediment
304 budgets conducted in the Pisco basin. In particular, Bekaddour et al. (2014) and Norton et al. (2016)
305 noted that the tributary basins, which currently experience an arid climate, were an important
306 sediment source during the time when the terrace material was accumulating.

307

308 **3 Datasets and Methods**

309 3.1 Mapping of terrace deposits occurrence

310 We mapped the occurrence of terrace deposits along the western Peruvian margin. This was
311 accomplished remotely on Google Earth imageries and during several field investigations between
312 2000 and 2015.

313

314 3.2 Ages of terrace deposits

315 Ages of the terrace deposits in the Pisco and Majes valleys and along the Pacific coast (conglomerates
316 at Lima and Pativilca) have been determined in the framework of various studies. We compile these
317 data (Table 1) that were previously presented and discussed in Steffen et al. (2009; 2010), Trauerstein
318 et al. (2014) and Litty et al. (2018; 2019). We combine these chronological datasets with ages that
319 were established for scree deposits in the Lluta valley (Veit et al., 2016) and for a terrace suite in the
320 Cañete valley (Viveen et al., 2022); and we provide a new hydrological framework for interpreting
321 the terraces.

322 One of the first chronological calibrations of these sediments was conducted by Steffen et al. (1996)
323 in the Pisco valley using infrared stimulated luminescence (IRSL) signals measured from a bulk
324 population of potassium-rich feldspar grains. These authors considered feldspar as the preferred
325 mineral for dating because they did not identify significant anomalous fading and instable
326 luminescence signals for feldspar grains, whereas quartz minerals did contain such unstable
327 components that could not be removed during pre-heating. For the Pisco valley (Figure 2a), Steffen
328 et al. (2009) dated nearly all possible sites (a total of 28, Figure S1) where sand lenses were embedded
329 in conglomerates. For the same reason, the ages of the terrace deposits in the Majes valley (a total of
330 18 sites, Figure S2) are based on infrared stimulated luminescence (IRSL) applied to feldspar grains
331 because these minerals yielded stable signals that were void of instable components, which obviously
332 was not the case for quartz minerals. In a subsequent study, Trauerstein et al. (2014) conducted
333 research on the valley fill deposits in the Pativilca valley (Figure 2a). In contrast to Steffen et al.
334 (2009; 2019), these authors applied the IRSL and pIR-IRSL method to small aliquots and individual
335 grains. They found that the samples dated to c. 100 Ka (sites PA01, PA05, PA06, PA09, PA10, and
336 PA11) were not affected by partial bleaching (see also Lowick et al., 2012 and Figure S3 for sample
337 location). We therefore used these results and particularly the central age models (CAM, Galbraith
338 and Roberts, 2012) in our work (Table 1). In contrast, Trauerstein et al. (2014) noted that ages of
339 feldspar grains of samples (PA03, PA12, PA13, PA02, PA07) are likely biased by such an effect, that
340 could, however, be a signal of sediment source (Guyez et al., 2022). The resulting ages are therefore
341 discarded for further analysis in this work. For the same terrace systems, but for a terrace level on its
342 northern margin situated downstream of the outlet of the Pativilca valley (site PAT-DP on Figure S3),
343 Litty et al. (2018) determined a surface exposure age of what they referred to as terrace level T2,
344 using the concentrations of cosmogenic ^{10}Be in the uppermost 5 meters of the sedimentary archive
345 (cosmogenic nuclide depth profile dating, e.g., Braucher et al., 2008; Schaller et al., 2009). These
346 concentrations exponentially decrease with depth, albeit with a large scatter. Such a pattern was used
347 by Litty et al. (2018) to infer an age of 200 ± 90 Ka for the time when this surface was formed. Another
348 terrace surface, closer to the coast, was dated with the same depth-profile approach to 1.2 ± 0.3 Ma.

349 However, ages derived with depth profiling are notoriously biased by surface erosion with the
350 consequence that ^{10}Be concentrations in depth profiles can be at saturation (e.g., Knudsen et al., 2020).
351 Because these effects increase with older ages, we disregard the >1 Ma age in this work. In a
352 subsequent contribution, Litty et al. (2019) dated the conglomerates at Lima (Figure 2a) using the
353 isochron-burial dating method where the ratios between the concentrations of cosmogenic ^{26}Al and
354 ^{10}Be were used to infer a depositional age. Based on that method, Litty et al. (2019) reported ages of
355 c. 490 ± 70 Ka and 490 ± 80 Ka for two different sites, respectively. We included these ages in this work
356 (Table 1).

357 In a recent contribution, Viveen et al. (2022) dated the sedimentary fill of the Cañete valley (c. 12.8°S ;
358 Figure 2a) at 9 sites (Figure S4) along the lowermost c. 45 km segment of the valley. These authors
359 employed the IRSL and pIR-IRSL methodologies on detrital feldspar grains and produced a total of
360 33 deposition ages. They additionally reported improved sample preparation practices ahead of IRSL
361 and pIR-IRSL measurements. In their Figure 10, Viveen et al. (2022) presented overlapping ages
362 calculated from IRSL(50), IRSL(110), IRSL(180) and pIR-IRSL(225) and pIR-IRSL(290) signals,
363 but they noted that the overdispersion is less for the IRSL(110) and IRSL(180) signals than for the
364 IRSL(50) and IRSL(225) ones. We therefore employed the ages resulting from the IRSL(110) and
365 IRSL(180) signals in our compilation (Table 1). An exception is sample Cañete-1, for which Viveen
366 et al. (2022) proposed to employ the pIR-IRSL(225) signal.

367 Finally, we also considered the ^{14}C ages measured on fossiliferous tree trunks and leaves of *Escallonia*
368 *angustifolia* that are preserved in hillslope deposits $\sim 10\text{-}15$ m above the current floor of the Lluta
369 valley (Figure S5, and Veit et al., 2016). Because the growth of these plants requires a constant water
370 supply, the ^{14}C ages yield information about when the groundwater table was high enough reach the
371 roots of these trees.

372 We synthesized the luminescence and ^{14}C ages together with the reported uncertainties in Table 1 and
373 calculated the probability of occurrence for these ages. We did so for each valley and for the entire
374 western Andean margin between c. 20°S and 8°S latitudes (see section 4.2). All sample sites are
375 reported in Figure S1 for the Pisco valley, S2 for the Majes valley, S3 for the Pativilca valley, S4 for
376 the Cañete valley, and S5 for the Lluta valley.

377

378 3.3 Derivation of relationships between water and sediment discharge

379 The formation of the terrace systems along the Peruvian margin could have been caused by shifts in
380 sediment discharge Q_s in relation to changes in water discharge Q (e.g., Viveen et al., 2019). We
381 explore the validity of this hypothesis for the Pisco valley for which a chronological framework of
382 the terrace deposits exists. We proceed through reviewing existing sediment transport models, thereby
383 deriving dependencies of sediment flux on water discharge, and exploring how variations of both
384 parameters can be used to explain the construction of staircase terrace systems. To this end, we start
385 with the bedload transport equation by Bagnold (1966), which builds the basis to estimate the ratio
386 between the mean annual water discharge recorded by the sediments underlying a terrace ($\overline{Q_{paleo}}$)

387 and the modern mean annual water discharge ($\overline{Q_{modern}}$) after some modifications are made.
 388 According to Meyer-Peter and Müller (1948), Bagnold (1966), Paola et al. (1992), Tucker and
 389 Slingerland (1997) and Wong and Parker (2006), the specific bedload discharge q_s can be computed
 390 through:

$$391 \quad q_s = \frac{A}{(\rho_s - \rho_w)\sqrt{\rho_w}} (\tau - \tau_c)^{1.5} \quad (1),$$

392 where A is a constant (which will drop out during the subsequent steps, see equations 5, 6, 7 and 15),
 393 ρ_s and ρ_w are the densities of sediment and water, respectively; τ corresponds to the bed shear stress,
 394 and τ_c denotes a critical shear stress that is required to entrain sediment particles with a threshold
 395 grain size D_x . The total bedload discharge Q_s in a channel with a given width W is then:

$$396 \quad Q_s = q_s W \quad (2).$$

397 The bed shear stress τ is calculated through:

$$398 \quad \tau = \rho_w g d \sin \alpha \quad (3),$$

399 where g is the gravity acceleration, d is water depth and α is the slope of the channel. Because
 400 $\sin \alpha \sim \tan \alpha$ for small slopes $< 1^\circ$ as those in our streams of interest (Schlunegger et al., 2020), we
 401 use the channel gradient $S = \tan \alpha = \frac{\delta h}{\delta x}$, where h is the elevation.

402 Following Shields (1936), the critical shear stress τ_c that is required to mobilize the 50% (median)
 403 grain size percentile (D_{50}) is calculated by:

$$404 \quad \tau_c = \phi (\rho_s - \rho_w) g D_{50} \quad (4),$$

405 Where ϕ denotes the Shields (1936) variable.

406 Note that the D_{84} has preferentially been used if threshold conditions for the incipient motion of
 407 grains are considered, because this grain size percentile apparently best characterizes the sedimentary
 408 framework of a gravel bar and thus the channel form stability (Grant et al., 1990; MacKenzie et al.,
 409 2018). However, the sediment transport rates of Meyer-Peter and Müller (1948), expressed by
 410 equation (1), were originally calibrated with flume experiments that were based on the D_{50} . Because
 411 we are interested in the bulk sediment flux and not particularly in entrainment criteria and the shift of
 412 individual clasts, we employed the D_{50} (Paola and Mohrig, 1996; Pfeiffer and Finnegan, 2018; Chen
 413 et al., 2018) instead of the D_{84} . Note also that equation (1) predicts that during a specific discharge,
 414 the bedload will be mobilized if $\tau/\tau_c = \tau_t > 1$ (e.g., Tucker and Slingerland, 1997, and many others).
 415 In the following, we infer that during channel-forming floods when sediment transport occurs, a river
 416 appears to adjust its channel geometry and particularly its width to new discharge conditions (e.g.,
 417 after a climate change) with the consequence that the τ/τ_c ratios take a constant value for sediment
 418 transport events during which $\tau > \tau_c$ (see also Powell et al., 2016). This inference is based on Parker
 419 (1978), who used field observations and theoretical arguments to propose that during channel-forming
 420 floods when sediment transport occurs, a river dynamically adjusts its channel geometry and
 421 particularly its width to new shear stress conditions. In a subsequent study, Paola and Mohrig (1996)
 422 tested and confirmed this hypothesis based on observations of modern coarse-grained rivers. In their
 423 work, they used channel slope data as benchmark and inferred that τ/τ_c takes a constant value upon

424 analyzing their data. We thus follow Paola and Mohrig (1996) and considered the ratio τ/τ_c as a
 425 constant during bankfull discharge and hence during channel forming floods. This allows us to rewrite
 426 equation (1) accordingly:

$$427 \quad q_s = c_1 D_{50}^{1.5} (\tau_t - 1)^{1.5} \quad (5), \text{ where}$$

$$428 \quad c_1 = [A \phi^{1.5} g^{0.5} (\rho_s - \rho_w)^{0.5}] / \sqrt{\rho_w} \quad (6).$$

429 Combining equations (1), (2) and (5) then yields:

$$430 \quad Q_s = W c_1 D_{50}^{1.5} (\tau_t - 1)^{1.5} \quad (7).$$

431 As a next step, we have to find an expression that relates the bedload discharge Q_s to water discharge
 432 Q . We start with the inference that specific water discharge q can be computed as the product between
 433 the flow velocity v and water depth d :

$$434 \quad q = vd \quad (8).$$

435 We then estimate the mean water velocity v using the Manning-Strickler friction law as a basis and
 436 considering the bed roughness formulation deviated by Ferguson (2007):

$$437 \quad v = (a^{0.6} g^{0.3} S^{0.3} q^{0.4}) / D_{84}^{0.1} \quad (9).$$

438 Note that we employed the D_{84} instead of the D_{50} for the calculation of the flow velocity because it
 439 was shown that the velocity strongly depends on bed's roughness (Ferguson, 2007) and the
 440 sedimentary framework of a gravel bar, which is better characterized by the D_{84} than by the D_{50}
 441 (Grant et al., 1990; MacKenzie et al., 2018).

442 Considering that equation (3) can be rewritten to yield an expression for water depth d :

$$443 \quad d = \frac{(\tau_t \tau_c)}{(\rho_w g S)} = \frac{\tau_t \phi (\rho_s - \rho_w) g D_{50}}{(\rho_w g S)} \quad (10)$$

444 and then combining equations (8), (9) and (10), yields the following expression:

$$445 \quad q = c_2^{1.66} \cdot \frac{D_{50}^{1.66}}{D_{84}^{0.16}} \cdot \frac{\tau_t^{1.66}}{S^{1.66}} \quad (11),$$

446 where

$$447 \quad c_2 = \phi (\rho_s - \rho_w) g^{0.3} a^{0.6} / \rho_w \quad (12).$$

448 The total water discharge Q for a given channel width W is then:

$$449 \quad Q = W c_2^{1.66} \frac{D_{50}^{1.66}}{D_{84}^{0.16}} \frac{\tau_t^{1.66}}{S^{1.66}} \quad (13).$$

450 Considering equation (13) and our inference that rivers adjust channel geometries to new conditions
 451 so that the τ/τ_c ratio is constant then yields an expression, which allows us to determine the ratio
 452 between the discharge values at the time when the terrace sediments accumulated (here denoted
 453 Q_{paleo}) and the modern situation (here denoted as Q_{modern}):

$$454 \quad \frac{Q_{paleo}}{Q_{modern}} = \frac{W_{paleo}}{W_{modern}} \left(\frac{S_{modern}}{S_{paleo}} \right)^{1.166} \frac{D_{50(paleo)}^{1.66} / D_{84(paleo)}^{0.16}}{D_{50(modern)}^{1.66} / D_{84(modern)}^{0.16}} \quad (14).$$

455 Likewise, the use of equation (7) and the same boundary conditions as for equation (14) yields:

$$456 \quad \frac{W_{paleo}}{W_{modern}} = \frac{Q_{s(paleo)}}{Q_{s(modern)}} \left(\frac{D_{50(modern)}}{D_{50(paleo)}} \right)^{1.5} \quad (15).$$

457 The combination of equations (14) and (15) then returns:

$$458 \quad \frac{Q_{paleo}}{Q_{modern}} = \frac{Q_{S(paleo)}}{Q_{S(modern)}} \left(\frac{S_{modern}}{S_{paleo}} \right)^{1.166} \left(\frac{D_{84(modern)}/D_{50(modern)}}{D_{84(paleo)}/D_{50(paleo)}} \right)^{0.166} \quad (16).$$

459 For Pisco valley, Litty et al. (2016) reported data, collected with the Wolman (1954) method, on the
 460 size of the D_{96} and the D_{50} for both the modern and the T1 terrace deposits. The corresponding values
 461 are 1.1 cm for the D_{50} of the modern deposits, and 2.0 cm for the same grain size percentile of the
 462 terrace level T1. The values reported by Litty et al. (2016) for the D_{96} are 7.5 cm for the modern
 463 sediments, and 12.0 for the T1 deposits (see their Tables 1 and 2). The ratio between these percentile
 464 values is 6 for the terrace T1 sediments, and 6.8 for the modern material, which are nearly identical
 465 ratios considering the large uncertainties of at least $\pm 20\%$ on the grain size datasets (Litty et al., 2016).
 466 These values were measured c. 50 km upstream of the Pacific coast at the same location where
 467 Bekaddour et al. (2014) estimated the ^{10}Be -based sediment fluxes, and where the T1 deposits are
 468 entirely made up of fluvial conglomerates (see Litty et al., 2014). Nearly identical D_{96}/D_{50} ratios
 469 (within uncertainties) between the T1 and the modern deposits were also determined a few kilometers
 470 downstream of that site (see Figure 7 in Litty et al., 2016). In a subsequent study where grains sizes
 471 from gravel bars in various streams in Switzerland and Peru (data from Litty et al., 2017a) were
 472 synthesized, Schlunegger et al. (2020) showed that the D_{84}/D_{50} ratios are linearly dependent on the
 473 D_{96}/D_{50} ratios with a correlation coefficient $R^2=0.91$. For the Pisco valley, we may therefore infer
 474 that the grain size ratios D_{84}/D_{50} are equal (within uncertainties) for both the modern and the T1
 475 terrace deposits. If, however, these ratios were much different, then its effect on equation (16) would
 476 be limited because of the low exponent on the grain size ratio (equation 16). Therefore, and also for
 477 simplicity purposes, we can formulate an expression where the discharge ratio only depends on the
 478 ratio between the slope and bedload discharge values between two (modern and paleo) conditions:

$$479 \quad \frac{Q_{paleo}}{Q_{(modern)}} = \frac{Q_{S(paleo)}}{Q_{S(modern)}} \left(\frac{S_{modern}}{S_{paleo}} \right)^{1.166} \quad (17).$$

480 Note that equations (15) and (17) are valid for bankfull discharge conditions when τ_t is constant for
 481 modern and paleo deposits. Therefore, we infer that the relationships expressed by equation (17) are
 482 also valid for the related mean annual values:

$$483 \quad \frac{\overline{Q_{paleo}}}{\overline{Q_{modern}}} = \frac{\overline{Q_{S(paleo)}}}{\overline{Q_{S(modern)}}} \left(\frac{S_{modern}}{S_{paleo}} \right)^{1.166} \quad (18).$$

484 This expression is a modified version of the stream power equation (Bagnold, 1966):

$$485 \quad Q_s \propto Q^m S^n \quad (19),$$

486 where $m=1$ and $n=1.166$. Note also that this equation suggests that the channel curvature θ , which
 487 corresponds to the concavity value $\theta = m/n$ in Hack's (1973) relationship, is c. 0.85. This is a higher
 488 curved channel than what is conventionally inferred ($\theta = 0.45$) upon normalizing the steepness of
 489 channels in mountain belts (e.g., Sklar and Dietrich, 1998; Safran et al., 2005; Korup, 2006), and it is
 490 also higher than reported for streams in the Andes at 3°S (Vanacker et al., 2015). However, channels
 491 with such and even higher concavity values were reported for the Swiss Alps (Norton et al., 2010),
 492 the Yungas on the eastern margin in the Bolivian Andes (Schlunegger et al., 2011) and for some
 493 streams in the western Andean margin of Peru (Trauerstein et al., 2013). The large curvature inferred

494 from equation (18) results from the use of equation (9) that considers a grain-size dependent bed
 495 roughness (Ferguson, 2007) for alluvial channels. In such streams, the selective transport and
 496 deposition of gravels (Ferguson et al., 1996) paired with a natural dynamic adjustment of a stream to
 497 variable water, sediment and energy inputs (Gasparini et al., 1999) have the potential to control rapid
 498 and exponential (Sternberg, 1875) downstream fining of the river gravels. Because of the dependency
 499 of grain size on channel slope (Blissenbach, 1952), such rapid downstream fining would result in a
 500 high channel concavity. However, in cases where most of the supplied sediment is exported and only
 501 a minor fraction of this material is deposited, then the channel concavity is expected to be less. In this
 502 context, in the absence of lateral sediment and water supply to a trunk stream, equation (18) can be
 503 used to determine the relative proportion of the supplied sediment that accumulated on the channel
 504 floor using information on the down-stream decrease of the channel gradient, where:

$$505 \frac{\delta Q_s}{\delta x} / Q_s \propto \frac{Q}{Q_s} \left(\frac{\delta}{\delta x} S^{1.166} \right) = 1.166 \frac{Q}{Q_s} \left(\frac{\delta h}{\delta x} \right)^{0.166} \frac{\delta^2 h}{\delta x^2} \quad (20).$$

506

507 **4 Results**

508 4.1 Occurrence and sedimentology of terrace deposits

509 Along the western Andean margin of Peru (Figure 2a), terraces and terrace deposits occur between c.
 510 6°S and 19°S latitudes (Figure 5a), and such deposits are found either within the valleys at the
 511 confluence between tributary valleys and the trunk valley (type 1), within a trunk valley over a large
 512 downstream distance down to the Pacific coast (type 2) or at the Pacific coast itself (type 3).

513

514 4.1.1 Type 1 terraces: Isolated arroyo fans at the downstream end of tributary valleys

515 Terrace sediments of type 1 are found at the confluence between two major streams, or more
 516 frequently they occur where a tributary arroyo converges with a trunk. Such deposits are encountered
 517 along the entire western margin of the Peruvian Andes (Figure 5a). Inspection of satellite imagery
 518 shows that the thicknesses of such arroyo-fans increase from ~20 m north of 10°S latitudes to >100
 519 m between 12°S and 14°S (e.g., in the Cañete and Pisco valleys, and Figure 5b). From there, the fan
 520 deposits thin to ≤80 m between 14° and 16° (e.g., Majes valley) and finally to <20 m in the Lluta
 521 valley at 18°S and farther south (Nester et al., 2017). The segment between c. 10°S and 16°S latitudes
 522 is also the region where the arroyo fans transition to tabular terrace systems farther downstream
 523 (similar to the examples described in Mather et al., 2017), thereby forming the terrace sequences of
 524 type 2 (see next section and Figure 5).

525 At the valley bottom, the surfaces of such arroyo deposits have a fan-shaped geometry with
 526 downstream surface slopes that range from <5° (Rio Chicama valley) to nearly 10° (Lluta valley).
 527 Smaller fans appear to have a higher surface gradient than larger ones as is commonly the case for
 528 such deposits (Blair and McPherson, 1994). In addition, the diameters of these tributary arroyos reveal
 529 a large spread between <400 m (Lluta valley) and >1 km (Pisco valley). One of the largest fans,
 530 referred to as the Acoyo megafan, is situated near Acoyo in the Majes valley (Figure 2a) and has a cross-
 531 sectional width of >8 km. In the area of the upstream margin of these fans, the fan surfaces gradually

532 transition into the rocky hillslopes where the fan sediments appear to onlap onto the bedrock. At the
533 base, some of these fans are made up of clast-supported conglomerates (e.g., inset of Figure 3c) that
534 were considered to have been deposited by the trunk stream (e.g., Litty et al., 2016) where water
535 runoff is perennial (Reber et al., 2017). Towards the top, breccia interbeds with a matrix-supported
536 fabric, which evidences deposition by debris flows, increase in abundance and thickness (Figure 3b
537 3c). Up-section, this alternation between conglomerate and breccia beds evolves towards an
538 amalgamated stack of several decimeter- to some meter-thick breccia beds. Such sediments finally
539 occur on the surface of all tributary fans. Finally, in the Lluta valley, at c. 18.4°S / 70.0°W, <5 m-
540 thick-successions with gullies, and stratified hillslope debris occur ~10-15 m above the current valley
541 floor. They contain plant fragments of *Escallonia angustifolia*, which is an evergreen shrub with roots
542 that reach down to the groundwater table (Veit et al., 2016).

543

544 4.1.2 Type 2 terraces: Tabular systems of staircase terraces within trunk valleys

545 Terrace sediments of type 2 transition from the fan-shaped arroyo deposits at the downstream end of
546 a tributary valley (type 1 terraces, see above) to several tens of km-long tabular systems with a surface
547 that gently dips in the downstream direction towards the Pacific coast. Nearly all of these terrace
548 systems are underlain by conglomerates that have a clast-supported fabric. Most of the clasts are flat
549 lying, but in some places, they form bedform clusters of imbricated gravels where the clasts dip in
550 the upstream direction, thus pointing towards a palaeoflow that parallels the flow direction of the
551 modern streams. This suggests that the conglomerates underneath these terraces were formed by
552 fluvial processes and were thus deposited by the trunk stream of the corresponding valley. The terrace
553 deposits either dip beneath the modern surface as is the case at the downstream end of the Pisco valley
554 near the Independencia District at 13.692°S / 76.029°W (Figures 6a, b), or they transition into fan
555 deltas at the Pacific coast. Probably the most prominent example of such a fan delta is situated in
556 Lima. The fan beneath the capital of Peru has a convex-up surface and stretches from 12.071°S /
557 77.129°W, which is the northern margin where the fan surface dips beneath the modern coastal
558 sediments, to 12.168°S / 77.033°W that represents the southern margin of the fan where the fan delta
559 conglomerates onlap laterally onto bedrock. The cross-sectional width of the exposed fan surface is
560 thus ~4 km, and the thickest suite is exposed at Barranco (12.143°S / 77.025°W, district of Lima)
561 where the conglomerates are >50 m thick. Further conglomerates along the Pacific coast are found
562 (from North to South) at the downstream end of the Pativilca valley where a >10 m-thick terrace
563 system underlain by fluvial conglomerates in the valley (10.671°S / 77.694°W) transitions into a fan
564 delta that stretches from 10.689°S / 77.8167°W (northern boundary) to 10.721°S / 77.802°W
565 (southern margin) over a cross-sectional width of ~3.5 km. Fluvial conglomerates, yet at higher
566 elevations are also found south of the Pativilca River at 10.758°S / 77.7656°W, and such
567 conglomerates at the Pacific coast can also be found at the downstream end of the Cañete River where
568 a 50 m-thick suite is exposed along a road cut at 12.806°S / 76.543°W. A suite of conglomerates was
569 then mapped tens of kilometers farther upstream in the Cañete valley, where they form a staircase
570 system of multiple terrace levels (Viveen et al., 2022). Finally, the most spectacular suite of type 2

571 staircase terrace systems (at least according to our perception) is found in the Pisco valley at ~13.7°S
572 where three staircase systems can be found along several tens of kilometers on the valley floor. In
573 summary, type 2 terrace deposits are mainly found in trunk valleys between 7.6°S (Chicama valley)
574 and 15.9°S latitudes (Majes valley, Figure 5a). The thicknesses of the valley-fill deposits increase
575 from ~15 m in the Chicama valley to 30-50 m between 12°S and 14°S (e.g., Cañete and Pisco valleys).
576 Farther south, they thin to <30 m (Ocoña and Majes valleys) and are no longer observed south of
577 16°S (Figures 2a and 5).

578

579 4.1.3 Type 3 terraces: ‘Rasas’

580 Terraces of type 3 (Figure 5a) are encountered as coastal deposits between 14.5°S and 15.5°S and
581 were interpreted as response to rock uplift in relation to the subduction of the Nazca ridge (Marcharé
582 and Ortlieb, 1992). South of ~15°S, terrace systems along the Pacific coast either feature kilometre-
583 wide planar features with a dip towards the ocean (Regard et al., 2010). They form lineaments with a
584 regular spacing that strike sub-parallel to the orientation of the modern coastline, or they occur as
585 escarpments that parallel the coastal orientation of the uplifted coastal terraces. These geomorphic
586 features, which occur at various elevations up to 300 m a.s.l., were interpreted as ‘rasas’ or uplifted
587 marine terraces (Madella et al., 2016; Regard et al., 2010; 2021).

588

589 4.2 Ages of terrace deposits

590 The number of ages reported for terrace sediments in the western Andean valleys has remained quite
591 low, but some archives have already been studied at a quite high level of detail either with infrared
592 stimulated luminescence (IRSL) methods, or with terrestrial cosmogenic nuclides (Table 1). One of
593 the best-investigated terrace systems is situated in the Pisco valley at ~13.7°S latitude. This valley
594 comprises three sets of terrace levels (Figure 6c), where sediments underneath the three levels were
595 dated at 7 sites (Steffen et al., 2009). The conglomerates and breccias underlying the highest terrace
596 T1 span the time interval between 54.0±3.5 Ka (site PSC18) and 34.6±3.8 Ka (site PSC31). A second
597 suite of terrace sediments T2 spanning the interval between 27.8±1.6 Ka (site PSC5) and 16.0±1.1
598 Ka (site PSC28) form terrace levels at a lower elevation, and a lowermost terrace sequence T3 was
599 dated to the time span between c. 11.7±0.9 Ka (site PSC7) and 4.9±0.3 Ka (site PSC14) (Figure 6d).
600 Mapping reveals that the oldest terrace sequence T1 dips beneath the modern sediments at ~20 km
601 upstream of the Pacific coast (Figures 6a, b). From there, the oldest and thus highest terrace level can
602 be traced as far upstream as Huaytará suited at 13.593°S / 75.356°W, which is >100 km upstream
603 from the Pacific coast. There, the T1 terrace deposits reach their largest thickness of >120 m, and they
604 onlap on the bedrock that is exposed on the lateral valley flanks. Between ~10 and 45 km upstream
605 from the Pacific coast, the base of terrace T1 deposits is not exposed, implying that the basal
606 sediments of this terrace level are situated beneath the current valley floor. Farther upstream of km
607 45, however, the base of terrace T1 rests on bedrock. We tentatively assign an upstream-directed trend
608 to the age pattern of the T1 terrace deposits based on these ages, where sediment accumulation first
609 started in the downstream area, from where the locus of sedimentation propagated upstream. We infer

610 the occurrence of such a trend because one of the oldest sites, dated to c. 50 Ka, is situated at the
611 downstream end of terrace level T1 just before the top-level dips beneath the modern sediments.
612 However, 45 km upstream where the terrace deposits start to overly bedrock, nearly a same age was
613 determined for the basal units of the same terrace sequence (Figure 6d).

614 In a recent contribution, Viveen et al. (2022) dated the sedimentary fill of Cañete valley (~12°S) with the
615 IRSL and pIR-IRSL method that they applied on samples collected from 9 sites between the
616 Pacific coast and 45 km farther upstream. The authors presented overlapping ages calculated from
617 the IRSL(110) and IRSL(180) signals and suggested that sediment accumulation occurred at 102±6
618 Ka, 52-39 Ka, 32-20 Ka, 15-10 Ka and at 0.82±0.1 Ka.

619 The Majes valley surrounding Acoy at 16.02°S / 72.49°W is another region where the valley fill
620 deposits have been well investigated (Steffen et al., 2010). There, multiple terrace sequences were
621 dated at 16 sites with IRSL, yielding ages that span the time intervals between c. 110-100 Ka (Acoy
622 megafan), 60-50 Ka, and 12-8 Ka (Figure 7). Note that the samples MAJ19 and MAJ20 (Table 1)
623 with IRSL of 61.1±8.7 Ka and 41.2±5.9 Ka, respectively, were taken from talus slope deposits
624 (Steffen et al., 2020). The oldest ages were additionally confirmed by six ¹⁰Be-based exposure ages
625 (Margirier et al., 2015) of the Chuquibamba landslide (named after the city that is built on it at
626 15.839°S / 72.650°W), which originated in a northern tributary valley and the deposits of which
627 interfinger with the Acoy megafan sediments. The displacement of this landslide was dated by the
628 aforementioned authors with concentrations of cosmogenic ¹⁰Be (see Figure S2 for sample sites) to
629 the age range between c. 96 and 107 Ka (with an uncertainty to c. ±10 Ka, see Table 1). These ages
630 correspond to the ¹⁰Be-based surface exposure age of the Acoy megafan (105.3±10.2 Ka; Margirier
631 et al., 2015), and they are identical to the depositional ages of 107.0 ± 5.0 Ka and 101.6 ± 4.9 Ka
632 (sites MAJ6 and MAJ8, respectively, see Table 1) assigned by Steffen et al. (2010) to the sediments
633 underlying the Acoy fan surface (Figure 7).

634 In the Pativilca valley luminescence samples within the valley itself and along the coast (Table 1)
635 yielded depositional ages of c. 100 Ka (Trauerstein et al., 2014), whereas a 200 Ka-old age has been
636 determined for the terrace deposition on the northern valley margin (Table 1) using concentrations of
637 in-situ ¹⁰Be in a depth profile (Litty et al., 2018). The fan delta conglomerates at Lima were dated to
638 c. 500±90 Ka using the ¹⁰Be-²⁶Al burial dating technique (Litty et al. 2019). Finally, in the Lluta
639 valley, fossiliferous tree trunks and leaves of *Escallonia angustifolia*, which are embedded in scree
640 slope deposits above the current floor, were ¹⁴C-dated to 38 Ka and 15 Ka at 17 sites along the lower
641 part of the Lluta valley (Veit et al., 2016; Table 1).

642 In summary, if the ages of all sedimentary archives and their cumulative probability of occurrence
643 are considered (Figure 8), then sediment accumulation occurred between c. 90-110, 40-60 Ka, 18-30
644 Ka, and 4-14 Ka, consistent with the results of a similar synthesis by Viveen et al. (2022). If a global
645 context is considered, then these ages could potentially correspond to MIS 2, the Younger Dryas, MIS
646 3c and MIS 5c. However, we note that such correlations have to be considered with caution because
647 the assignment of ages to the period when sediment accumulation occurred is associated with large
648 uncertainties and could be biased by the selection of particular IRSL signals upon calculating a

649 luminescence age (see Trauerstein et al., 2014, for a detailed discussion). Nevertheless, if such a
650 correlation is valid, then most terrace sediments started to accumulate following a period of cooling.

651

652 4.3 Application of hydrological framework I: Controls on the formation of staircase terraces

653 The application of equations (18) and (19) also allows us further to understand the formation of
654 staircase terrace systems from a conceptual point of view. In particular, it predicts that if both
655 sediment supply rates Q_s and water discharge Q increase by the same factor, then the channel gradient
656 would not change, with the consequence that no terrace can form. However, if the factor of change is
657 greater for sediment discharge than for water flux (which corresponds to an increase in the sediment
658 load concentration), then a fraction of the transported mechanical load would accumulate on the
659 channel floor with the consequence that the channel gradient S will gradually increase until the
660 sediment transport capacity (equation 1) becomes high enough to evacuate the supplied sediment. In
661 contrast, if sediment discharge decreases but the water discharge remains at a high level, or at least it
662 decreases less than the supply of sediment, then the stream would respond by lowering its channel
663 gradient S to yield a new equilibrium between water discharge, sediment flux and energy gradient
664 (equation 19). Accordingly, the combination of equations (18) and (19) predicts that the formation of
665 staircase terrace systems can be understood as the transient response to an increase in the sediment
666 load concentrations (Q_s/Q ratio) of a stream followed by a decrease of this variable. We note that
667 such an underlying control has already been proposed before based on theoretical (e.g. Tucker and
668 Slingerland, 1997; Parker et al., 1998) experimental (Whipple et al., 1998) and field-based work (e.g.,
669 Viveen et al., 2019), and it is reconfirmed in this contribution.

670 Finally, equation (20) can be used to estimate the relative proportion of the supplied material that will
671 be deposited in the trunk channel particularly along stream segments where lateral sediment and water
672 supply is negligible, as is currently the case for the downstream reach of the Pisco and Lluta and other
673 rivers close to the Pacific coast. In particular, following equation (20), a high curvature of the
674 channel's thalweg (current state) implies that a relatively large fraction of the supplied sediment is
675 accumulating on the channel floor. In the same logic, a relatively low curvature of the long-stream
676 profile (e.g., recorded by the top of terrace level T1) suggests that only a small fraction of the supplied
677 sediment was accumulating in the Pisco valley during the formation of the terrace level T1.

678

679 4.4 Application of the hydrological framework II: Estimates of paleo-water discharge

680 We can also use the hydrological framework elaborated above to estimate whether the terrace deposits
681 record a larger or a lower water discharge in comparison the modern situation. For the Pisco valley,
682 sediment discharge recorded by the valley fill (sediments underlying terrace level T1) and the modern
683 riverine material was determined using a ^{10}Be -based sedimentary budget (Bekaddour et al., 2014). It
684 reveals that during the time when the sediments of terrace level T1 accumulated (MIS 3c), sediment
685 discharge ranged between 130'000 and 325'000 m^3/yr with a mean of 227'000 m^3/yr (or 230'000
686 m^3/yr if rounded) and was thus approximately ten times higher than today (28'000 m^3/yr of 30'000

687 m³/yr if rounded; Litty et al., 2016). Note that the sediment flux data, which was originally determined
 688 by Bekaddour et al. (2014) using concentrations of in-situ ¹⁰Be, was subsequently corrected by Litty
 689 et al. (2016) to account for a possible contribution of solute and suspension loads to the total sediment
 690 flux. Such a correction was necessary because denudation rate estimates that base on in-situ ¹⁰Be
 691 include both the chemical and mechanical contributions to the bulk erosion of bedrock (von
 692 Blanckenburg, 2005). We therefore considered the corrected values of Litty et al. (2016) in this work.
 693 Most important, the sediment budget outlined above can be used to estimate how much more water,
 694 compared to the current situation, was required to evacuate the supplied material on an annual basis.
 695 Conventionally, such a water budget is accomplished using grain size data (Duller et al., 2012),
 696 because such data preserves information on the stream power or the bed shear stress during the time
 697 the sedimentary particles were transported and deposited (Shields, 1936). Because stream power and
 698 bed shear stress depend, among other parameters, on water discharge (e.g., Bagnold, 1966; Torizzo
 699 and Pitlick, 2044; Pfeiffer and Finnegan, 2018; Schlunegger et al., 2020), grain size data in
 700 combination with information on the transport rates of bedload provide useful information to estimate
 701 values of paleo-water discharge during the time the sediments were deposited. However, such an
 702 estimate additionally requires information on the channel width (equation 14), which, however, is not
 703 readily available from stratigraphic records or is usually associated with large uncertainties (Litty et
 704 al., 2016; Chen et al., 2018). We therefore refrain from such an approach and proceed using equation
 705 (18) where the ratio between the mean annual paleo-water discharge and the modern water flux can
 706 be computed based on data about the modern slope ($S_{modern}=0.011$) and the energy gradient during
 707 terrace T1 times ($S_{paleo}=0.015$), and the ratio between the corresponding mean annual transport rates
 708 of sediment (the corresponding sediment discharge values were determined with in-situ ¹⁰Be, see
 709 further above). We proceed through propagating uncertainties with a 20% and 10% standard deviation
 710 on the sediment discharge and the slope values, respectively (Schlunegger et al., 2020), in a Monte
 711 Carlo simulation with 10'000 iterations (Figure 9). We find that the mean annual paleo-water
 712 discharge recorded by the MIS 3c terrace deposits T1 was $5.7_{-2.8}^{+12.6}$ times larger than today (with 95%
 713 confidence interval). Currently, the mean annual precipitation rates in the Pisco valley are c. 270
 714 mm/yr (Reber et al., 2017, data based on the TRMM-V6.3B43.2 precipitation database of Huffman
 715 et al., 2007), and the mean annual water discharge is 13.6 m³/s (data from gauging station 203604,
 716 taken by Reber et al. from the SNIRH database of Peru). As consequence and considering that the
 717 runoff-coefficients are likely to be lower in a wetter climate (thicker soil, more vegetation), an up to
 718 6 times larger water runoff would require much larger rainfall rates up to 1000 mm/yr and possible
 719 more.

720 We note, however, that the application of equation (18) implies that two simplifications are valid.
 721 These include the inferences that (i) the distribution of τ/τ_c values are constant during channel
 722 forming conditions as implied from flume experiments and field observations, and (ii) the grain size
 723 ratios D_{84}/D_{50} are equal (within uncertainties) for both the modern and the terrace deposits. The self-
 724 similar distribution of grain size reported from different fluvial settings in the USA and in Andes of

725 Peru and Argentina (D'Arcy et al., 2017; Litty et al., 2017; Harries et al., 2018) and the results of
726 flume experiments and field data (Parker, 1978) suggest that from a conceptual point of view, the
727 simplifications are valid (see also Paola and Mohrig, 1996, for a test of Parker's hypothesis). We
728 additionally anticipate that the resulting inferences are also applicable to the other Peruvian valley
729 fills where sediment transport was accomplished by fluvial processes (but not by debris flows).

730

731 **5 Reviewing possible mechanisms for the formation of staircase terrace systems**

732 As described above, there are several potential factors that have been suggested as drivers of terrace
733 formation on the west coast of Peru (Figure 4). In the following sections, we evaluate each driver and
734 comment on their relative importance for understanding the construction of these western Andean
735 terraces. Among the various arguments that have been put forward, we prefer an interpretation where
736 the formation of staircase terraces requires cyclic changes in the Q_s/Q ratios, but where changes in
737 water discharge were out-of-phase with shifts in sediment supply (Figure 4a).

738

739 5.1 The role of uplift

740 The formation of the fluvial staircase terraces in the valleys of the western Peruvian Andes has been
741 interpreted as the combined response to climate driven variations in the Q_s/Q ratio between sediment
742 supply Q_s and water discharge Q that are superimposed on a long-term tectonic uplift signal (Viveen
743 et al., 2022; Figure 4b). In particular, the occurrence of tectonic uplift was invoked because in the
744 Cañete valley, the top of an older terrace level is situated at a higher elevation than the surface of a
745 younger terrace (Viveen et al., 2022). Whereas the marine terraces or 'rasas' south of 14.5°S latitude
746 (type 3 terraces) do indeed reflect the occurrence of an uplift component (Ortlieb et al., 1996; Regard
747 et al., 2010; 2021; Saillard et al., 2011, see also section 5.5), we see two problems with inferring such
748 controls for the development of type 1 and 2 terrace systems. In the following, we outline our
749 arguments using the example of the Pisco and Majes valleys where we have collected most data, yet
750 we suggest that the same reasoning is likely applicable to the other sites where terraces are preserved
751 (Figure 5). First, mapping shows that that at the downstream end of the Pisco valley, the modern
752 coastal deposits encroach on the surface of terrace level T1 (Figures 6a, 6b). Such a geometric
753 relationship reflects an onlap that has formed in response to a tectonic subsidence (Figure 4a) or to a
754 rise of the eustatic sea level during the Holocene. In either case, such a geometric relationship is
755 incompatible with the occurrence of uplift, or at least the rate of tectonic uplift would have been lower
756 than the rate at which the global sea level has risen after the Last Glacial Maximum. Second, the
757 sediments underlying the highest terrace level (T1) have an older age than the material underlying the
758 neighboring lower terrace levels (T2 and T3; Figures 6c and 6d), as is particularly the case for the
759 segment of the Pisco valley situated between 50 and 100 km upstream of the Pacific coast (Figure 6d
760 and Figure 2a in Steffen et al., 2009). There, the base of terrace T1 is situated at the same elevation
761 as the base of terrace sequences T2 and T3, but the ages are different: Whereas the basal deposits of
762 the terrace sequence are c. 45 Ka old (site 12 in Figures 6c and 6d), the sediments at the base of terrace
763 sequences T2 and T3 have ages of c. 25 Ka (site 15 in Figures 6c and 6d) and 5 Ka (site 14 in Figures

764 6c and 6d). A similar pattern was also reported for the Majes valley where the bases of the various
765 terrace sequences are close (or even below?) to the current local base-level irrespective of the ages at
766 which the terraces were formed (Steffen et al., 2010; Figure 7). Accordingly, prior to a period of
767 sediment accumulation, the base level of each of these phases was situated at nearly the same
768 elevation. In addition, also in the Majes valley, a fan dated to c. 60 Ka at sites 4 and 5 has a lower
769 surface elevation relative to the current base level than two other fans c. 10 km farther upstream that
770 were dated at sites 2 and 17 to c. 23 Ka and 13 Ka, respectively (Figure 7). In this case, the high and
771 low surface elevations could result from a large and small sedimentary pulse, respectively, and do not
772 necessarily record an uplift signal.

773 At a larger scale, however, the Peruvian valleys do show evidence for a tectonic driving force. These
774 are the distinct knickzones separating the ‘meseta’ or plateau from the Western Escarpment (Figures
775 2a, 3a) and the high steepness values of the Peruvian streams downstream of the knickzones
776 (Trauerstein et al., 2013). As outlined above, these geomorphic features were considered as a transient
777 response of the Andean streams to a period of uplift in the Late Miocene, where streams responded
778 to this uplift by headward retreat (e.g., Schlunegger et al., 2006; Schildgen et al., 2007). We thus
779 envisage a scenario where the formation of the terrace sequences mainly records an environmental
780 driven force, which is superimposed on the legacy of surface uplift in the Late Miocene (Jeffery et
781 al., 2013; Thouret et al., 2017; Viveen et al., 2022). Therefore, the situation where the terrace
782 sequences or perched on bedrock and/or border a bedrock channel as illustrated in Figure 4b and
783 documented by Viveen et al. (2022) for the Cañete valley c. 29 and 43.5 km upstream of the Pacific
784 coast could represent such a situation where the stream is still adjusting to the Late Miocene uplift
785 pulse, but where this process has been superimposed by cyclic and out-of-phase changes in water and
786 sediment discharge. Yet we acknowledge that additional research is needed to further clarify the role
787 of uplift.

788

789 5.2 The role of eustatic sea level variations

790 Because north of 14.5°S the offshore topography along the coastal margin of Peru is generally flatter
791 than the thalweg of the Peruvian rivers (Lemenkova, 2020, and physical maps of Peru), a drop in the
792 eustatic sea level has the potential to initiate a wave of sediment accumulation onshore. In this case,
793 deposition would begin in the flat area that was previously submerged by the sea, and the locus of
794 sediment deposition would then shift upstream. Such an interpretation is consistent with the inferred
795 filling of the Pisco valley from downstream to upstream (Figure 10b). It is also coherent with the
796 chronological framework for the terrace sequences, which reveals that the accumulation of the terrace
797 sediments indeed occurred when the eustatic sea level was most likely lower than today (Figure 8).
798 In the Majes valley, however, fans and terraces were mainly constructed either at the tip of landslides
799 (e.g., the Acoy megafan, Margirier et al., 2015) or after the confluence of tributary streams without
800 any obvious connections to the Pacific Ocean (Figure 7 and Steffen et al., 2010). These observations
801 imply that a supply control on the construction of terrace sequences was probably more important
802 than a potential sea level influence.

803

804 5.3 The role of bedrock lithology

805 The lithology and the fabric of the bedrock has the potential to control the course of glaciers and
806 rivers in mountain belts, and it has been documented to exert a measurable impact on the morphology
807 of valleys, the denudation rates in them and the production of sediment (e.g., Cruz Nunes et al., 2015;
808 Stutenbecker et al., 2016; 2018; Bernard et al., 2019; Mather and Stokes, 2018; Piantelli et al., 2023,
809 and many others). Therefore, it is very likely that the nature of the bedrock has also influenced the
810 generation of sediment in the Peruvian valleys and thus controlled the construction of the staircase
811 terrace systems in these valleys. Such an interpretation is even more obvious considering the
812 deformation history of the bedrock along the western Peruvian margin and thus the formation of faults
813 and fractures in the rock, where the Tertiary ignimbrites experienced less brittle deformation than the
814 underlying Cretaceous units (see section 2.5). As a consequence, Abbühl et al. (2011) thought that
815 the Tertiary units have a lower erodibility than the Cretaceous lithologies and have therefore
816 functioned as cap-rocks. According to these authors, the inferred erodibility contrast has allowed to
817 maintain the regional knickzone (Figure 2a) over 10^6 yr timescales, during which the Andean streams
818 have responded to the Late Miocene uplift through headward retreat (Schlunegger et al., 2006;
819 Schildgen et al., 2007). Despite these lithology controls, the patterns of ^{10}Be -based denudation rates,
820 the generation of sediment, the hillslope angles and channel steepnesses disclose a predominantly
821 precipitation but not a rock type control (Abbühl et al., 2011; Trauerstein et al., 2013). Apparently,
822 while erodibility contrasts have allowed the maintenance of the regional knickzone over 10^6 yr
823 timescales upon headward retreat, the rate at which this retreat has occurred and sediment has been
824 generated has not been influenced by rock type, or at least the related signals were too weak to be
825 measured with available techniques. We therefore exclude the possibility that the formation of the
826 staircase terrace systems in the valleys of western Peru was conditioned and thus controlled by rock
827 type.

828

829 5.4 Climate forcing

830 As outlined above, we neither invoke a tectonic driving force nor changes in the eustatic level and
831 lithology as a primary driving force to explain the formation of the staircase terrace systems in the
832 Peruvian valleys. Accordingly, we are left with an interpretation where a change in the ratio between
833 the supply rates of sediment Q_S and water discharge Q most likely explains the cyclic phases of
834 sediment accumulation and erosion. Recently, such a mechanism has been used to explain the cyclic
835 shifts in aggradation and erosion in Crete, Greece (Ott et al., 2022), and such a scenario is also
836 consistent with the results of landscape evolution models (Tucker and Slingerland, 1997). In this
837 context, we invoke three possibilities to explain such observations.

838 As a first option, we consider a mechanism where increased rainfall could result in a supply pulse of
839 material through rapid erosion on the hillslopes (out-of-phase shifts in sediment and water discharge).
840 This would increase the Q_S/Q ratio, with the consequence that a fraction of the supplied sediment is
841 deposited in order to reach an equilibrium between sediment flux, water discharge and channel slope

842 (equation 19). The subsequent erosional recycling of the previously deposited material would then
843 occur as the sediment supply decreases due to emptying of slope-sediment reservoirs while water
844 discharge remained at a relatively high level. As a second possibility, we see a mechanism where
845 sediment production and supply are positively correlated with rainfall rates (in-phase shifts in
846 sediment and water discharge). This is anticipated to result in a situation where changes in water
847 discharge are associated with corresponding shifts in sediment discharge. Equation (18) predicts that
848 in such an environment, no thick terrace sequences would form. Finally, Veit et al. (2017) proposed
849 a scenario, which we consider as a third mechanism, where an increase in water discharge (at a
850 constant sediment supply) would have caused a lowering of the Lluta valley at c. 15 Ka, thereby
851 explaining the fossiliferous tree trunks and leaves of *Escallonia angustifolia* on the valley flanks c.
852 15-20 m above the modern floodplain. We review these scenarios in the following sections.

853

854 5.4.1 Out-of-phase shifts in sediment and water discharge

855 *The role of a pulse of sediment supplied from the hillslopes to the valley floor*

856 A large sediment supply, or a sediment pulse, from the hillslopes to the channel network (Figure 10a)
857 has the potential to shift the Q_s/Q ratio to a higher value (Figure 11a), leading to the accumulation of
858 a fraction of the supplied sediment and shifting the valley floor to a higher elevation. Such a
859 mechanism corresponds to a top-down geomorphic forcing (e.g., Mather et al., 2016) and could result
860 in the temporary accumulation of sediment on the valley floor. We interpret that such a top-down
861 control is recorded by the stratigraphic architecture of type 1 and type 2 of valley fills, and the inferred
862 mechanisms at work are discussed for the T1 sedimentary suite in the Pisco valley (Figure 4c). In
863 these deposits, fluvial conglomerates with distal sediment sources are replaced up-section by locally
864 sourced debris flow deposits (Steffen et al., 2009) indicating that the debris flow fans were prograding
865 towards the valley center (Figure 10a), driven by the supply of large volumes of sediment (Figure
866 11a). Such an environmental control has been proposed before (Steffen et al., 2009; Bekaddour et al.,
867 2014; Litty et al., 2016; Norton et al., 2016) and is reconfirmed in this work. Because the curvature of
868 the paleo-thalweg was relatively small, we postulate using equation (20) that a relatively minor
869 fraction of the supplied sediment was deposited in the Pisco valley, with the consequence that large
870 volumes of sediment (which we cannot quantify, unfortunately) were exported towards the Pacific
871 Ocean. We additionally interpret that an effective evacuation of the supplied material was
872 accomplished through large water fluxes, which were ~6 times higher than today according to our
873 calculations (Figure 9a). Considering that the current mean annual discharge of the Pisco River is
874 ~13.6 m³/s (Reber et al., 2017), this would correspond to a mean annual paleo-water flux of up to 100
875 m³/s. This increase in water runoff, however, was roughly 20-30% smaller than the change in
876 sediment supply (c. 30'000 m³/yr versus 230'000 m³/yr, ~7-8 times larger sediment supply, see
877 above), which ultimately resulted in the accumulation of a fraction of the supplied sediment. We
878 acknowledge, however, that although we present mean annual values for water and sediment
879 discharge estimates, the precipitation and transport work in these arid environments were most likely
880 not uniformly distributed throughout the year and that most of the transport work could have been

881 accomplished by rare but high-magnitude floods. Such a mechanism at work has been proposed based
882 on an analysis of water discharge patterns of streams in different climate environments across the
883 USA (Molnar, 2001), and it has been documented based on suspension loads of sediment in the Piura
884 River (Northern Peru, Figure 2a) where extreme ENSO conditions have strongly impacted the
885 evacuation of sedimentary material (Mettier et al., 2009). We are not able to explore whether the
886 larger transport work (in comparison to the modern state) as inferred for the T1 terrace sediments in
887 the Pisco valley was associated with a stormier climate, but we note that on average more water was
888 required to accomplish the transport work.

889 The phase of erosion leading to the recycling of the previously deposited sediments and thus to the
890 formation of a terrace level can also be explained using equation (18), where a decrease in the Q_s/Q
891 ratio most likely initiated the period of incision (Figure 11a). As outlined by Norton et al. (2016),
892 such a change could have occurred as the sediment reservoirs on the hillslopes were depleted, while
893 water fluxes were still high or possibly decreased, but this reduction was most likely less than that of
894 the sediment supply. Following this logic, the thickness of a terrace level could be used as a proxy to
895 estimate the ratio between a sedimentary pulse and the increase in water runoff (Figure 1b), which
896 apparently was highest between 12°S and 14°S (Figure 5).

897

898 *Top-down geomorphic forcing and bottom-up sedimentary response in the valley*

899 Because stream power of the Peruvian streams decreases towards the Pacific coast (decreasing slope
900 and decreasing water flux due to possible water infiltration into the subsurface), we interpret that
901 sediment accumulation most likely started somewhere downstream with the locus of deposition then
902 propagating upstream, thereby backfilling the valley with sediment from downstream to upstream
903 (Figure 10b). A similar mechanism has been reported from California (Weldon, 1986) and is
904 consistent with the chronological data from the Pisco valley (Figure 6d). Indeed, available IRSL ages
905 imply that at ~25 km upstream distance from the coast, the sediments close to the top of terrace level
906 T1 have nearly the same age as the basal part of the same sequence but more than 100 km farther
907 upstream (Figure 6d). For instance, the sediments of samples PSC35 and PSC38 (Figure 6d), which
908 have a depositional age of 47.7 ± 2.9 Ka and 51.5 ± 2.9 Ka, respectively, were collected close to the
909 downstream end of terrace level T1 but only a few meters beneath its top (e.g., site 35, see Figure 2B
910 in Steffen et al., 2009). In contrast, the material at site 4 (Figure 6d) has nearly the same age (49.4 ± 2.8
911 Ka; Table 1) but was collected >60 km farther upstream and nearly at the bottom of the >100 m thick
912 terrace sequence. This pattern of ages additionally suggests that while sedimentation continued
913 upstream, the erosion and recycling of the previously deposited material already commenced in the
914 downstream area. Apparently, as the river was depositing some of its bedload in the upstream part, it
915 gained free capacity to entrain sedimentary material farther downstream (see also Weldon, 1986).
916 Accordingly, the inferred top-down geomorphic driving force (Figure 10a), characterized by a supply
917 pulse of sediment with sources on the hillslopes, resulted in a complex bottom-up response by the
918 trunk stream (Figure 10b) such as that sedimentation and erosion occurred out-of-phase in the lower
919 and upper parts of the valley.

920

921 5.4.2 In-phase shifts of water and sediment discharge, and the influence of ENSOs

922 We use the second option where the Q_s/Q ratio did not substantially vary through time to explain the
923 absence of staircase terrace sequences in the Peruvian valleys north of c. 10-8°S latitudes (Figure 5).
924 The consequences of a constant Q_s/Q can be seen in the Piura basin at ~5°S latitude (Figure 11b)
925 where in-situ ^{10}Be concentrations in riverine sand show that catchment-averaged denudation rates and
926 thus sediment supply vary in concert with modern precipitation rates (Abbühl et al., 2010). We
927 suggest that past changes in precipitation rates would therefore have caused a corresponding response
928 in sediment generation and water discharge, explaining the lack of stratigraphic records of such
929 changes (i.e., terraces) in this catchment. Even in the case that sediments did accumulate on the
930 channel floor, the sedimentary material would likely be removed because of strong water discharge
931 during ENSO conditions. Based on a geomorphic analysis of the drainage network in the Piura basin,
932 Abbühl et al. (2010) identified evidence for a shift from transport- to supply-limited conditions in the
933 channel network at an elevation of ~1000 m asl where predominant moisture sources change from an
934 easterly (monsoonal) to a westerly (ENSO) control. Because ENSOs appear to have severely affected
935 the Peruvian margin north of ~10°S latitude (Figure 2b), we infer that precipitation patterns related
936 to ENSO conditions have regularly caused a shift of the Q_s/Q ratios to low values, with the possible
937 consequence that any sedimentary material that did accumulate on the channel floor has been removed
938 (Abbühl et al., 2010).

939

940 5.4.3 Changes in water discharge and the role of groundwater supply

941 Veit et al. (2017) proposed a scenario where at 15 Ka an increase in water discharge would have
942 substantially lowered the floor of the Lluta valley. This interpretation is based on the occurrence of
943 fossiliferous tree trunks and leaves of *Escallonia angustifolia*, which were dated with radiocarbon to
944 the time span between 38 Ka and 15 Ka (Table 1, Veit et al., 2017). These plant fragments were
945 mapped on the valley flanks c. 15-20 m above the modern floodplain (See Figure S5 for sample
946 locations), but such shrubs would actually need a continuous groundwater supply to grow.
947 Additionally, the roots of *Escallonia angustifolia* are apparently not long enough to accommodate the
948 elevation difference between their occurrence on the hillslope and the modern valley floor (10-20 m,
949 see above). For these reasons, Veit et al. (2017) suggested that the valley floor in the Lluta valley was
950 c. 9 m higher during the growth of these plants. At c. 15 Ka, which is the age of the youngest
951 *Escallonia angustifolia* fragment (Table 1), an increase in water discharge (and thus an increase in the
952 Q/Q_s ratio) apparently resulted in a lowering of the valley floor, thereby disconnecting the roots of
953 *Escallonia angustifolia* shrubs from the groundwater table. Veit et al. (2017) proposed that such an
954 increase in water runoff occurred in response to a higher moisture availability on the Altiplano during
955 the Central Andean Pluvial Event (CAPE; Figure 8) between c. 16 and 14 Ka (Quade et al., 2008)
956 when the lakes on the Altiplano reached the highest stand (Fritz et al., 2004; Placzek et al., 2006).

957 However, if this interpretation were valid, we would expect the occurrence of cut terraces in the Lluta
958 valley (Figure 1a), for which we have found no evidence in the field.

959 Therefore, as an alternative hypothesis, we propose that the growth of *Escallonia angustifolia* was
960 controlled by the supply of groundwater with sources on the Altiplano during the time when the lake
961 levels reached a highstand (Tauca period; Figure 8). In this context, the boundary between the Azapa
962 Formation (Oligocene fluvial conglomerates and sandstones) and the overlying Oxaya unit (Early
963 Miocene ignimbrites), which was mapped close to the bottom of the Lluta valley and which also
964 served as detachment horizon of landslides during pluvial periods >2.5 Ma ago (Wörner et al.,
965 2002; Strasser and Schlunegger, 2015), could have assisted as groundwater pathway, establishing a
966 hydrological link between the Altiplano and the dry western Andean margin during pluvial periods.
967 There are indeed several independent observations from the Atacama Desert that support a
968 groundwater-supply hypothesis: (i) Nester et al. (2017) documented an increase in supply of
969 groundwater with sources on the Altiplano particularly during the CAPE period; (ii) Galli and
970 Dingman (1962) reported several springs in the Atacama Desert, and (iii) Hoke et al. (2004) proposed
971 that such springs have been repeatedly charged by groundwater with sources in the Western Cordillera
972 or the Altiplano. The latter authors also suggested that landsliding and the formation of steep
973 headscarps in many locations in the Atacama Desert were formed in response to groundwater sapping.
974

975 5.4.4 Summary: Landscape conditioning and hydroclimatic thresholds

976 Considering the cases mentioned above, we infer a hydroclimatic threshold control on the formation
977 of staircase terrace systems where both the landscape steepness and precipitation rates need to exceed
978 a lowermost limit for the release of a sedimentary pulse. We find such conditions between 10°S and
979 17°S latitudes where erosion on the steep valley flanks beneath the knickzone (Western Escarpment)
980 is activated during wet phases, thereby causing the formation of the type 2 of staircase terrace systems.
981 This also includes the segment where type 1 terraces are thickest (between 12° and 16°S) and where
982 individual arroyo fans converge downstream to a fluvial terrace level. Most of type 1 terrace systems,
983 which occur north and south of the Pisco area, also have such an underlying control, but the out-of-
984 phase shifts between water and sediment discharge appear to have been less pronounced. We thus
985 propose a mechanism where the formation of staircase terraces requires cyclic changes in the Q_s/Q
986 ratios, supporting previous interpretations by Norton et al. (2016) and Viveen et al. (2021; 2022). Our
987 compilation of geomorphic, sedimentologic and provenance data additionally reveals that such
988 conditions of alternating Q_s/Q ratios occur when changes in water discharge are out-of-phase with
989 shifts in sediment supply. As the terraces require high sedimentation loads but not necessarily high
990 discharge, they are likely forming either at the beginning of wet phases or at their end. As we suggest
991 that sediment starvation on the hillslopes is an important driver for the phase of incision (after the
992 period of sediment accumulation), the start of a full terrace cycle from sediment accumulation to
993 erosional recycling should then occur at the beginning of a wet phase.

994

995 5.5 Global climate change controls

996 At the global scale, the phases of sediment accumulation started at the same time when many large
997 glaciers advanced to the lowlands (e.g., Younger Dryas, and the MIS2). In the Central Andes, glacial
998 advances also occurred between c. 40 and 22 Ka, and then again between 13.2 and 12.5 Ka and were
999 considered as isochronous with the summer insolation maxima in the sub-tropics of the Southern
1000 Hemisphere (e.g., D’Arcy et al., 2019; Hein et al., 2017). This also coincides with periods of increased
1001 precipitation on the western Andean margin and the eastern Amazon Basin (Hou et al., 2020).
1002 Considering the large uncertainties, the accumulation of the older terrace deposits e.g., at Lima and
1003 Pativilca could also have occurred during significant glaciations (i.e., MIS 12a and MIS 6). It thus
1004 appears that at the global scale, cold periods with glacial advances (e.g., Raymo and Huybers, 2009)
1005 were associated with a wet and erosive climate at least in the area surrounding the western Andean
1006 margin of Peru. This is attributed to the strengthening of the South American Summer Monsoon and
1007 thus of the Andean jet (Figure 2b) during glacial episodes, as recently concluded by Mey et al. (2020)
1008 and Hou et al. (2020). Accordingly, the formation of the staircase terrace systems appears to coincide,
1009 at first order, with climate shifts but not with sea level changes. While sea level changes do occur
1010 largely in concert over glacial/interglacial phases, they do not appear to be the most important driving
1011 forces for the development of the landscape onshore Peru based on the evidence presented in section
1012 5.2.

1013

1014 5.6 Controls of subduction tectonics

1015 At a more regional scale, it is interesting to notice that close to the Pacific coast, coastal terraces or
1016 ‘rasas’ (type 3 of terraces) are encountered mainly south of 14.5°S (Figures 2a and 5), whereas they
1017 are absent farther north. For the area north of 14.5°S, we interpret that the subsidence of the coastal
1018 margin (Viveen and Schlunegger, 2018) explains the absence of ‘rasas’, whereas the occurrence of
1019 such terraces south of it points to the occurrence of uplift as already noted in section 5.1 and described
1020 in detail by Regard et al. (2010, 2022). We speculate that some (but not all) of these conditions are
1021 controlled by the oblique subduction of the Nazca ridge which strikes from the SW to the NE and has
1022 thus a direction orthogonal to the coastal margin of Peru (Figure 2a). The aseismic ridge extends over
1023 ~1100 km with a height between 2000-1500 m. At its highest point, the ridge reaches water depths
1024 between 2000-3000 m. At the location where the Nazca ridge subducts and hence currently interfaces
1025 with the South American plate (between 14°S and 15°S latitudes), the trench is uplifted up to 1500
1026 m, as documented by Li and Clark (1994). Because the Nazca plate is subducting at 080° and the
1027 Nazca Ridge is trending 045°, the site where the ridge interfaces with the South American plate upon
1028 subduction has shifted southward through time (Hampel, 2002). Therefore, it is possible that some of
1029 the subsidence that we see north of 14.5°S could be related to the passage of this ridge. As a further
1030 complication, the collisional zone north of the Nazca ridge is characterized by a flat-slab subduction
1031 where trench retreat exceeds slab rollback, whereas steep slab subduction prevails south of it and the
1032 trench retreat apparently equals slab rollback (Schepers et al., 2017). In addition, it is interesting to
1033 note that (i) a Coastal Cordillera is present south of 15°, while this geomorphic feature is absent north
1034 of 14.5°S; and that (ii) earthquakes with magnitudes >4 have occurred more frequently south of c.

1035 15°S than farther north (see also Reber et al., 2017). It is unclear, at this stage, how these differences
1036 in the subduction processes have influenced or potentially controlled the subsidence or uplift pattern
1037 of the coastal margin of Peru (Viveen and Schlunegger, 2018) and thus the occurrence or absence of
1038 'rasas'. In either case, it is interesting to note that the geomorphological properties of the coastal
1039 margin of Peru change where the subduction geometry reveals some major shifts along strike.

1040

1041 5.7 Controls of the large-scale tectonic architecture of the Andes

1042 At the scale of the entire Andes, the precipitation pattern appears to be conditioned by the large-scale
1043 tectonic architecture of the Andes that has resulted from the collision between the Nazca and the
1044 South American plates during several tens of millions of years. The result was the construction of an
1045 elevated plateau >4000 m high such as the Altiplano and the formation of the Bolivian Orocline (Kley,
1046 1999; Figure 2a). Whereas the elevated plateau and the resulting strong insolation have driven the
1047 advection of moisture by the Andean jet (Figure 2b) (Garreaud et al. 2003; 2010) particularly during
1048 Austral summer, the Bolivian Orocline on the eastern Andean margin (Figure 2a) has diverted these
1049 winds towards the SE and thus away from the Altiplano and the Peruvian margin. The related effects
1050 are best visible between 14°S and 15°S latitudes where the 400 mm/yr isohyet crosses the Andes from
1051 the Western to the Eastern Cordillera (Figure 2a). On the Eastern Andean margin, the region where
1052 the Andean jet intercepts with the Bolivian Orocline is also the area where modern mean annual
1053 precipitation rates are highest (McQuarrie et al., 2008; Figure 5a), thus documenting the orographic
1054 forcing and the imprint of the widening of the Andes on the climate in this region. Because the
1055 isohyets follow the geometry of the eastern Andean margin and since their deflection corresponds to
1056 the region where currently the seasonality of precipitation is highest (Figure 5b), it is not surprising
1057 that the stratigraphic record of Quaternary climate oscillation show the greatest along-strike changes
1058 at these latitudes (Figure 5): South of these latitudes, the Andean jet is deflected hundreds of
1059 kilometers away from the Pacific margin with the consequence that orbital variations in the strengths
1060 of the Andean jet only had a marginal impact on the geomorphic processes on the Western Andean
1061 Escarpment. However, climate was repeatedly wet enough on the Altiplano for the lakes to reach high
1062 levels (Plasecek et al., 2008), which obviously resulted in periods of large groundwater supply to the
1063 Atacama Desert (see section 5.3.3).

1064 At ~16° latitudes and farther north, more moisture could potentially be transferred from the eastern
1065 margin to the Western Escarpment during times of stronger winds, thereby triggering landslides and
1066 debris flows downstream of the Western Escarpment and releasing several pulses of sediment down
1067 to the Peruvian valleys on the Pacific side of the Andes. These latitudes are indeed the region where
1068 the seasonality of precipitation is currently the highest (Figure 2b), and where the most spectacular
1069 staircase terrace sequences and thickest arroyo and terrace deposits have been observed (Figure 5).
1070 North of 12-10°S, however, the impact of a stronger Andean jet is considered to be less as the Andean
1071 jet mainly parallels the Andean Mountain chain. These are also the latitudes where terrace deposits
1072 are largely absent (Figure 5).

1073 Finally, because the Andean orogen, the Andean monsoon and the precipitation pattern have most
1074 likely evolved in response to a My-old positive feedback (Norton and Schlunegger, 2011; Stalder et
1075 al., 2020), we postulate that the construction of cut-and-fill terrace sequences has also occurred during
1076 several millions of years. However, the seasonality of the related processes was most likely amplified
1077 during the Quaternary and particularly after the Middle Pleistocene Transition when the predominant
1078 climate cycles changed from 41 to 100 ky (Clark et al., 2006). Yet only the most recent ones of such
1079 sedimentary archives have been preserved in the Peruvian valleys.

1080

1081 **6 Conclusion**

1082 The staircase terrace systems along the western Andean margin of Peru most likely record multiple
1083 cyclic phases of a wet and erosive climate, which occurred during time intervals when the global
1084 climate was cold and when glaciers advanced to the lowlands, at least in Europe. On the western
1085 margin of the Peruvian Andes, such a shift towards a cooler climate triggered a pulse of erosion on
1086 the valley's hillslopes, resulting in a short period when sediment supply increased more significantly
1087 than water discharge. These were the times when sediment accumulated on the valley floor. The
1088 temporarily stored sediment was then evacuated to the coastal region as the sediment reservoirs on
1089 the hillslopes were depleted. The consequence was the occurrence of a period of erosion, thereby
1090 leaving a terrace level at a higher elevation. Our review of existing chronologic and sedimentologic
1091 data reveals that the signals of cyclic phases of sedimentation and erosion have been superimposed
1092 on a tectonic driving force, as proposed by Viveen et al. (2022) for the Cañete valley and documented
1093 by Tofelde et al. (2017) for the Central Andes in NW Argentina. In the western margin of the Peruvian
1094 Andes, such an uplift pulse most likely occurred in the Late Miocene and initiated a phase of
1095 headward retreat when a knickzone migrated from the coastal region towards the High Andes over
1096 10^6 yr timescales. The coastal region, however, experienced a phase of subsidence, at least north of
1097 14.5°S south (see section 2). Accordingly, the Peruvian valleys have a cross-sectional shape that
1098 depends on the position of the cross-section relative to the kickzone and on the magnitude of the
1099 sedimentary pulse: In the area of the subsiding coastal plain, terrace levels are hardly visible in the
1100 landscape, whereas close to the knickzone where streams are actively incising into the bedrock,
1101 terrace deposits are likely to be perched on the hillslopes (Figure 12).

1102 As a further implication of our compilation, we find that the terraces are thickest between 10°S and
1103 16°S latitudes, while they thin farther north and south of it. Whereas isolated hanging arroyo fans at
1104 the confluence between tributary and trunk streams do occur at these latitudes, they are too small and
1105 isolated to form several km-long terrace systems downstream of the confluence. We consider this
1106 pattern of terrace occurrence to record a hydroclimatic threshold control where both the landscape
1107 steepness and precipitation rates need to exceed a lowermost limit for the release of a sedimentary
1108 pulse. We find such conditions in the region of thickest terrace occurrence where erosion is activated
1109 on the steep valley flanks beneath the knickzone (Western Escarpment) during wet phases, thereby
1110 causing the formation of kilometer-long and several tens of meters-thick staircase terrace systems.
1111 Farther north and south of this region, the out-of-phase shifts between water and sediment discharge

1112 have been most likely less pronounced, and thick staircase terrace systems could not form. This
1113 spatially limited segment where terraces are thickest coincides with the region where on the opposite
1114 eastern margin of the Andes, the Andean jet is deflected by the Bolivian Orocline. These monsoonal
1115 winds are advected towards the South in response to the stronger insolation that is caused by the large
1116 South American continent and particularly by the Altiplano plateau situated at an elevation >4000 m.
1117 However, approaching the Bolivian Orocline these winds are diverted towards the SE and thus away
1118 from the Peruvian margin. It thus appears that this SE deflection of the Andean jet is responsible for
1119 the strong cyclicity of precipitation on the opposite western margin of the Andes where during pluvial
1120 periods, stronger winds allow more moisture to reach the coastal Peruvian segment, thereby triggering
1121 debris flows on the hillslopes and thus driving large sediment pulses to the valleys. During dry
1122 periods, however, the Andean jet is apparently too weak in this region to allow for sufficient rain to
1123 fall on the Western Escarpment, with the consequence that the sedimentary material is not mobilized
1124 on the hillslopes. Therefore, because the occurrence of terrace sequences in the western Peruvian
1125 Andes has been conditioned by the large-scale architecture of the Andes, we suggest that the
1126 construction of staircase terrace sequences has occurred in response to a long-term geomorphic
1127 process.

1128 We close our review on the terrace formation in Peru with recommendations for further research. We
1129 see the need for assessing the sedimentological properties of the terrace deposits and for collecting
1130 information on the provenance of the material at a higher level of details than what is currently
1131 available. Such information can be used to identify the source areas and the mechanisms through
1132 which the sediment supply and transport has occurred (debris flows versus fluvial processes). Most
1133 important, however, the terrace sequences have to be placed in a precise and spatially high-resolution
1134 chronological framework. This could be accomplished through cosmogenic surface dating, and
1135 particularly through applications of luminescence techniques. Similarly important, data on sediment
1136 and possibly water discharge need to be collected. Sediment flux can be determined through
1137 sedimentary budgeting or ¹⁰Be-based estimates of paleo-erosion rates (e.g., Charreau et al., 2011;
1138 Bekaddour et al., 2014; Madella et al., 2018), and water paleo-water discharge can be estimated using
1139 grain size data and information on channel metrics (either channel gradient, channel depths and/or
1140 widths (e.g., Sharma et al., 2023, for the example of the Middle Eocene Escanilla Formation). Last
1141 but not least, low-temperature thermo-chronometric data would allow to infer the longer-term
1142 exhumation history. Such data would be better suited to constrain the role of tectonic uplift than
1143 surface markers such as the top of terrace levels, which could eventually be controlled by the
1144 magnitude of the supply pulse as we suggest in this work.

1145

1146 **Figure caption**

1147 **Figure 1** Fluvial terraces in a valley. a) A period of valley filling followed by a set of incisions
1148 results in the formation of cut terraces. b) Changes in the ratio between sediment (Q_s)
1149 and water discharge (Q) results in the construction cut-and-fill terrace sequences. Here,
1150 the valley is filled with sediment when the Q_s/Q ratio is high, whereas the previously

1151 deposited material is recycled when the ratio is low. In such a view, the thickness of the
1152 valley fill depends on the magnitude of the Q_s/Q ratio. c) Progressive fluvial incision
1153 into the bedrock leads to the formation of strath terraces. Modified after Lewin and
1154 Gibbard (2010).

1155 **Figure 2** a) Overview Figure, showing the Andes of Peru and the offshore topography, and the
1156 major cities where research on the onshore occurrence of staircase terraces has been
1157 conducted. The figure also displays the regional knickzone, which separates a high-
1158 elevated plateau or ‘meseta’ from the steep Western Escarpment. The latter geomorphic
1159 domain connects the headwaters region of the investigated streams with the Pacific
1160 Ocean. The cities of Pisco, Pativilca and Herbay Bajo (in yellow) are the locations where
1161 the Pisco, Pativilca, and Cañete Rivers debouch into the Pacific Ocean. These are the
1162 valleys where terraces have been dated. The cities of Arica and Acoy (indicated in red)
1163 are located in the Lluta and Majes valleys, respectively, where terrace deposits have been
1164 analyzed as well. b) Location of the Intertropical Convergence Zone (ITCZ) during
1165 Austral summer when a stronger insolation on the southern hemisphere and particularly
1166 on the Altiplano shifts the Hadley cells towards the south. This is considered to trigger
1167 the Andean jet and thus the Andean monsoon. The percentages (Flantua et al., 2016)
1168 indicate the relative proportion of rain that falls during this period. The figure also shows
1169 the reach along the Pacific coastal margin where stronger than average temperatures are
1170 registered during an ENSO year (El Niño Southern Oscillation). c) Same as Figure 2b,
1171 but showing the situation during Austral winter (redrawn after Flantua et al., 2016).

1172
1173 **Figure 3** a) Photo from the headwaters of the Piura River (Figure 2a) illustrating the regional
1174 knickzone that separates a ‘meseta’ with a gentle topography in the headwaters from the
1175 steep Western Escarpment farther downstream. b) Staircase terrace systems in the Majes
1176 valley upstream of Acoy (see Figure 2a for location). The figure also shows that the
1177 terrace deposits comprise a sequence with fluvial conglomerates at the base and locally
1178 sourced debris flow deposits on the top. c) Staircase terrace systems in the Lluta valley
1179 at 13.598°S / 75.623°W, photo taken from Schlunegger et al. (2013). Similar to the
1180 Majes valley, the figure shows that the terrace deposits comprise a sequence with fluvial
1181 conglomerates at the base and locally sourced debris flow deposits on the top. d) Strath
1182 terrace of unknown age in the Lluta valley south of Arica (Figure 2a for location). e)
1183 Example of a geomorphic setting (Majes valley downstream of Acoy) where the modern
1184 floodplain does not show any staircase structure and where the valley floor describes a
1185 sharp angle to the bordering hillslope. This is considered as a result of ongoing sediment
1186 accumulation on the valley floor.

1187
1188 **Figure 4** Conceptual figure, illustrating how the cross-sectional shape of a valley changes if
1189 cycling shifts in the Q_s/Q ratio occur along a reach, which experiences a) no uplift, b)

1190 tectonic uplift or ongoing fluvial dissection into bedrock, and c) subsidence. In case a)
1191 the base of each terrace sequence is situated at the same elevation. The height of a terrace
1192 level and thus the thickness of a terrace sequence depends the magnitude of the Q_s/Q
1193 ratio. b) Along reaches where tectonic uplift or ongoing fluvial dissection into bedrock
1194 occurs, the base of a successively younger terrace sequence is situated at a lower
1195 elevation. The situation displayed in b) could also be found in regions where streams
1196 incise into bedrock upon adjusting their longitudinal stream profile in response to an
1197 uplift pulse, which occurred sometime in the past.

1198

1199 **Figure 5** a) Overview figure, showing mean annual precipitation rates (MAP), the spatial
1200 distribution of type 1, 2 and 3 terraces and their thicknesses. b) thickness patterns of type
1201 1 terraces (blue circles) and type 2 terraces (small red circles), as well as lengths (large
1202 red circles) of type 2 terraces.

1203

1204 **Figure 6** Details of the geomorphology of the Pisco River that discharges into the Pacific Ocean
1205 near Pisco (Figure 2a). a) Longitudinal stream profile of the modern river, local slope,
1206 modern sediment discharge, and longitudinal stream profile inferred from the top of
1207 terrace T1 deposits. The figure also shows the paleo-slope (Litty et al., 2016) and the
1208 paleo-sediment discharge recorded by concentrations of in-situ ^{10}Be (Bekaddour et al.,
1209 2014; Litty et al., 2016). b) Geomorphic map of the downstream end of the Pisco valley.
1210 It shows how the terrace level T1 dips beneath the modern surface. c) Sedimentary
1211 architecture of the valley-fill in the Pisco valley c. 80 km upstream from the Pacific
1212 coast. The valley fill can be categorized into three terrace sequences, each of which are
1213 bound by a distinct break-in-slope towards the valley center. Most of the terrace
1214 sequences start with fluvial conglomerates at the base and end with debris flow breccias
1215 towards the top (see also Figure 3c). The numbers correspond to sites where
1216 luminescence samples were collected (e.g., site 11 is sample site PSC11 in Table 1 and
1217 Figure S1). The sample sites are situated c. 3.2 km farther upstream of the location where
1218 the photo of Figure 3c was taken. Modified after Steffen et al. (2009). d) Chronological
1219 framework of the staircase terrace deposits in the Pisco valley. Modified after Steffen et
1220 al. (2009). All ages were determined by Steffen et al. (2009) using infrared stimulated
1221 luminescence (IRSL) methodologies applied to a bulk population of potassium-rich
1222 feldspar grains.

1223

1224 **Figure 7** Chronology and architecture of the terrace sequences and debris flow fans in the Majes
1225 valley. a) Terraces and debris flow fans occur below the confluence of tributary streams
1226 and channels. The thicknesses of fan deposits most likely depend on the magnitude of
1227 the sedimentary pulse. b) Chronological framework of the fan and terrace deposits.

1228 Modified after Steffen et al. (2010). See Figure 2a for location of Majes valley,
1229 Supplementary File S2 for sample sites and Table 1 for ages.

1230

1231 **Figure 8** Pattern of stable isotopes within a chronological framework (Railsback et al., 2015) and
1232 the occurrence of sediment accumulation in the Pisco, Majes Cañete, Pativilca and Lluta
1233 valleys. The figure also displays the ^{10}Be exposure ages of the Chuquibamba landslide
1234 in the Majes valley. Please note that we used the ages of the IRSL(110) and IRSL(180)
1235 signals for the terrace sediments in the Cañete valley as suggested by Viveen et al.
1236 (2022). An exception is the age calculated for the site Cañete-1, which is based on a
1237 IRSL(225) signal. Upon drafting the diagram with the cumulative probability of terrace
1238 ages, we considered the ages from the Lluta valley separately as the wood and root
1239 fragments are rather embedded in hillslope than in terrace deposits (Veit et al., 2016).
1240 See Figure 2a for location of valleys, text for references and Table 1 for the list of ages.
1241 The figure also shows the time span of lake level highstands on the Altiplano (Fritz et
1242 al., 2004; Placzek et al., 2006). CAPE = Central Andean Pluvial Event (Quade et al.,
1243 2008). The pattern of eustatic sea level changes is taken from Waelbroeck et al. (2002).

1244

1245 **Figure 9** Results of Monte Carlo simulation, showing a) the relative occurrence of the inferred
1246 ratios between modern and paleo-water discharge, and how this relates to the ratio
1247 between b) the modern and the paleo-slopes and c) the modern and paleo-sediment
1248 discharge.

1249

1250 **Figure 10** Conceptual figure illustrating the processes and dynamics resulting in the filling of the
1251 Pisco valley. a) A sediment pulse from the hillslopes possibly resulted in a downslope
1252 sediment supply that exceeded the transport capacity of the trunk stream in the valley.
1253 As a result, a fraction of the supplied material was accumulating on the valley floor, and
1254 the lateral tributary fans started to prograde towards the valley center. Such a mechanism
1255 is recorded by a stratigraphic sequence that starts with distally sourced fluvial
1256 conglomerates at the base, and that ends with locally source breccia deposits towards the
1257 top. b) We infer that sediment deposition started downstream where the channel gradient
1258 flattens, and that the location of sediment accumulation shifted further upstream. As a
1259 result of this backfilling, the sediments onlap the valley floor in the upstream direction
1260 (see arrows). Such a mechanism at work is implied by the application of equation 17 and
1261 by the chronological data of terrace T1 deposits (Figure 6d).

1262

1263 **Figure 11** Conceptual figure showing the relationships between the hydroclimate and the landscape
1264 for the modern situation and for the geological past when conditions with an inferred
1265 stronger Andean jet prevailed. The rainfall distributions are different for a) central Peru
1266 (region surrounding Pisco), and b) northern Peru (north of Pativilca). a) Currently in

1267 Central Peru, water and sediment discharge appear to be in equilibrium, and no terrace
1268 appears to be formed. At the beginning of a pluvial period, however, higher rainfall rates
1269 in the area of the Western Escarpment leads to a sediment pulse and a high Q_s/Q ratio
1270 so that that sediment accumulated on the valley floor. Towards the end of the pluvial
1271 period, the hillslopes became void of sediment, with the consequence that the Q_s/Q ratio
1272 was shifted to a low value. The stream responded to this change by dissecting into
1273 previously deposited sediment. b) In northern Peru, both water and sediment discharge
1274 increased most likely by the same factor during pluvial periods. Therefore, the Q_s/Q
1275 ratios did not change, and no terrace sequences were formed.

1276

1277 **Figure 12** Conceptual figure, showing the architecture of the valley fill as a long-term phase of
1278 headward retreat in the headwaters and subsidence at the basin outlet is superimposed
1279 by cyclic changes in the Q_s/Q ratio. Such a situation is likely to be appropriate to
1280 explain the observations in the Peruvian valleys, at least north of 14.5°S latitude. a)
1281 Subsidence along the coastal margin of Peru leads to a drowning and burial of the terrace
1282 systems, with the consequence that the topographic expression of terrace levels becomes
1283 less obvious. b) Farther upstream where neither subsidence nor bedrock downcutting in
1284 the course of headward retreat occurs, the bases of subsequently younger terrace
1285 sequences are situated at nearly the same elevation. c) Towards the headwaters where
1286 the stream is incising into the bedrock in response to ongoing headward retreat, the base
1287 of a younger terrace sequence is located at a lower elevation than that of an older
1288 sequence. d) Close to the knickzone where fluvial dissection is ongoing, the signals of
1289 sedimentary pulses might be recorded as strath terraces.

1290

1291 **Table 1** List of published ages of terrace deposits along the Peruvian margin of the Andes

1292

1293 **Data availability**

1294 All data used for this paper are presented in tables, in the text in the figures.

1295

1296 **Declaration of interests**

1297 The authors have no competing financial interests.

1298

1299 **Acknowledgments**

1300 Financial support was provided by the Swiss National Science Foundation (project numbers 100220,
1301 105162, 105188, 107448, 111638, 119615, 121680, 137516). The constructive and detailed reviews
1302 by V. Vanacker and two anonymous referees are kindly acknowledged. We thank M. Stokes for the
1303 editorial handling of our review paper.

1304

1305 **References**

- 1306 Abbühl, L., Norton, K.P., Schlunegger, F., Kracht, O., Aldahan, A., Possnert, G., 2010. El Niño
1307 forcing on ^{10}Be - based surface denudation rates in the northwestern Peruvian Andes?
1308 *Geomorphology* 123, 257–268. doi:10.1016/j.geomorph.2010.07.017.
- 1309 Abbühl, L., Norton, K.P., Jansen, J.D., Schlunegger, F., Aldahan, A., Possnert, G., 2011. Erosion
1310 rates and mechanisms of knickzone retreat inferred from ^{10}Be measured across strong climate
1311 gradients on the northern and central Andes Western Escarpment. *Earth Surf. Process. Landf.*
1312 36, 1464-1473. <https://doi.org/10.1002/esp.2164>.
- 1313 Antoine, P., Louzet, N.L., Chaussé, C., Lautridou, J.-P., Pastre, J.-F. Auguste, P., Bahain, J.-J.,
1314 Falguères, C., Galehb, B., 2007. Pleistocene fluival terraces from northern France (Seine,
1315 Yonne, Somme): synthesis, and new results from interglacial deposits. *Quat. Sci. Rev.* 22-24,
1316 2701-2723. <https://doi.org/10.1016/j.quascirev.2006.01.036>.
- 1317 Bagnold, R.A., 1966. An Approach to the Sediment Transport Problem from General Physics. *Geol.*
1318 *Surv. Prof. Paper*, 422-I.
- 1319 Baker, P.A., Seltzer, G.O., Fritz, S.C., Dunbar, R.B., Grove, M.J., Cross, S.L., Tapia, P., Rowe,
1320 H.D., Broda, J.P., 2001a. The history of South American tropical precipitation for the
1321 past 25,000 years. *Science* 291, 640-643. <https://doi.org/10.1126/science.291.5504.640>.
- 1322 Baker, P.A., Rigsby, C.A., Seltzer, G.O., Fritz, S.C., Lowenstein, T., Bacher, N., Veliz, C., 2001b.
1323 Tropical climate changes at millennial and orbital timescales on the Bolivian Altiplano.
1324 *Nature* 409, 698-701. <https://doi.org/10.1038/35055524>.
- 1325 Bekaddour, T., Schlunegger, F., Vogel, H., Delunel, R., Norton, K.P., Akçar, N., Kubik, P., 2014.
1326 Paleo erosion rates and climate shifts recorded by Quaternary cut-and-fill sequences in the
1327 Pisco valley, central Peru. *Earth Planet. Sci. Lett.* 390, 103-115.
1328 <https://doi.org/10.1016/j.epsl.2013.12.048>.
- 1329 Bernard, T., Sinclair, H.D., Bailleton, B., Mudd, S.M., Ford, M., 2019. Lithological control on the
1330 post-orogenic topography and erosion history of the Pyrenees. *Earth Planet. Sci. Lett.* 518,
1331 53-66. <https://doi.org/10.1016/j.epsl.2019.04.034>.
- 1332 Blair, T.C., McPherson, J.G., 1994. Alluvial fan processes and forms. In *Geomorphology of desert*
1333 *environments*, Parsons, A.J., Abrahams, A.D. (eds). London, Chapman and Halls, 354-402.
- 1334 Blissenbach, E., 1952. Relation of surface angle distribution to particle size distribution on alluvial
1335 fans. *J. Sed. Petrol.* 22, 25-28.
- 1336 Bookhage, B., Strecker, M., 2008. Orographic barriers, high-resolution TRMM rainfall, and relief
1337 variations along the eastern Andes. *Geophys. Res. Lett.* 35, L06403.
1338 <https://doi.org/10.1029/2007GL032011>.
- 1339 Braucher, R., Del Castillo, P., Simae, L., Hidy, A.J., Bourlés, D.L., 2008. Determination of both
1340 exposure time and denudation rate from an in-situ ^{10}Be depth profile: A mathematical proof of
1341 uniqueness. *Model sensitivity and applications to natural cases. Quat. Geochronol.* 4, 56-67.
1342 <https://doi.org/10.1016/j.quageo.2008.06.001>.

- 1343 Bromley, G.R.M., Schäfer, J.M., Hall, B.L., Rademaker, K.M., Putnam, A.E., Todd, C.E., Helgland,
1344 M., Winckler, G., Jackson, M.S., Strand, P.D., 2016. A cosmogenic ^{10}Be chronology for the
1345 local last glacial maximum and termination in the Cordillera Oriental, southern Peruvian
1346 Andes: Implications for the tropical role in global climate. *Quat. Sci. Rev.* 148, 54-67.
1347 <https://doi.org/10.1016/j.quascirev.2016.07.010>.
- 1348 Bridgland, D.R., Westaway, R., 2008. Climatically controlled river terrace staircases: a worldwide
1349 Quaternary phenomenon. *Geomorphology* 98, 285-315.
- 1350 Bridgland, D.R., Westaway, R., 2014. Quaternary fluvial archives and landscape evolution: a global
1351 synthesis. *Proc. Geol. Assoc.* 125, 600-629.
- 1352 Carretier, S., Regard, V., Vassallo, R., Aguilar, G., Martinod, J., Riquelme, R., Christophoul, F.,
1353 Charrier, R., Gayer, E., Farías, M., Audin, L., Lagane, C., 2015. Differences in ^{10}Be
1354 concentrations between river sand, gravel and pebbles along the western side of the central
1355 Andes. *Quat. Geochronology* 27, 33-51. <http://dx.doi.org/10.1016/j.quageo.2014.12.002>.
- 1356 Charreau, J., Blard, P.-H., Puchol, N., Avouac, J.-P., Lallier-Vergès, F., Bourlès, D., Braucher, R.,
1357 Gallaud, A., Finkel, R., Jolivet, M., Chen, Y., Roy, P., 2011. Paleo-erosion rates in Central
1358 Asia since 9 Ma: A transient increase at the onset of Quaternary glaciations? *Earth
1359 Planet. Sci. Lett.* 304, 85-92. <https://doi.org/10.1016/j.epsl.2022.01.018>.
- 1360 Cheng, H., Sinha, A., Cruz, F.W., Wang, X., Edwards, R.L., d'Horta, F.M., Ribas, C.C., Viulle, M.,
1361 Schott, L.D., Auler, A.S., 2013. Climate change patterns in Amazonia and biodiversity. *Nat.
1362 Comm.* 4, 1-6. <https://doi.org/10.1038/ncomms2415>.
- 1363 Chen, C., Guerit, L., Foreman, B.Z., Hassenruck-Gudipati, H.J., Adatte, T., Honegger, L., Perret, M,
1364 Sluijs, A., Castellort, S., 2018. Estimating regional flood discharge during Palaeocene-Eocene
1365 global warming. *Sci. Rep.* 8, 13391. <https://doi.org/10.1038/s41598-018-31076-3>.
- 1366 Clark, P.U., Archer, D., Pollard, D., Blum, J.D., Rial, J.A., Brovkin, V., Mix, A.C., Pisias, N.G., Roy,
1367 M., 2006. The middle Pleistocene transition: characteristics, mechanisms, and implications for
1368 long-term changes in atmospheric pCO_2 . *Quat. Sci. Rev.* 25, 3150-3184.
1369 <https://doi.org/10.1016/j.quascirev.2006.07.008>.
- 1370 Claude, A., Akçar, N., Ivy-Ochs, S., Schlunegger, F., Kubik, P.W., Christl, M., Vockenhuber, C.,
1371 Kuhlemann, J., Rahn, M., Schlüchter, C., 2019. Changes in landscape evolution patterns in the
1372 northern Swiss Alpine Foreland during the mid-Pleistocene revolution. *GSA Bull.* 131, 2056-
1373 2078. <https://doi.org/10.1130/B31880.1>.
- 1374 Cobbing, E.J., Pitcher, W.S., Wilson, J.J., Baldock, J.W., Taylor, W.P., McCourt, W.J., Snelling
1375 N., 1981. *The Geology of the Western Cordillera of Northern Perú*. Institute of Geological
1376 Sciences Overseas, Memoirs 5, London.
- 1377 Cruz Nunes, F., Delunel, R., Schlunegger, F., Akçar, N., Kubik, P., 2015. Bedrock bedding,
1378 landsliding and erosional budgets in the Central European Alps. *Terra Nova* 27, 370-378.
1379 <https://doi.org/10.1111/ter.12169>.
- 1380 D'Arcy, M., Whittaker, A. C., and Roda-Boluda, D. C., 2017. Measuring alluvial fan sensitivity to

1381 past climate changes using a self-similarity approach to grain-size fining, Death Valley,
1382 California. *Sedimentology* 64, 388–424. doi: 10.1111/sed.12308.

1383 D’Arcy, M.D., Schildgen, T.F., Strecker, M.R., Wittmann, H., Duesing, W., Mey, J., Tofelde, S.,
1384 Weissmann, P., Alonso, R.N., 2019. Timing of past glaciation at the Sierra de Aconquija,
1385 northwestern Argentina, and throughout the Central Andes. *Quat. Sci. Rev.*, 204, 37-57.
1386 <https://doi.org/10.1016/j.quascirev.2018.11.022>.

1387 DeVries, T. J., 1987. A review of geological evidence for ancient El Niño activity in Peru. *J.*
1388 *Geophys. Res.* 92, 14,471-14,479.

1389 Dewitte, B., Takahashi, K., 2019. Extreme El Niño Events. In Venugopal, V., Sukhatme, J.,
1390 Murtugudde, R., Roca, R., *Tropical Extremes*, 165-201.

1391 do Prado, A.H., de Almeida, R.P., Geleazzi, C.P., Sacek, V., Schlunegger, F., 2022. Climate changes
1392 and the formation of fluvial terraces in central Amazonia inferred from landscape evolution
1393 modelling. *Earth Surf. Dyn.* 10, 457-471. <https://doi.org/10.5194/esurf-10-457-2022>.

1394 Ehlers, T.A., Poulsen, C.J., 2009. Influence of Andean uplift on climate and paleoaltimetry
1395 estimates. *Earth Planet. Sci. Lett.*, 281, 238-248.
1396 <https://doi.org/10.1016/j.epsl.2009.02.026>.

1397 Eitel, B., Hecht, S., Mächtle, B., and Schukraft, G., 2005. Geoarchaeological evidence from
1398 desert loess in the nazca-palpa region, southern Peru: Palaeoenvironmental changes and
1399 their impact on pre-columbian cultures. *Archaeometry* 47, 137–158.
1400 <https://doi.org/10.1111/j.1475-4754.2005.00193.x>.

1401 Evenstar, L.A., Hartley, A.J., Mather, A.E., 2023. Orogenic-orographic feedback and the rise of
1402 the Central Andes. *Earth Planet. Sci. Lett.* 602, 117931.
1403 <https://doi.org/10.1016/j.epsl.2022.117931>.

1404 Farabaugh, R.L., Rigsby, C.A., 2005. Climatic influence on sedimentology and geomorphology
1405 of the Rio Ramis Valley, Peru. *J. Sediment. Res.* 75, 12-28.

1406 Farr, T. G. et al., 2007. The Shuttle Radar Topography Mission, *Rev. Geophys.*, 45, RG2004,
1407 doi:10.1029/2005RG000183.

1408 Ferguson, R., Hoegy, T., Walthen, S., Werritty, A., 1996. Field evidence for rapid downstream
1409 finding of river gravels through selective transport. *Geology* 24, 179-182.
1410 [https://doi.org/10.1130/0091-7613\(1996\)024<0179:FEFRDF>2.3.CO;2](https://doi.org/10.1130/0091-7613(1996)024<0179:FEFRDF>2.3.CO;2)

1411 Ferguson, R., 2007. Flow resistance equations for gravel- and boulder- bed streams, *Water Resour.*
1412 *Res.* 43, W05427, <https://doi.org/10.1029/2006WR005422>.

1413 Flantua, S.G.A., Hooghiemstra, H., Vuille, M., Behling, H., Carson, J.F., Cosling, W.D., Hoyos,
1414 I., Ledru, M.P., Montoya, E., Mayle, F., Maldonado, A., Rull, V., Tonello, M.W., Whitney,
1415 B.S., González-Arango, C., 2016. Climate variability and human impact in South America
1416 during the last 2000 years: synthesis and perspectives from pollen records. *Clim. Past.* 12,
1417 483-523. <https://doi.org/10.5194/cp-12-483-2016>.

1418 Fritz, S.C., Baker, P.A., Lowenstein, T.K., Seltzer, G.O., Rigsby, C.A., Dwyer, G.S., Tapia, P.M.,
1419 Arnold, K.K., Ku, T.L., Luo, S., 2004. Hydrologic variation during the last 170,000 years

1420 in the southern hemisphere tropics of South America. *Quat. Res.* 61, 95–104.
1421 <https://doi.org/10.1016/j.yqres.2003.08.007>.

1422 Galli, C., Dingman, R., 1962. Cuadra de los Picos, Alca, Matilla y Chacarilla, con un estudio
1423 sobre los recursos de agua subterránea. Santiago, Chile, Instituto de Investigaciones
1424 Geológicas, 125 pp.

1425 Galbraith, R.F., Roberts, R.G., 2012. Statistical aspects of equivalent dose and error calculation and
1426 display in OSL dating: An overview and some recommendations. *Quat. Geochron.* 11, 1-27.
1427 <https://doi.org/10.1016/j.quageo.2012.04.02>.

1428 García, M., Hérial, G., 2005. Fault - related folding, drainage network evolution and valley
1429 incision during the Neogene in the Andean Precordillera of Northern Chile.
1430 *Geomorphology* 65, 279–300. doi: 10.1016/j.geomorph.2004.09.007.

1431 Garreaud, R.D, Vuille, M., Clement, A.C., 2003. The climate of the Altiplano: observed current
1432 conditions and mechanisms of past changes. *Paleogeogr. Paleoclimatol. Paleoecol.* 194, 5-22.
1433 [https://doi.org/10.1016/S0031-0182\(03\)00269-4](https://doi.org/10.1016/S0031-0182(03)00269-4).

1434 Garreaud, R.D., Molina, A., Farias, M., 2010. Andean uplift, ocean cooling and Atacama
1435 hyperaridity: A climate modeling perspective. *Earth Planet. Sci. Lett.* 292, 39-50.
1436 <https://doi.org/10.1016/j.epsl.2010.01.017>.

1437 Garzione, C.N., Hoke, G.D., Libarkin, J.C., Withers, S., MacFadden, B., Eiler, J., Gosh, P., Mulch,
1438 A., 2008. Rise of the Andes. *Science* 320, 1304-1307.
1439 <https://doi.org/10.1126/science.1148615>.

1440 Gasparini, N.M., Tucker, G.E., Bras, R.L., 1999. Downstream fining through selective particle sorting
1441 in an equilibrium drainage network. *Geology* 27, 1079-1082. [https://doi.org/10.1130/0091-](https://doi.org/10.1130/0091-7613(1999)027<1079:DFTSPS>2.3.CO;2)
1442 [7613\(1999\)027<1079:DFTSPS>2.3.CO;2](https://doi.org/10.1130/0091-7613(1999)027<1079:DFTSPS>2.3.CO;2).

1443 Ghosh, P., Garzione, C.N., Eiler, J.M., 2006. Rapid uplift of the Altiplano revealed through ¹³C-¹⁸O
1444 bonds in paleosol carbonates. *Science* 311, 511-515. <https://doi.org/10.1126/science.1119365>.

1445 Grant, G. E., Swanson, F. J., Wolman, M. G., 1990. Pattern and origin of stepped-bed morphology in
1446 high gradient streams, western Cascades, Oregon. *GSA Bull.* 102, 340–352.
1447 [https://doi.org/10.1130/0016-7606\(1990\)102<0340:PAOOSB>2.3.CO;2](https://doi.org/10.1130/0016-7606(1990)102<0340:PAOOSB>2.3.CO;2)

1448 Guyez, A., Bonnet, S., Reimann, T., Carretier, S., Wallinga, J., 2022. Illuminating past river incision,
1449 sediment source and pathways using luminescence signals of individual feldspar grains
1450 (Rangitikei River, New Zealand). *Earth Surf. Process. Landf.* 47, 1952-1971.
1451 <https://doi.org/10.1002/esp.5357>

1452 Hack, J.T., 1973. Stream profile analysis and stream-gradient index. *US Geol. Surv. J. Res.* 1, 421–
1453 429. [https://doi.org/10.1016/S0012-821X\(02\)00859-2](https://doi.org/10.1016/S0012-821X(02)00859-2).

1454 Hampel, A., 2002. The migration history of the Nazca Ridge along the Peruvian active margin: A re-
1455 evaluation. *Earth Planet. Sci. Lett.* 203, 665-679.

- 1456 Hampel, A., Kukowski, N., Bialas, J., Hübscher, C., Heinbockel, R., 2004. Ridge subduction at an
1457 erosive margin: The collision zone of the Nazca Ridge in southern Peru. *J. Geophys. Res.*,
1458 109, B02101. <https://doi.org/10.1029/2003JB002593>.
- 1459 Harries, R. M., Kirstein, L. A., Whittaker, A. C., Attal, M., Peralta, S., Brooke, S., 2018. Evidence
1460 for Self-Similar Bedload Transport on Andean Alluvial Fans, Iglesia Basin, South Central
1461 Argentina. *J. Geophys. Res. Earth Surf.* 123, 2292–2315. doi: 10.1029/2017JF004501.
- 1462 Hein, A.S., Coge, A., Darvill, C.M., Mendelova, M., Kaplan, M.R., Herman, F., Dunai, T.J., Norton,
1463 K.P., Xu, S., Christl, M., Rodés, A., 2017. Regional mid-Pleistocene glaciation in central
1464 Patagonia, *Quaternary Science Reviews*, Volume 164, 2017, Pages 77-94,
1465 <https://doi.org/10.1016/j.quascirev.2017.03.023>.
- 1466 Hey, R. D., Thorne, C. R., 1986. Stable channels with mobile gravel beds. *J. Hydrol. Eng.* 112, 671–
1467 689. [https://doi.org/10.1061/\(ASCE\)0733-9429\(1986\)112:8\(671\)](https://doi.org/10.1061/(ASCE)0733-9429(1986)112:8(671)).
- 1468 Hoke, G.D, Isacks, B.L., Jordan, T.W., Yu, J.S., 2004. Groundwater-sapping origin for the giant
1469 quebradas of northern Chile. *Geology* 32, 605-608. <https://doi.org/10.1130/G20601.1>.
- 1470 Hou, A., et al., 2020. Insolation and greenhouse gas forcing of the South American Monsoon System
1471 across three glacial- interglacial cycles. *Geophysical Research Letters*, 46, e2020GL087948.
1472 <https://doi.org/10.1029/2020GL087948>.
- 1473 Howard, A. D., 1980. Threshold in river regimes. In *Thresholds in Geomorphology*, Coates, D. R.,
1474 Vitek, J. D. (eds.). Allen and Unwin, Boston, MA, 227–258.
1475 <https://doi.org/10.4324/9781003028697>.
- 1476 Jeffery, M.L., Ehlers, T.A., Yanites, B.J., Poulsen, C.J., 2013. Quantifying the role of
1477 paleoclimate and Andean uplift on river incision. *JGR Earth Surface*, 118, 852-871.
1478 <https://doi.org/10.1002/jgrf.20055>.
- 1479 Jordan, T.E., Kirk-Lawlor, N.E., Blanco, N., Rech, J.A., Cosentino, N.J., 2014. Landscape
1480 modification in response to repeated onset of hyperarid paleoclimate states since 14Ma,
1481 Atacama Desert, Chile. *Geol. Soc. Am. Bull.* 126, 1016–1046.
1482 <http://dx.doi.org/10.1130/B30978.1>.
- 1483 Kley, J., 1999. Geologic and geometric constraints on a kinematic model of the Bolivian orocline. *J.*
1484 *South Amer. Earth Sci.* 12, 221-235.
- 1485 Knudsen, M.F., Nøgaard, J., Grischott, R., Kober, F., Egholm, D.L., Hansen, T.M., Jansen, J.D., 2020.
1486 New cosmogenic nuclide burial-dating model indicates onset of major glaciations in the Alps
1487 during Middle Pleistocene Transition. *Earth Planet. Sci. Lett.* 549, 116491.
1488 <https://doi.org/10.1016/j.epsl.2020.116491>.
- 1489 Kober, F., Ivy-Ochs, S., Schlunegger, F., Baur, H., Kubik, P.W., Wieler, R., 2007. Denudation rates
1490 and a topography-driven rainfall threshold in northern Chile: Multiple cosmogenic nuclide data
1491 and sediment yield budgets. *Geomorphology* 83, 97-120.
1492 <https://doi.org/10.1016/j.geomorph.2006.06.029>.
- 1493 Kober, F., Ivy-Ochs, S., Zeilinger, G., Schlunegger, F., Kubik, P.W., Bauer, H., Wieler, R., 2009.
1494 Complex multiple cosmogenic nuclide concentration and histories in the arid Rio Lluta

1495 catchment, northern Chile. *Earth Surf. Process. Landf.* 34, 398-412.
1496 <https://doi.org/10.1002/esp.1748>.

1497 Kothyari, G.C., Luirei, K., 2016. Late Quaternary tectonic landforms and fluvial aggradation in the
1498 Saryu River valley: Central Kumaun Himalaya. *Geomorphology* 268, 159-176.
1499 <http://dx.doi.org/10.1016/j.geomorph.2016.06.010>.

1500 Korup, O., 2006. Rock-slope failure and the river long profile. *Geology* 34, 45–48.
1501 <https://doi.org/10.1130/G21959.1>.

1502 Kukowski, N., Hampel, A., Hoth, S., Bialas, J., 2008. Morphotectonic and morphometric analysis of
1503 the Nazca plate and the adjacent offshore Peruvian continental slope – implications for
1504 submarine landscape evolution. *Marine Geol.* 254, 107-120.
1505 <https://doi.org/10.1016/j.margeo.2008.05.017>.

1506 Lavé, J., Avouac, J.P., 2000. Active folding of fluvial terraces across the Siwaliks Hills, Himalayas
1507 of central Nepal. *J. Geophys. Res. – Solid Earth* 105, 5735-5779.
1508 <https://doi.org/10.1029/1999JB900292>.

1509 Lemenkova, P., 2020. GRASS GIS topographic and geophysical mapping of the Peru-Chile trench.
1510 *Forum Geographic.* 19, 143-157. <http://dx.doi.org/10.5775/fg.2020.009.d>.

1511 Lewin, J., Gibbard, P.L., 2010. Quaternary river terraces in England: forms, sediments and processes.
1512 *Geomorphology* 120, 293-311.

1513 Li, C., Clark, A.L., 1994. Tectonic effects of the subducting Nazca Ridge on the southern Peru
1514 continental margin. *Marine Petrol. Geol.* 5, 575-586. [https://doi.org/10.1016/0264-](https://doi.org/10.1016/0264-8172(94)90069-8)
1515 [8172\(94\)90069-8](https://doi.org/10.1016/0264-8172(94)90069-8).

1516 Litty, C., Duller, R., Schlunegger, F., 2016. Paleohydraulic reconstruction of a 40 Ka-old terrace
1517 sequence implies that water discharge was larger than today. *Earth Surf. Process. Landf.*, 41,
1518 884-898. <https://doi.org/10.1002/esp.3872>.

1519 Litty, C., Schlunegger, F., Willem, V., 2017a. Possible threshold controls on sediment grain properties
1520 of Peruvian coastal river basins. *Earth Surf. Dyn.* 5, 571-583. [https://doi.org/10.5194/esurf-5-](https://doi.org/10.5194/esurf-5-571-2017)
1521 [571-2017](https://doi.org/10.5194/esurf-5-571-2017).

1522 Litty, C., Lanari, P., Burn, M., Schlunegger, F., 2017b. Climate-controlled shifts in sediment
1523 provenance inferred from detrital zircon ages, western Peruvian Andes. *Geology* 45, 59-62.
1524 <https://doi.org/10.1130/G38371.1>.

1525 Litty, C., Schlunegger, F., Akçar, N., Delunel, R., Christl, M., Vockenhuber, C., 2018. Chronology
1526 of alluvial terrace sediment accumulation and incision in the Pativilca Valley, western Peruvian
1527 Andes. *Geomorphology* 315, 45-56. <https://doi.org/10.1016/j.geomorph.2018.05.005>.

1528 Litty, C., Schlunegger, F., Akçar, N., Lanari, P., Christl, M., Vockenhuber, C., 2019. Possible controls
1529 on the accumulation of Peru’s most prominent alluvial fan: The Lima Conglomerate. *Earth*
1530 *Surf. Process. Landf.* 44, 991-1003. <https://doi.org/10.1002/esp.4548>.

1531 Lowick, S., Trauerstein, M., Preusser, F., 2012. Testing the application of post IR-IRSL dating
1532 to fine grain waterlain sediments. *Quaternary Geochronology* 8, 33-40.
1533 <https://doi.org/10.1016/j.quageo.2011.11.007>.

- 1534 MacKenzie, L., Eaton, B. C., Church, M., 2018. Breaking from the average: Why large grains
1535 matter in gravel-bed streams. *Earth Surf. Proc. Landf.* 43, 3190–3196.
1536 <https://doi.org/10.1002/esp.4465>.
- 1537 Madella, A., Delunel, R., Akçar, N., Schunegger, F., Christl, M., 2018. 10Be-inferred paleo-
1538 denudation rates imply that the mid-Miocene western central Andes eroded as slowly as today.
1539 *Sci. Rep.* 8, 2299. <https://doi.org/10.1038/s41598-018-20681-x>.
- 1540 Madella, A., Delunel, R., Audin, L., Schlunegger, F., 2016. Why is there no Coastal Cordillera at the
1541 Arica Bend (Western Central Andes)? *Basin Res.* 30, 248-268.
1542 <https://onlinelibrary.wiley.com/doi/pdf/10.1111/bre.12218>.
- 1543 Mather, A.E., Stokes, M., Whitfield, E., 2016. River terraces and alluvial fans: The case for an
1544 integrated Quaternary fluvial archive. *Quat. Sci. Rev.* 166, 74-90.
1545 <https://doi.org/10.1016/j.quascirev.2016.09.022>.
- 1546 Mather, A.E., Stokes, M., Whitfield, E., 2017. River terraces and alluvial fans: The case for an
1547 integrated Quaternary fluvial archive. *Quat. Sci. Rev.* 166, 74-90.
1548 <https://doi.org/10.1016.j.quascirev.2016.09.22>.
- 1549 Mather, A.E., Stokes, M., 2018, Bedrock structural control on catchment-scale connectivity and
1550 alluvial fan processes, High Atlas Mountains, Morocco. *Geo. Soc. London Spec. Publ.* 440,
1551 103-128.
- 1552 Margirier, A., Audin, L., Carcaillet, J., Schwartz, S., Benavente, C., 2015. Tectonic and climatic
1553 controls on the Chuquibamba landslide (western Andes, southern Peru). *Earth Surf. Dyn.*
1554 3, 281-289. <https://doi.org/10.5194/esurf-3-281-2015>.
- 1555 McPhillips, D., Bierman, P.R., Rood, D.H., 2014. Millennial-scale record of landslides in the
1556 Andes consistent with earthquake trigger. *Nat. Geosc.* 7, 925-930.
1557 <https://doi.org/10.1038/ngeo2278>
- 1558 MacKenzie, L., Eaton, B. C., Church, M., 2018. Breaking from the average: Why large grains
1559 matter in gravel-bed streams. *Earth Surf. Proc. Landf.* 43, 3190–3196, 2018.
- 1560 McQuarrie, N., Ehlers, T.A., Barnes, J.B., Maede, B., 2008. Temporal variation in climate and
1561 tectonic coupling in the central Andes. *Geology* 36, 999-1002.
1562 <https://doi.org/10.1130/G25124A.1>.
- 1563 Merritts, D.J., Vincent, K.R., Wohl, E.E., 1994. Long river profiles, tectonism, and eustasy: A guide
1564 to interpreting fluvial terraces. *J. Geophys. Res.* 99, 14031-14050.
- 1565 Mettier, R., Schlunegger, F., Schneider, H., Rieke-Zapp, D., Schwab, M., 2009. Relationships
1566 between landscape morphology, climate and surface erosion in northern Peru at 5°S latitude.
1567 *Int. J. Earth Sci.* 98, 2009-2022. <https://doi.org/10.1007/s00531-0355-7>.
- 1568 Mey, J., D’Arcy, M.K., Schildgen, T.F., Egholm, D.L., Wittmann, H., Strecker, M.R., 2020.
1569 Temperature and precipitation in the southern Central Andes during the last glacial maximum,
1570 Heinrich Stadial 1, and the Younger Dryas. *Quat. Sci. Rev.*, 248, 106592.
1571 <https://doi.org/10.1016/j.quascirev.2020.106592>.

1572 Meyer-Peter, E., Müller, R., 1948. Formulas for bedload transport, Proceedings of the 2nd meeting
1573 of the Int. Assoc. Hydraul. Struct. Res., Stockholm, Sweden, Appendix 2, 39–64.

1574 Molnar, P., 2001. Climate change, flooding in arid environments, and erosion rates. *Geology* 29,
1575 1071-1074. [https://doi.org/10.1130/0091-7613\(2001\)029<1071:CCFIAE>2.0.CO;2](https://doi.org/10.1130/0091-7613(2001)029<1071:CCFIAE>2.0.CO;2).

1576 Montgomery, D.R., Balco, G., Willett, S.D., 2001. Climate, tectonics, and the morphology of the
1577 Andes. *Geology* 29, 579-582. [https://doi.org/10.1130/0091-7613\(2001\)029<0579:CTATMO>2.0.CO;2](https://doi.org/10.1130/0091-7613(2001)029<0579:CTATMO>2.0.CO;2).

1579 Morera, S.B., Condom, T., Crave, A., Steer, P., Guyot, J.L., 2017. The impact of extreme El Niño
1580 events on modern sediment transport along the western Peruvian Andes (1968-2012). *Sci Rep.*
1581 7, 11947. <https://doi.org/10.1038/s41598-017-12220-x>.

1582 Nester, P.L., Gayó, E., Latorre, C., Jordan, T.E., Blanco, N., 2007. Perennial stream discharge in the
1583 hyperarid Atacama Desert of northern Chile during the latest Pleistocene. *PNAS* 104, 19724-
1584 19729. <https://doi.org/10.1073/pnas.0705373104>.

1585 Norton, K.P., Abbühl, L.M., Schlunegger, F., 2010. Glacial conditioning as an erosional driving force
1586 in the Central Alps. *Geology* 38, 655-658. <https://doi.org/10.1130/G31102.1>.

1587 Norton, K.P., Schlunegger, F., 2011. Migrating deformation in the Central Andes from enhanced
1588 orographic rainfall. *Nat. Comm.* 2, 584. <https://doi.org/10.1038/ncomms1590>.

1589 Norton, K.P., Schlunegger, F., Litty, C., 2016. On the potential for regolith control of fluvial terrace
1590 formation in semi-arid escarpments. *Earth Surf. Dyn.* 4, 147-157.
1591 <https://doi.org/10.5194/esurf-4-147-2016>.

1592 Ortlieb, L., Goy, J.L., Zazo, C., Hillaire-Marcel, C., Ghaleb, B., Guzman, N., Thiele, R., 1996.
1593 Quaternary morphostratigraphy and vertical deformation in Mejillones Peninsula, Northern
1594 Chile. *Third ISAG, St. Malo (France)* 9, 17-19.

1595 Ott, R.F., Scherler, D., Wegmann, K.W., D'Arcy, M.K., Pope, R.J., Ivy-Ochs, S., Christl, M.,
1596 Vockenhuber, C., Rittenour, T.M., 2022. Paleo-denudation rates suggest variations in runoff
1597 drove aggradation during last glacial cycle, Crete, Greece. *Earth Surf. Proc. Landf.*, 1-20.
1598 <https://doi.org/10.1102/esp.5492>.

1599 Paola, C., Mohrig, D., 1996. Palaeohydraulics revised: palaeoslope estimation in coarse-grained
1600 braided rivers. *Basin Res.* 8, 243–254.

1601 Parker, G. (1978) Self-formed straight rivers with equilibrium banks and mobile bed. Part 2. The
1602 gravel river. *J. Fluid Mech.* 89, 127-146.

1603 Parker, G., Paola, C., Whipple, K.X, Mohrig, D., 1998. Fluvial Fans: Theory. *J Hydr. Eng.* 124, 12-
1604 20.

1605 Paola, C., Heller, P. L., Angevine, C., 1992. The large-scale dynamics of grain size variation in
1606 alluvial basins, 1: Theory. *Basin Res.* 4, 73–90.

1607 Pazzaglia, F.J., Gardner, T.W., 1993. Fluvial terraces of the lower Susquehanna River.
1608 *Geomorphology* 2-3, 83-113. [https://doi.org/10.1016/0169-555X\(93\)90031-V](https://doi.org/10.1016/0169-555X(93)90031-V).

1609 Pazzaglia, F., Gardner, T.W., Merritts, D.J., 1998. Bedrock fluvial incision and longitudinal
1610 profile development over geologic time scales determined by fluvial terraces. *AGU*
1611 *Geophys. Monograph* 107, 207-236.

1612 Pinatelli, F.M., Truttmann, S., Herwegh, M., 2023. The control of collisional tectonics over vally
1613 morphology: the case of the largest glacier in the European Alps. *Terra Nova*, in press.
1614 <https://doi.org/10.1111/ter.1266>.

1615 Pfeiffer, A.M., Finnegan, N.J., 2018. Regional variation in gravel riverbed mobility, controlled by
1616 hydrological regime and sediment supply. *Geophys. Res. Lett.* 45, 3097–3106.
1617 <https://doi.org/10.1002/2017GL076747>.

1618 Pfiffner, O.A., Gonzales, L., 2013. Mesozoic-Cenozoic Evolution of the Western Margin of South
1619 America: Case Study of the Peruvian Andes. *Geosciences* 3, 262-310.
1620 <https://doi.org/10.3390/geosciences3020262>.

1621 Placzek, C., Quade, J., Patchett, P.J., 2006. Geochronology and stratigraphy of late Pleistocene
1622 lake cycles on the southern Bolivian Altiplano: Implication for causes of tropical climate
1623 change. *GSA Bull.* 118, 515–532. <https://doi.org/10.1130/B25770.1>.

1624 Placzek, C.J., Quade, J., Patchett, P.J., 2013. A 130 Ka reconstruction of rainfall on the Bolivian
1625 Altiplano. *Earth Planet. Sci. Lett.* 363, 97-108. <https://doi.org/10.1016/j.epsl.2012.12.017>.

1626 Powell, D.M., Onckelford, A., Rice, S.P., Hillier, J.K., Nguyen, T., Reid, I., Tate, N.J., Ackerley, D.,
1627 2016. Structural properties of mobile armors formed at different flow strengths in gravel-bed
1628 rivers. *JGR Earth Surf.* 121, 1494-1515. <https://doi.org/10.1002/2015JF003794>

1629 Quade, J., Rech, J.A., Betancourt, J.L., Latorre, C., Quade, B., Rylander, K.A., Fisher, T., 2008.
1630 Paleowetlands and regional climate change in the central Atacama Desert, northern Chile. *Quat.*
1631 *Res.* 69, 343-360. <https://doi.org/10.1016/j.yqres.2008.01.003>.

1632 Railsback, L.B., Gibbard, P.L., Head, M.J., Voarintsoa, N.R.G., Toucanne, S., 2015. An optimized
1633 scheme of lettered marine isotope substages for the last 1.0 million years, and the
1634 climatostratigraphic nature of isotope stages and substages. *Quat. Sci. Rev.* 111, 94-106.
1635 <http://dx.doi.org/10.1016/j.quascirev.2015.01.012>.

1636 Ratnayaka, K., Hetzel, R., Hornung, J., Hampel, A., Hinderer, M., Frechen, M., 2021. Postglacial
1637 alluvial fan dynamics in the Cordillera Oriental, Peru, and palaeoclimatic implications. *Quat.*
1638 *Res.* 91, 431-449. <https://doi.org/10.1017/qua.2018.106>.

1639 Raymo, M., Huybers, P., 2008. Unlocking the mysteries of the ice ages. *Nature* 451, 284–285.
1640 <https://doi.org/10.1038/nature06589>

1641 Reber, R., Delunel, R., Schlunegger, F., Litty, C., Madella, A., Akçar, N., Christl, M., 2017.
1642 Environmental controls on ¹⁰Be-based catchment-averaged denudation rates along the western
1643 margin of the Peruvian Andes. *Terra Nova* 29, 292-293. <https://doi.org/10.1111/ter.12274>.

1644 Rech, J.A., Currie, B.S., Jordan, T.E., Riquelme, R., Lehmann, S.B., Kirk-Lawlor, N.E., Li, S.,
1645 Gooley, J.T., 2019. Massive middle Miocene gypsic paleosols in the Atacama Desert and the
1646 formation of the Central Andean rain-shadow. *Earth Planet. Sci. Lett.* 506, 184-194.
1647 <https://doi.org/10.1016/j.epsl.2018.10.040>.

1648 Regard, V., Saillard, M., Martinod, J., Audin, L., Carretier, S., Pedoja, K., Riquelme, R., Paredes, P.
1649 Hérail, G., 2010. Renewed uplift of the Central Andes Forearc revealed by coastal evolution
1650 during the Quaternary. *Earth Planet. Sci. Lett.* 297, 199-201.
1651 <https://doi.org/10.1016/j.epsl.2010.06.020>.

1652 Regard, V., Martinod, J., Saillard, M., Carretier, S., Leanni, L., Hérail, G., Audin, L., Pedoja, K.,
1653 2021. Late Miocene – Quaternary forearc uplift in southern Peru: new insights from ¹⁰Be dates
1654 and rocky coastal sequences. *J. South Amer. Earth Sci.* 109, 103261.
1655 <https://doi.org/10.1016/j.jsames.2021.103261>.

1656 Rigsby, C.A., Baker, P.A., Aldenderfer, M.S., 2003. Fluvial history of the Rio Ilave valley, Peru, and
1657 its relationship to climate and human history. *Paleogeogr. Palaeoclimatol. Paleoecol.* 194, 165-
1658 185. doi:10.1016/S0031-0182(03)00276-1.

1659 Rodbell, D.T., et al., 2022. 700,000 years of tropical Andean glaciation. *Nature* 607, 301-306.
1660 <https://doi.org/10.1038/s41586-022-04873-0>.

1661 Rodríguez-Rodríguez, L., Antón, L., Rodés, A., Pallàs, R., García-Castellanos, D., Jiménez-Munt, I.,
1662 Struth, L., Leanni, L., 2020. Dates and rates of rates of endo-exorheic drainage development:
1663 Insights from fluvial terraces (Duero River, Iberian Peninsula). *Global Planet. Change* 193,
1664 103271. <https://doi.org/10.1016/j.gloplacha.2020.103271>.

1665 Rosas, M.A., Vanacker, V., Viveen, W., Gutierrez, R.R., Huggel, C., 2020. The potential impact of
1666 climate variability on siltation of Andean reservoirs. *J. Hydrol.* 581, 124396.
1667 <https://doi.org/10.1016/j.jhydrol.2019.124396>

1668 Rosas, M.A., Viveen, W., Vanacker, V., 2023. Spatial variation in specific sediment yield along the
1669 Peruvian western Andes. *Catena* 220, 106699. <https://doi.org/10.1016/j.catena.2022.106699>.

1670 Safran, E.B., Biermann, P.R., Aalto, R., Dunne, T., Whipple, K.X., Caffee, M., 2005. Erosion rates
1671 driven by channel network incision in the Bolivian Andes. *Earth Surf. Process. Landf.* 30,
1672 1007-1024. <https://doi.org/10.1002/esp.1259>.

1673 Saillard, M., Hall, S.R., Audin, L., Farber, D.L., Regard, V., Hérail, G., 2011. Andean coastal uplift
1674 and active tectonics in southern Peru: ¹⁰Be surface exposure dating of differentially uplifted
1675 marine terrace sequences (San Juan de Marcona, ~15.4°S). *Geomorphology* 128, 178-190.
1676 <https://doi.org/10.1016/j.geomorph.2011.01.004>.

1677 Schaller, M., Ehlers, T.A., Blum, J.D., Kallenberg, M.A., 2009. Quantifying glacial moraine age,
1678 denudation, and soil mixing with cosmogenic nuclide depth profiles. *J. Geophys. Res.* 114,
1679 F01012. <https://doi.org/10.1029/2007JF000921>.

1680 Schaller, M., Ehlers, T.A., Stor, T., Torrent, J., Lobato, L., Christl, M., Vockenhuber, C., 2016.
1681 Timing of European fluvial terrace formation and incision rates constrained by cosmogenic
1682 nuclide dating. *Earth Planet. Sci. Lett.* 451, 221-231.
1683 <https://doi.org/10.1016/j.epsl.2016.07.022>.

1684 Schepers, G., van Hinsbergen, D.J.J., Spakman, W., Kosters, M.E., Boschman, L.M., McQuarrie, N.,
1685 2017. South-American plate advance and forced Andean trench retreat as drivers for transient
1686 flat subduction episodes. *Nat. Comm.* 8, 15249. <https://doi.org/10.1038/ncomms15249>.

- 1687 Sharma, N., Whittaker, A.C., Watkins, S.E., Valero, L., Vérité, J., Puigdefabregas, C., Adatte, T.,
1688 Garcés, M., Guillocheau, F., Castellort, S., 2023. Water discharge variations control fluvial
1689 stratigraphic architecture in the Middle Eocene Escanilla formation, Spain. *Sci. Rep.* 13, 6834.
1690 <https://doi.org/10.1038/s41598-023-33600-6>.
- 1691 Schildgen, T. F., Hodges, K. V., Whipple, K. W., Reiners, P. W., Pringle, M. S., 2007. Uplift of the
1692 western margin of the Andean plateau revealed from canyon incision history, southern
1693 Peru. *Geology* 35, 523–526.
- 1694 Schlunegger, F., Zeilinger, G., Kounov, A., Kober, F., Hüsser, B., 2006. Scale of relief growth in the
1695 forearc of the Andes of Northern Chile (Arica latitude, 18°S). *Terra Nova* 18, 217-273.
1696 <https://doi.org/10.1111/j.1365-3121.2006.00682.x>.
- 1697 Schlunegger, F., Norton, K., Steffen, D., 2013. Timing the Interface Between Mass Wasting and
1698 Fluvial Processes with OSL. In: Schneuwly-Bollschweiler, M., Stoffel, M., Rudolf-Miklau, F.
1699 (eds.) *Dating Torrential Processes on Fans and Cones. Advances in Global Change Research*,
1700 vol 47. Springer, Dordrecht. https://doi.org/10.1007/978-94-007-4336-6_19
- 1701 Schlunegger, F., Norton, K.P., Delunel, R., Ehlers, T.A., Madella, A., 2017. Late Miocene increase
1702 in precipitation in the Western Cordillera of the Andes between 18-19°S latitudes inferred from
1703 shifts in sedimentation patterns. *Earth Planet. Sci. Lett.* 462, 157-168.
1704 <http://dx.doi.org/10.1016/j.epsl.2017.01.002>.
- 1705 Schlunegger, F., Norton, K.P., Zeilinger, G., 2011. Climate forcing on channel profiles in the Eastern
1706 Cordillera of the Coroico region, Bolivia. *J. Geol.* 119, 97-107. <https://doi.org/10.1086/657407>.
- 1707 Schlunegger, F., Delunel, R., Garefalakis, P., 2020. Short communication: Field data reveal that the
1708 transport probability of clasts in Peruvian and Swiss streams mainly depends on the sorting of
1709 the grains. *Earth Surf. Dyn.* 8, 717-728. <https://doi.org/10.5194/esurf-8-717-2020>.
- 1710 Shields A., 1936. Anwendung der Ähnlichkeitsmechanik und der Turbulenzforschung auf die
1711 Geschiebebewegung, Mitt. Preuss. Versuch. Wasserbau Schiffbau, Berlin, 26 pp.
- 1712 Sklar, L., Dietrich, W.E., 1998. River longitudinal profiles and bedrock incision models: Stream
1713 power and the influence of sediment supply. In *Rivers over Rock, Fluvial Processes in*
1714 *Bedrock Channels*, Tinkler, K.E., Wohl, E.E. (eds). AGU Geophys. Monograph 107, 237–
1715 260.
- 1716 Stalder, N.F., Herman, F., Fellin, M.G., Coutand, I., Aguilar, G., Reiners, P.W., Fox, M., 2020. The
1717 relationships between tectonics, climate and exhumation in the Central Andes (18-36°S):
1718 Evidence from low-temperature thermochronology. *Earth-Sci. Rev.* 210, 103276.
1719 <https://doi.org/10.1016/j.earscirev.2020.103276>.
- 1720 Starke, J., Ehlers, T.A., Schaller, M., 2020. Latitudinal effect of vegetation on erosion rates identified
1721 along western South America. *Science* 367, 1358-1361.
1722 <https://doi.org/10.1126/science.aaz0840>.
- 1723 Steffen, D., Schlunegger, F., Preusser, F., 2009. Drainage basin response to climate change in the
1724 Pisco valley, Peru. *Geology* 37, 491-494. <https://doi.org/10.1130/G25475A.1>.

- 1725 Steffen, D., Schlunegger, F., Preusser, F., 2010. Late Pleistocene fans and terraces in the Majes valley,
 1726 southern Peru, and their relation to climatic variations. *Int. J. Earth Sci.* 99, 1975-1789.
 1727 <https://doi.org/10.1007/s00531-009-0489-2>.
- 1728 Sternberg, H., 1875. Untersuchungen über Längen- und Querprofil geschiefbeführender Flüsse. *Z.*
 1729 *Bauwes.* 25, 486-506.
- 1730 Strasser, M., Schlunegger, F., 2005. Erosional processes, topographic length-scales and geomorphic
 1731 evolution in arid climatic environments: the 'Lluta collapse', northern Chile. *Int. J. Earth Sci.*
 1732 94, 433-446. <https://doi.org/10.1007/s00531-005-0491-2>.
- 1733 Stutenbecker, L. Costa, A., Schlunegger, F., 2016. Lithological control on the landscape form of the
 1734 upper Rhône Basin, Central Swiss Alps. *Earth Surf. Dyn.* 4, 253-272.
 1735 <https://doi.org/10.5194/esurf-4-253-2016>.
- 1736 Stutenbecker, L., Delunel, R., Schlunegger, F., Silva, T.A., Šegvić, B., Girardclos, S., Bakker, M.,
 1737 Costa, A., Lane, S., Loizeau, J.-L., Molnar, P., Akçar, N., Christl, M., 2018. Reduced sediment
 1738 supply in a fast eroding landscape? A multi-proxy sediment budget of the upper Rhône basin,
 1739 Central Alps. *Sed. Geology* 375, 105-119. <https://doi.org/10.1016/j.sedgeo.2017.12.013>.
- 1740 Thouret, J.-C., Gunnell, Y., Jicha, B.R., Paquette, J.-L., Braucher, R., 2017. Canyon incision
 1741 chronology based on ignimbrite stratigraphy and cut-and-fill sediment sequences in SW Peru
 1742 documents intermittent uplift of the western Central Andes. *Geomorphology*, 298, 1-19.
 1743 <https://doi.org/10.1016/j.geomorph.2017.09.013>.
- 1744 Tofelde, S., Schildgen, T.F., Savi, S., Pingel, H., Wickert, A.D., Bookhagen, B., Wittmann, H.,
 1745 Alonso, R.N., Cottle, J., Strecker, M.R., 2017. 100 kyr fluvial cut-and-fill terrace cycles since
 1746 the Middle Pleistocene in the southern Central Andes, NW Argentina. *Earth Planet. Sci. Lett.*
 1747 473, 141-153. <https://doi.org/10.1016/j.epsl.2017.06.001>
- 1748 Torizzo, M., Pitlick, J., 2004. Magnitude-frequency of bed load transport in mountain streams in
 1749 Colorado. *J. Hydrol.* 290, 137-151. <https://doi.org/10.1016/j.jhydrol.2003.12.001>.
- 1750 Trauerstein, M., Norton, K.P., Preusser, F., Schlunegger, F., 2013. Climatic imprint on landscape
 1751 morphology in the western escarpment of the Andes. *Geomorphology* 194, 76-83.
 1752 <http://dx.doi.org/10.1016/j.geomorph.2013.04.015>.
- 1753 Trauerstein, M., Lowick, S.E., Preusser, F., Schlunegger, F., 2014. Small aliquot and single grain
 1754 IRSL and post-IR IRSL dating of fluvial and alluvial sediments from the Pativilca valley, Peru.
 1755 *Quat. Geochron.* 22, 163-174. <http://dx.doi.org/10.1016/j.quageo.2013.12.004>.
- 1756 Tucker, G.E., Slingerland, R., 1997. Drainage basin responses to climate change. *Wat. Res. Res.* 33,
 1757 2031-2047. <https://doi.org/10.1029/97WR00409>
- 1758 Vandermaelen, N., Vanacker, V., Clapuyt, F., Christl, M., Beerten, K., 2022a. Reconstructing the
 1759 depositional history of Pleistocene fluvial deposits based on grain size, element geochemistry
 1760 and in-situ ¹⁰Be data. *Geomorphology* 402, 108127.
 1761 <https://doi.org/10.1016/j.geomorph.2022.108127>.
- 1762 Vandermaelen, N., Beerten, K., Clapuyt, F., Christl, M., Vanacker, V., 2022b. Constraining the
 1763 aggradation mode of Pleistocene river deposits based on cosmogenic radionuclide depth

1764 profiling and numerical modelling. *Geochronology* 4, 713-730.
1765 <https://doi.org/10.5194/gchron-4-713-2022>.

1766 Vanacker, V. von Blanckenburg, F., Govers, G., Molina, A., Campforts, B., Kubik, P., 2015.
1767 Transient river response, captured by channel steepness and concavity. *Geomorphology* 228,
1768 234-243. <https://doi.org/10.1016/j.geomorph.2014.09.013>.

1769 Veit, H., May, J.-H., Madella, A., Delunel, R., Schlunegger, F., Szidat, S., Capriles, J.M., 2016.
1770 Palaeo-geoecological significance of Pleistocene trees in the Lluta Valley, Atacama Desert. *J.*
1771 *Quat. Sci.* 31, 203-213. <https://doi.org/10.1002/jqs.2857>.

1772 Von Blanckenburg, F., 2005. The control mechanisms of erosion and weathering at basin scale from
1773 cosmogenic nuclides in river sediment. *Earth Planet Sci. Lett.* 237, 462-479.
1774 <https://doi.org/10.1016/j.epsl.2005.06.030>.

1775 Viveen, W., Schoorl, J.M., Veldkamp, A., van Balen, R.T., Vidal-Romani, R., 2013. Fluvial terraces
1776 of the northwest Iberian lower Miño River. *J. Maps* 9, 513-522.
1777 <http://dx.doi.org/10.1080/17445647.2013.821096>.

1778 Viveen, W., Schlunegger, F., 2018. Prolonged extension and subsidence of the Peruvian forearc
1779 during the Cenozoic. *Tectonophysics* 730, 48-62. <https://doi.org/10.1016/j.tecto.2018.02.018>.

1780 Viveen, W., Zevallos-Valdivia, L., Sanjurjo-Sanchez, J. 2019. The influence of centennial-scale
1781 variations in the South American summer monsoon and base-level fall on Holocene fluvial
1782 systems in the Peruvian Andes. *Global Planet. Change* 176, 1-22.
1783 <https://doi.org/10.1016/j.gloplacha.2019.03.001>.

1784 Viveen, W., Baby, P., Hurtado Enriquez, C.H., 2021. Assessing the accuracy of combined DEM-
1785 based lineament mapping and the normalized SL-index as a tool for active fault mapping.
1786 *Tectonophysics* 813, 228942. <https://doi.org/10.1016/j.tecto.2021.228942>.

1787 Viveen, W., Sanchez-Sanjurjo, J., Rosas, M.A., Vanacker, V., Villegas-Lanza, J.C., 2022. Heinrich
1788 events and tectonic uplift as possible drivers for late Quaternary fluvial dynamics in the western
1789 Peruvian Andes. *Global Planet Change*, 218, 103972.
1790 <https://doi.org/10.1016/j.gloplacha.2022.103972>.

1791 Waelbroeck, C., Labeyrie, L., Michel, E., Duplessy, J.C., McManus, J.F., Kambeck, K., Balbon, E.,
1792 Labracherie, M., 2002. Sea-level and deep water temperature changes derived from benthic
1793 foraminifera isotopic records. *Quat. Sci. Rev.* 21, 295-305. [https://doi.org/10.1016/S0277-](https://doi.org/10.1016/S0277-3791(01)00101-9)
1794 [3791\(01\)00101-9](https://doi.org/10.1016/S0277-3791(01)00101-9).

1795 Wegmann, K.W., Pazzaglia, F.J., 2009. Late Quaternary fluvial terraces of the Romagna and Marche
1796 Apennines, Italy: Climatic, lithologic, and tectonic controls on terrace genesis in an active
1797 orogen. *Quat. Sci. Rev.* 1-2, 137-165. <https://doi.org/10.1016/j.quascirev.2008.10.006>.

1798 Weldon, R.J. II, 1986. *The Late Cenozoic Geology of Cajon Pass; Implications for Tectonics and*
1799 *Sedimentation along the San Andreas Fault*. PhD thesis, Cal. Tech, California, USA.
1800 [doi:10.7907/9WJY-2A97. https://resolver.caltech.edu/CaltechETD:etd-08302006-135307](https://resolver.caltech.edu/CaltechETD:etd-08302006-135307)

1801 Whipple, K.X., Parker, G., Paola, C, Mohrig, D, 1998. Channel Dynamics, Sediment Transport, and
1802 the Slope of Alluvial Fans: Experimental Study. *J. Geol.* 106, 677-693.

1803 Wipf, M.A., 2006. Evolution of the Western Cordillera and coastal margin of Peru: evidence
1804 from low - temperature thermochronology and geomorphology. PhD thesis ETH. 16383,
1805 152 p. doi:10.3929/ethz - a - 005146374.

1806 Wolman, M.G., 1954. A method of sampling coarse riverbed material, Eos Trans. AGU, 35, 951–
1807 956.

1808 Wong, M., Parker,G., 2006. Reanalysis and Correction of Bed-Load Relation of Meyer-Peter and
1809 Müller Using Their Own Database. J. Hydraulic. Eng. 132, 1159-1168.
1810 [https://doi.org/10.1061/\(ASCE\)0733-9429\(2006\)132:11\(1159\)](https://doi.org/10.1061/(ASCE)0733-9429(2006)132:11(1159)).

1811 Wörner, G., Uhlig, D., Kohler, I., Seyfried, H., 2002. Evolution of the West Andean Escarpment at
1812 18°S (N. Chile) during the last 25 Ma: uplift, erosion and collapse through time.
1813 Tectonophysics 345, 183–198. [https://doi.org/10.1016/S0040-1951\(01\)00212-8](https://doi.org/10.1016/S0040-1951(01)00212-8).

1814

1815

1816

Valley	Sample Numbe	Easting	Northing
Pisco	PSC4	-13.592	-75.360
Pisco	PSC5	-13.610	-75.416
Pisco	PSC6	-13.611	-75.429
Pisco	PSC7	-13.608	-75.452
Pisco	PSC8	-13.567	-75.525
Pisco	PSC9	-13.567	-75.537
Pisco	PSC11	-13.596	-75.591
Pisco	PSC12	-13.596	-75.591
Pisco	PSC13	-13.598	-75.593
Pisco	PSC14	-13.596	-75.593
Pisco	PSC15	-13.595	-75.593
Pisco	PSC16	-13.598	-75.602
Pisco	PSC17	-13.599	-75.603
Pisco	PSC18	-13.644	-75.730
Pisco	PSC19	-13.643	-75.731
Pisco	PSC22	-13.643	-75.729
Pisco	PSC26	-13.648	-75.728
Pisco	PSC27	-13.649	-75.729
Pisco	PSC28	-13.652	-75.730
Pisco	PSC29	-13.651	-75.729
Pisco	PSC30	-13.675	-75.793
Pisco	PSC31	-13.678	-75.789
Pisco	PSC32	-13.678	-75.789
Pisco	PSC33	-13.681	-75.789
Pisco	PSC34	-13.681	-75.788
Pisco	PSC35	-13.731	-75.885
Pisco	PSC37	-13.726	-75.884
Pisco	PSC38	-13.694	-76.018
Majes	MAJ1	-15.854	-72.446
Majes	MAJ2	-15.873	-72.457
Majes	MAJ3	-15.925	-72.488
Majes	MAJ4	-15.931	-72.467
Majes	MAJ5	-15.934	-72.467
Majes	MAJ6	-15.989	-72.490
Majes	MAJ7	-15.990	-72.492
Majes	MAJ8	-15.999	-72.475
Majes	MAJ9	-16.234	-72.485
Majes	MAJ10	-16.017	-72.481
Majes	MAJ11	-16.013	-72.482
Majes	MAJ12	-15.850	-72.431
Majes	MAJ14	-15.844	-72.435
Majes	MAJ15	-15.842	-72.448
Majes	MAJ16	-15.844	-72.441
Majes	MAJ17	-15.895	-72.467
Majes	MAJ19	-16.305	-72.445

Majes	MAJ20	-16.285	-72.441
Lluta	VEC 06/35	-18.402	-70.016
Lluta	VEC 06/39	-18.403	-70.014
Lluta	VEC 06/36	-18.404	-70.014
Lluta	VEC 06/37B	-18.404	-70.014
Lluta	VEC 06/38	-18.404	-70.014
Lluta	VEC 06/34A	-18.406	-70.009
Lluta	VEC 06/34B	-18.406	-70.009
Lluta	VEC 06/33	-18.408	-70.005
Lluta	VEC 06/30	-18.409	-70.003
Lluta	VEC 06/32	-18.409	-70.003
Lluta	LVW-1	-18.451	-70.059
Lluta	LVW-2	-18.404	-70.035
Lluta	LVW-3	-18.400	-70.021
Lluta	LVW-4	-18.403	-70.016
Lluta	LVW-5	-18.405	-70.010
Lluta	LVW-6	-18.406	-70.010
Lluta	LVW-7	-18.395	-69.964
Rimac/Lima	LIM-IS1	-12.121	-77.044
Rimac/Lima	LIM-IS3	-12.121	-77.044
Pativilca	PAT-DP	-10.704	-77.775
Pativilca	PA01°	-10.674	-77.720
Pativilca	PA05°	-10.740	-77.787
Pativilca	PA06°	-10.545	-77.243
Pativilca	PA09°	-10.764	-77.761
Pativilca	PA10°	-10.775	-77.755
Pativilca	PA11°	-10.769	-77.751
Cañete	Cañete-1**	-13.153	-76.375
Cañete	Cañete-2*	-13.016	-76.168
Cañete	Cañete-3***	-13.020	-76.181
Cañete	Cañete-4''	-13.028	-76.190
Cañete	Cañete-5*	-13.028	-76.193
Cañete	Cañete-6*	-13.072	-76.237
Cañete	Cañete-7*	-12.977	-76.158
Cañete	Cañete-8*	-12.941	-76.125
Cañete	Cañete-9*	-13.125	-76.324
Chuquibamba landslide	11A39°*	-15.914	-72.545
Chuquibamba landslide	11A40°*	-15.912	-72.544
Chuquibamba landslide	11A41°*	-15.909	-72.549

Chuquibamba landslide	11A42°*	-15.907	-72.554
Chuquibamba landslide	11A43°*	-15.885	-72.576
Acroy megafan, Majes valley	11A28	-16.009	-72.489

*Ages base on the Central Age Model (CAM); they are corrected for fading and reportet

**CAM age is not corrected for fading

***Minimum Age Model.

°*Original coordinates of Margirier et al. (2015) were recalculated as their values did not

°**The age calculations considered a correction for surface erosion (0.21 mm/yr) and 6%

°***External uncertainties

°CAM ages, corrected for fading

'This sample was not used by Viveen et al. (2022) because it yielded unreliable ages for a

Ages (Ka)	Uncertainties (\pm Ka)	Method
49.4	2.8	IRSL measurements of bulk feldspar grain
27.8	1.6	IRSL measurements of bulk feldspar grain
22.6	1.3	IRSL measurements of bulk feldspar grain
11.7	0.9	IRSL measurements of bulk feldspar grain
38.2	2.5	IRSL measurements of bulk feldspar grain
26.9	1.7	IRSL measurements of bulk feldspar grain
39.2	3.3	IRSL measurements of bulk feldspar grain
45.8	2.9	IRSL measurements of bulk feldspar grain
22.3	2.0	IRSL measurements of bulk feldspar grain
4.9	0.3	IRSL measurements of bulk feldspar grain
26.5	1.6	IRSL measurements of bulk feldspar grain
9.8	0.6	IRSL measurements of bulk feldspar grain
25.0	1.5	IRSL measurements of bulk feldspar grain
54.0	3.5	IRSL measurements of bulk feldspar grain
46.0	3.0	IRSL measurements of bulk feldspar grain
10.2	0.8	IRSL measurements of bulk feldspar grain
50.4	3.4	IRSL measurements of bulk feldspar grain
17.9	1.2	IRSL measurements of bulk feldspar grain
16.0	1.1	IRSL measurements of bulk feldspar grain
7.4	0.6	IRSL measurements of bulk feldspar grain
51.9	3.4	IRSL measurements of bulk feldspar grain
34.6	3.8	IRSL measurements of bulk feldspar grain
9.1	0.9	IRSL measurements of bulk feldspar grain
48.0	2.9	IRSL measurements of bulk feldspar grain
53.3	3.2	IRSL measurements of bulk feldspar grain
47.7	2.9	IRSL measurements of bulk feldspar grain
7.0	0.5	IRSL measurements of bulk feldspar grain
51.5	2.9	IRSL measurements of bulk feldspar grain
3.2	0.3	IRSL measurements of bulk feldspar grain
23.0	1.0	IRSL measurements of bulk feldspar grain
8.5	0.7	IRSL measurements of bulk feldspar grain
51.2	3.4	IRSL measurements of bulk feldspar grain
59.7	3.6	IRSL measurements of bulk feldspar grain
107.0	5.0	IRSL measurements of bulk feldspar grain
7.9	0.6	IRSL measurements of bulk feldspar grain
101.6	4.9	IRSL measurements of bulk feldspar grain
6.4	0.4	IRSL measurements of bulk feldspar grain
1.8	0.1	IRSL measurements of bulk feldspar grain
9.6	0.7	IRSL measurements of bulk feldspar grain
56.7	7.8	IRSL measurements of bulk feldspar grain
12.0	1.2	IRSL measurements of bulk feldspar grain
10.7	0.5	IRSL measurements of bulk feldspar grain
8.0	0.6	IRSL measurements of bulk feldspar grain
12.9	0.6	IRSL measurements of bulk feldspar grain
61.1	8.7	IRSL measurements of bulk feldspar grain

41.2	5.9	IRSL measurements of bulk feldspar grain
23.9	0.1	14C age of leaves
0.5	0.0	14C age of reed
18.3	0.1	14C age of leaves
28.9	0.1	14C age of leaves
37.1	0.4	14C age of wood
19.4	0.1	14C age of leaves
19.5	0.1	14C age of wood
15.6	0.2	14C age of leaves
15.4	0.4	14C ages of TOC fAh
16.1	0.1	14C ages of leaves
35.0	0.3	14C age of wood
16.7	0.6	14C age of wood
22.0	0.3	14C age of wood
30.0	0.3	14C age of wood
27.8	0.4	14C age of wood
19.4	0.5	14C age of wood
18.0	0.2	14C age of wood
490.0	80.0	26Al/10Be isochron burial age
490.0	70.0	26Al/10Be isochron burial age
200.0	86.0	10Be depth profile age
128.0	13.0	IRSL(50) signals of small aliquot of feldspar
99.0	16.0	IRSL(50) signals of small aliquot of feldspar
101.0	17.0	IRSL(50) signals of small aliquot of feldspar
99.0	20.0	IRSL(50) signals of small aliquot of feldspar
102.0	18.0	IRSL(50) signals of small aliquot of feldspar
116.0	36.0	IRSL(50) signals of small aliquot of feldspar
102.0	6.0	pIR IRSL(225) signals of feldspar grains
43.0	4.0	IRSL(180) signals of feldspar grains
48.0	4.0	IRSL(110) signals of feldspar grains
0.8	0.1	IRSL(180) signals of feldspar grains
31.0	3.0	IRSL(180) signals of feldspar grains
37.0	3.0	IRSL(110) signals of feldspar grains
22.0	2.0	IRSL(180) signals of feldspar grains
28.0	2.0	IRSL(110) signals of feldspar grains
11.0	1.0	IRSL(180) signals of feldspar grains
14.0	1.0	IRSL(110) signals of feldspar grains
26.0	2.0	IRSL(180) signals of feldspar grains
29.0	3.0	IRSL(110) signals of feldspar grains
29.0	3.0	IRSL(180) signals of feldspar grains
23.0	2.0	IRSL(110) signals of feldspar grains
14.0	1.0	IRSL(180) signals of feldspar grains
12.0	1.0	IRSL(110) signals of feldspar grains
96.1	8.9 ^{***}	10Be exposure age ^{***}
102.9	9.5 ^{***}	10Be exposure age ^{***}
108.5	10.2 ^{***}	10Be exposure age ^{***}

97.9	9.2 ^{***}	10Be exposure age ^{***}
106.9	11.5 ^{***}	10Be exposure age ^{***}
105.3	10.2 ^{***}	10Be exposure age ^{***}

with a 1σ uncertainty.

: correspond with the sites displayed in their Figure 5.

6 and 8% in the production rate and 10Be decay constant, respectively

ll (pIR) signals. Yet for the sake of completeness, we included this age in Figure 8.

is

Steffen et al. (2010)

Veit et al. (2016)

Litty et al. (2018; ESPL)

Litty et al. (2018; ESPL)

Litty et al. (2018; Geomorphology)

ar grains

Trauerstein et al. (2014)

Viveen et al. (2022)

Margirier et al. (2015)

Figure 1

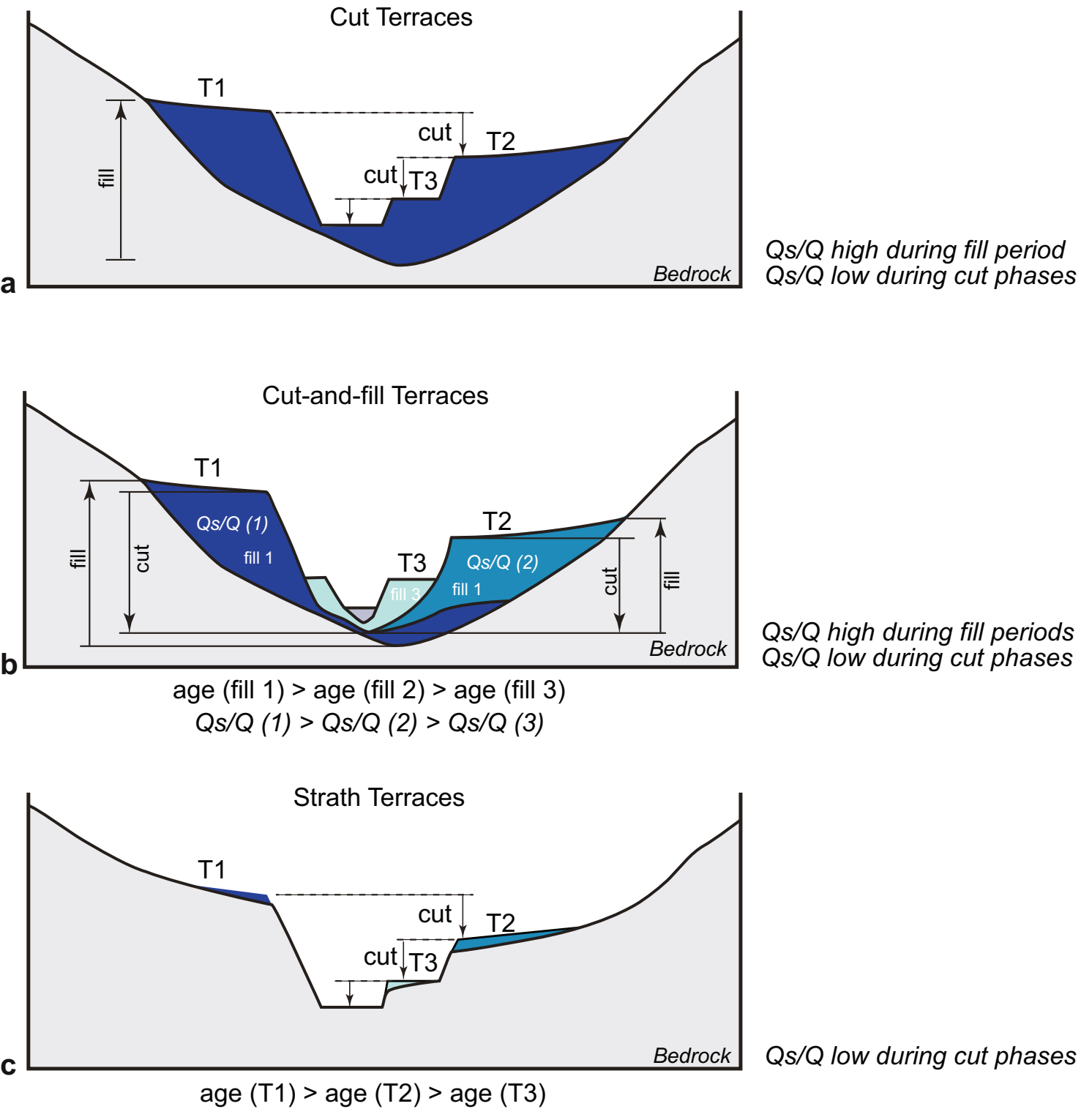


Figure 1

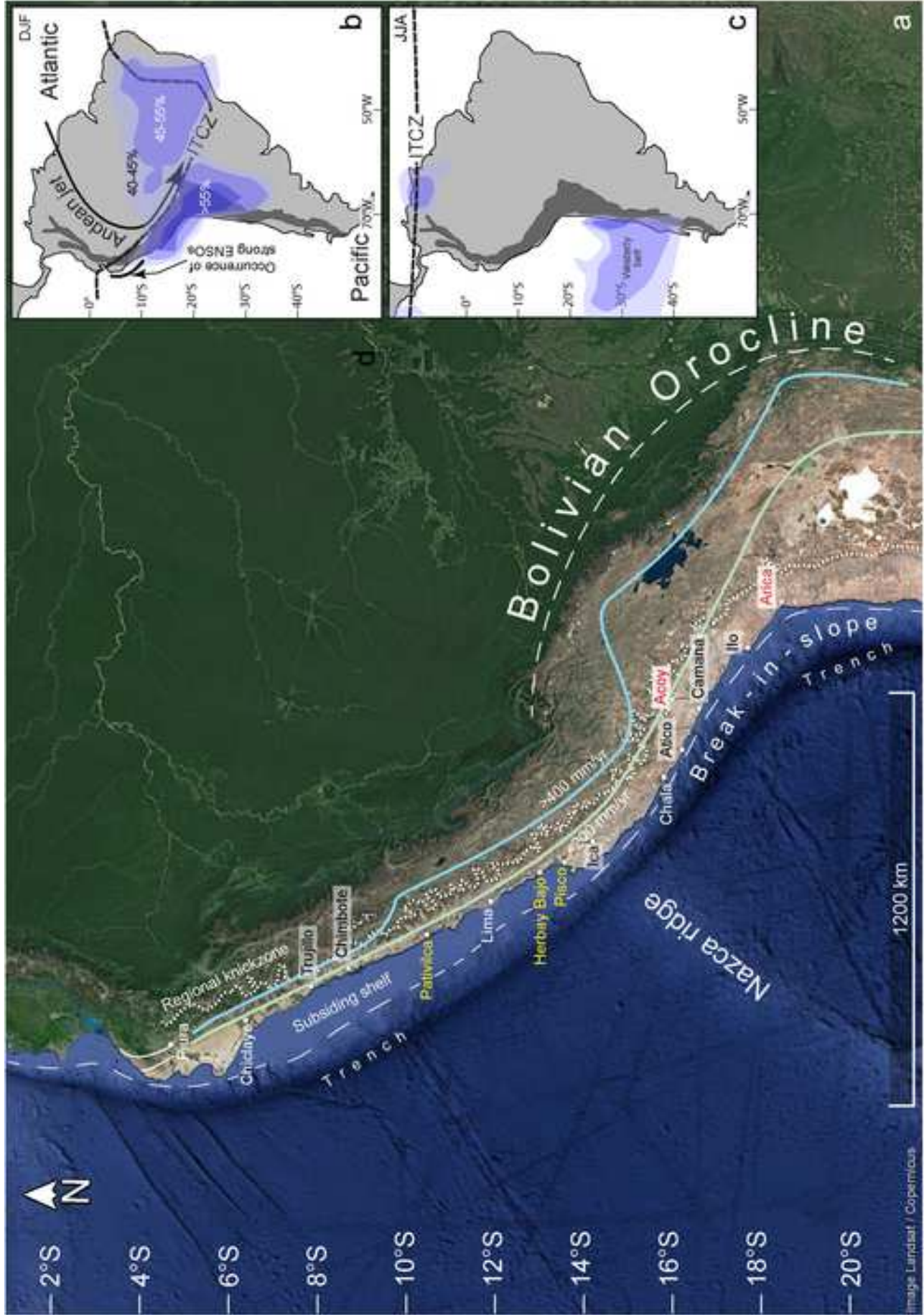


Figure 2

Image Landsat / Copernicus

Figure 3

[Click here to access/download;Figure \(Color\);Figure_3.jpg](#)



Figure 3

Figure 4

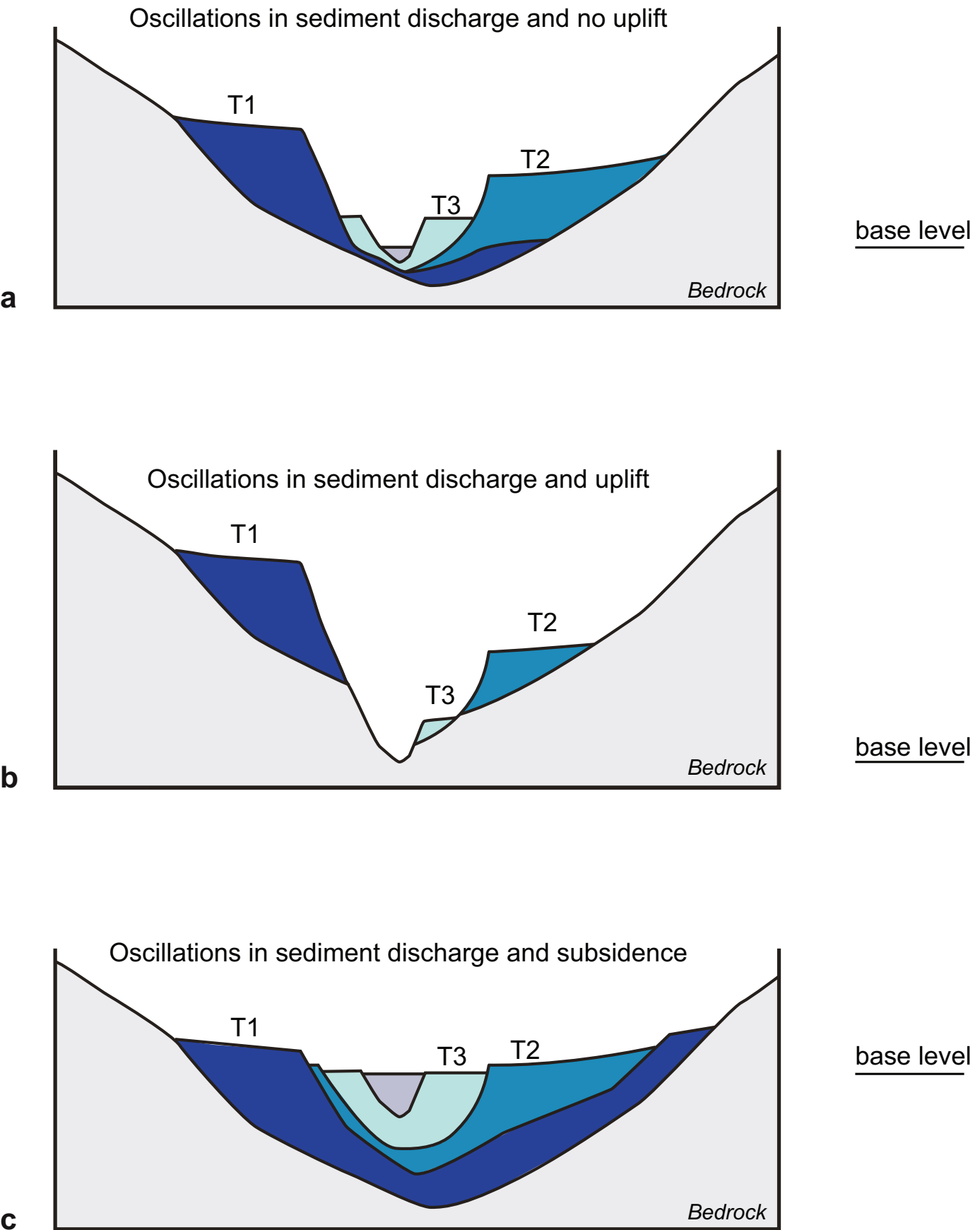


Figure 4

Figure 5

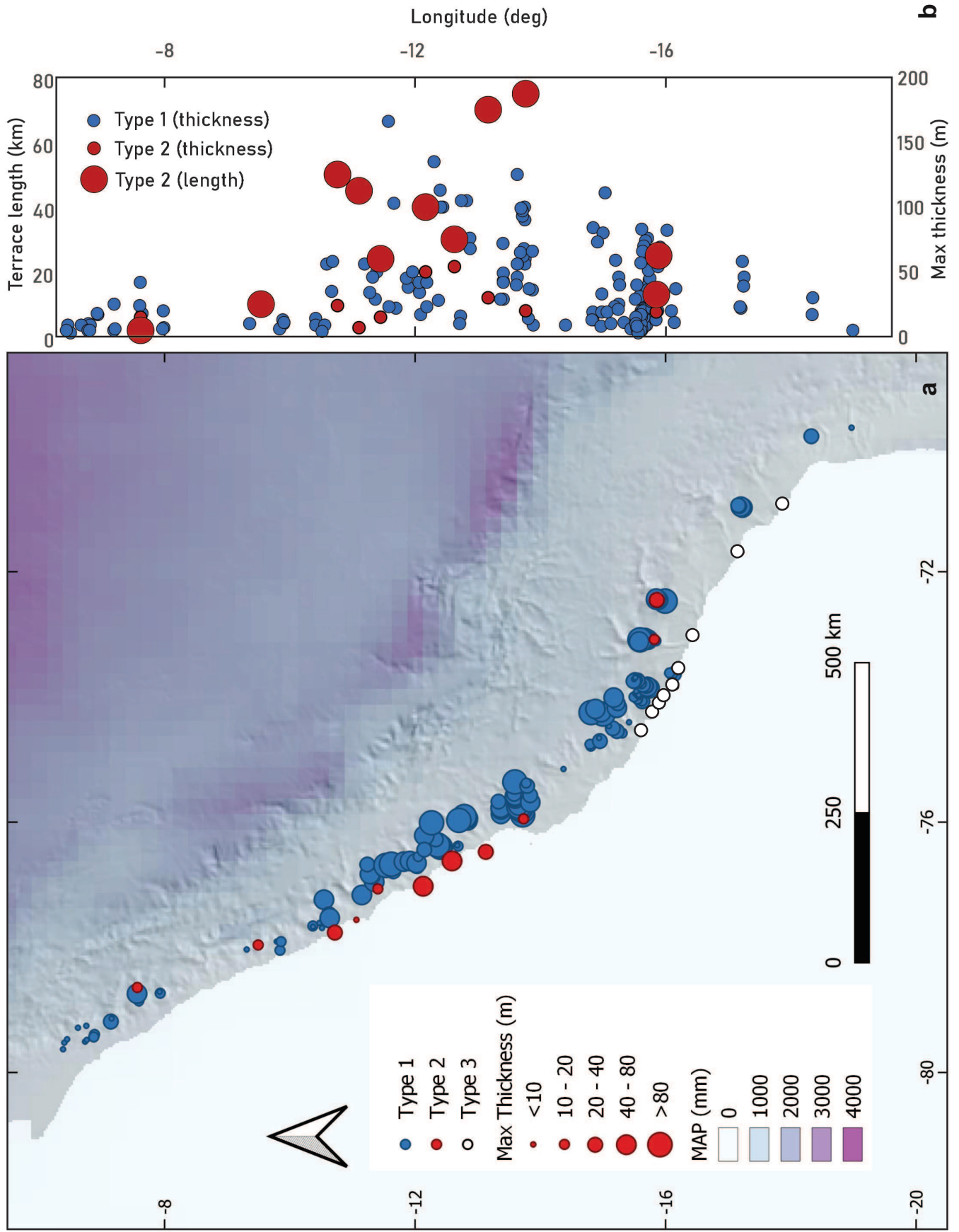
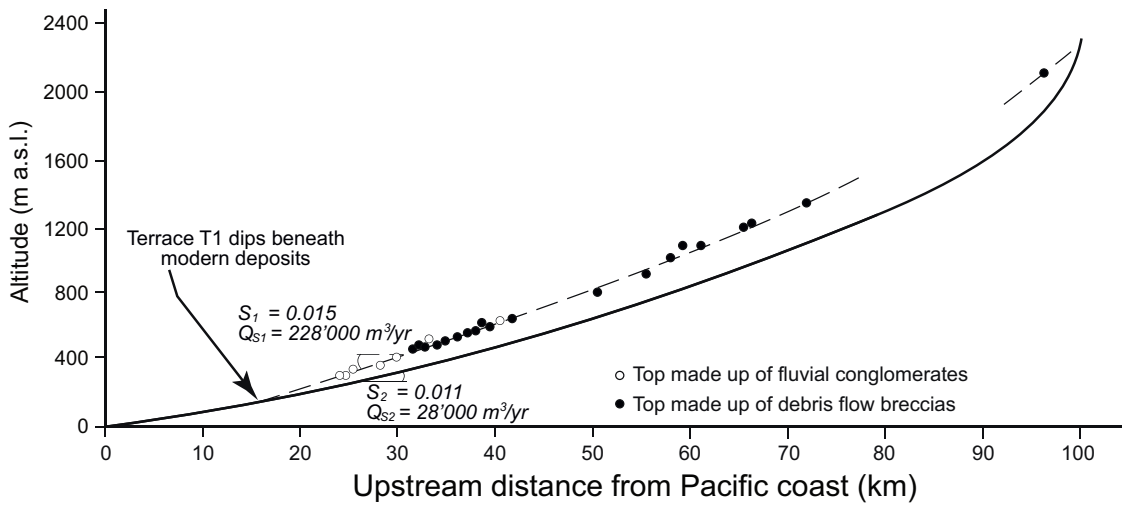
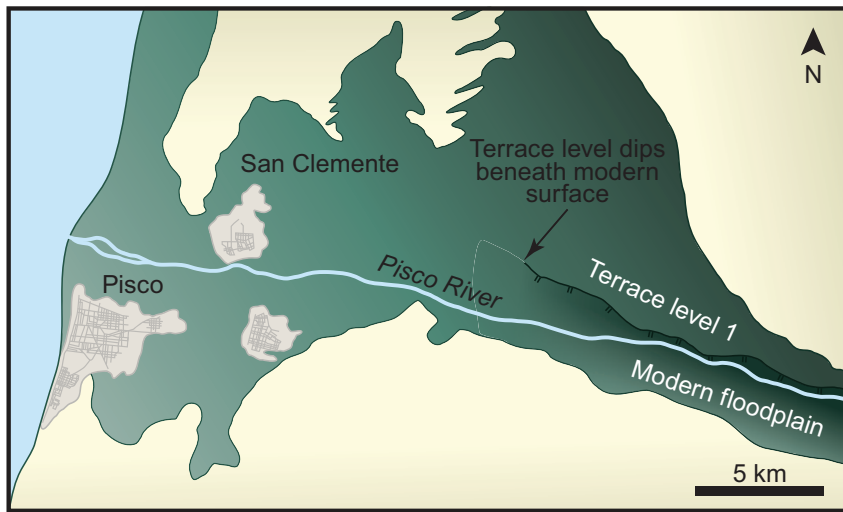


Figure 5

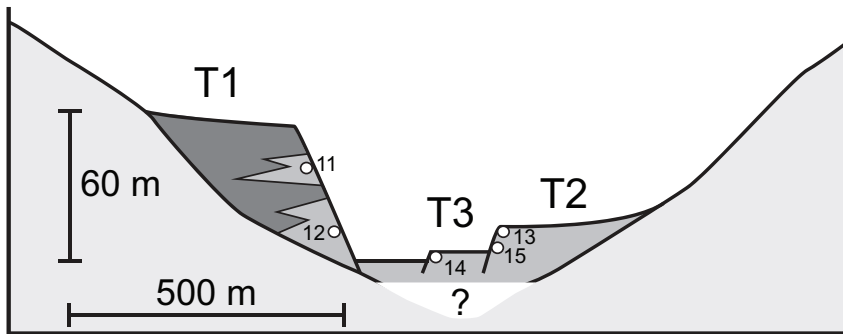
Figure 6



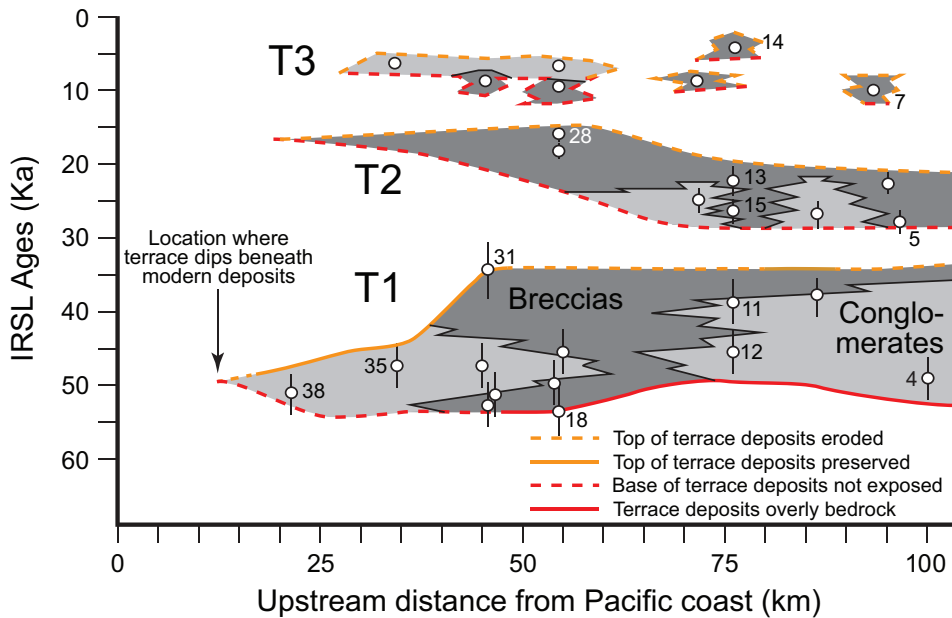
a



b



c



d

Figure 6

Figure 7

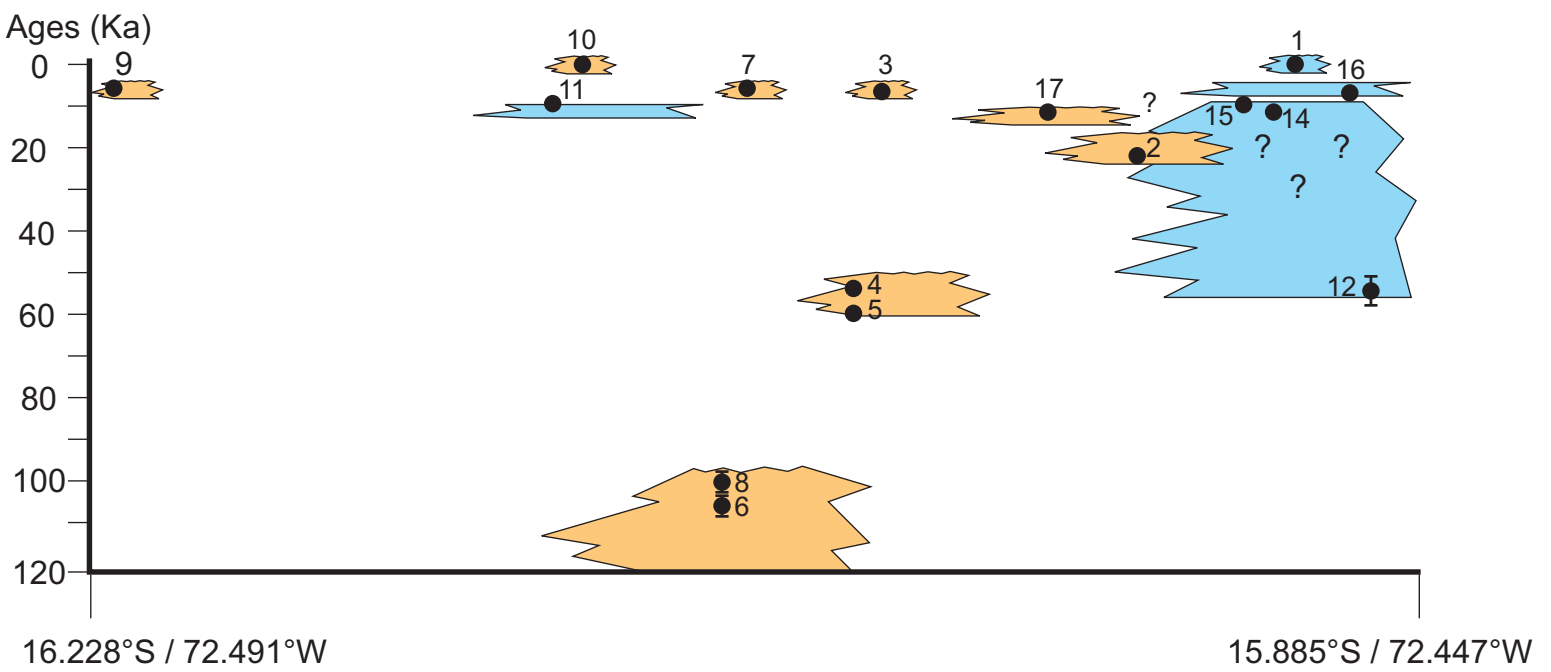
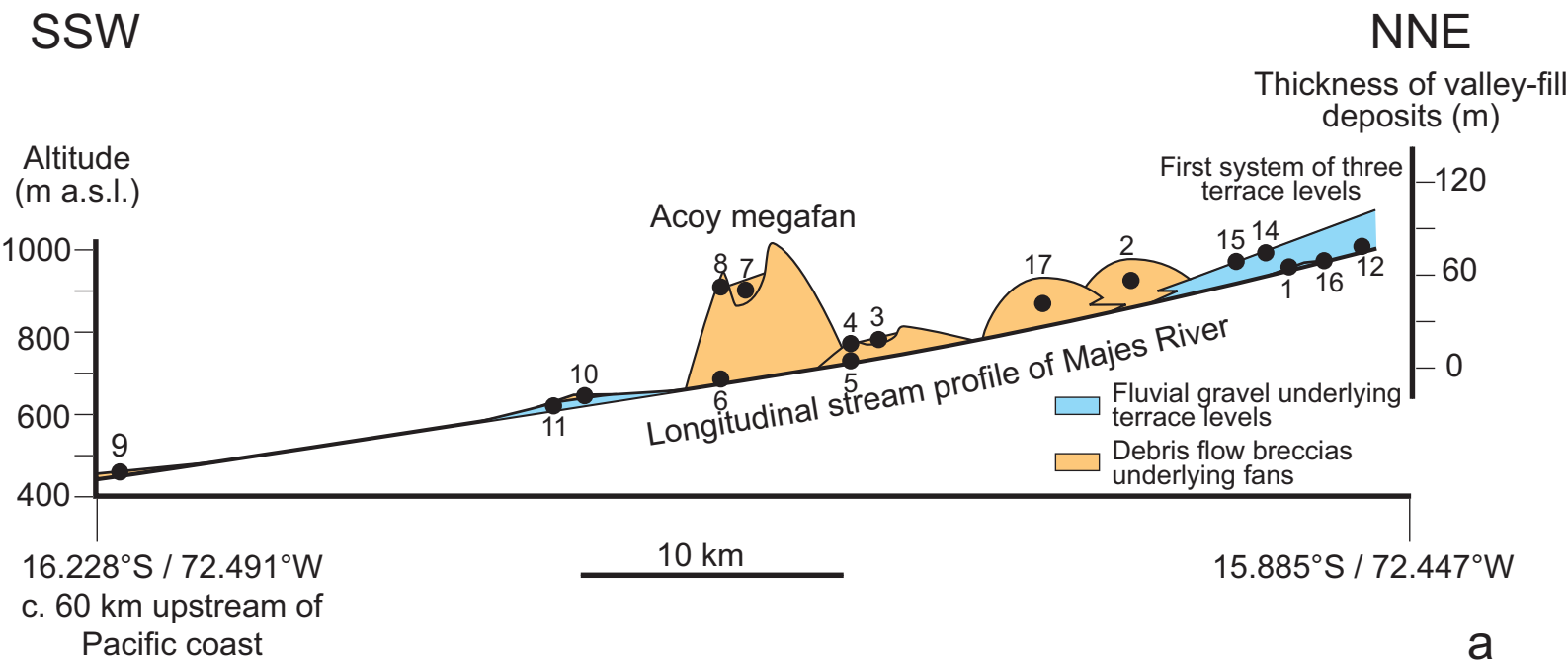


Figure 7

Figure 8 Lake level highstands on Altiplano

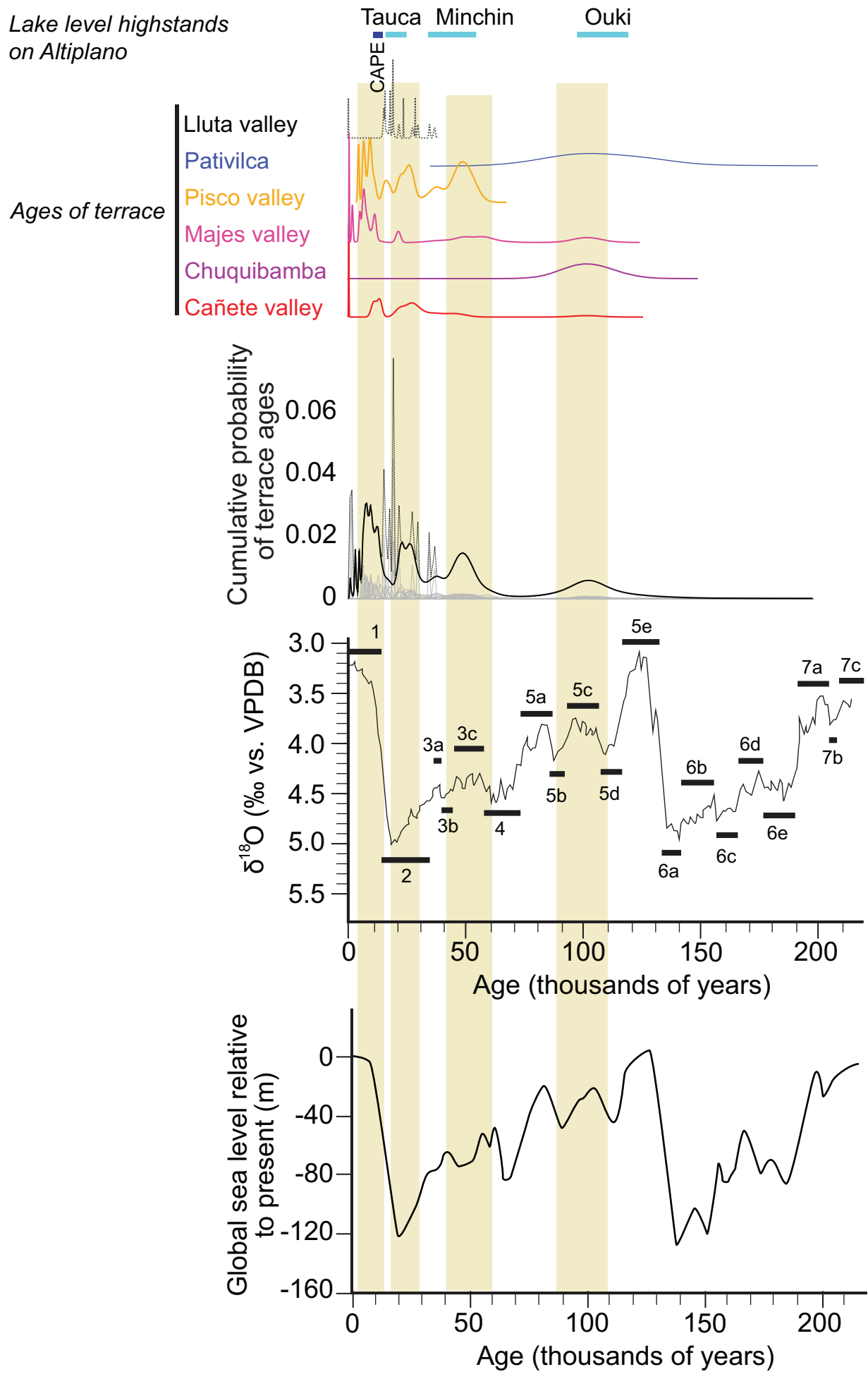
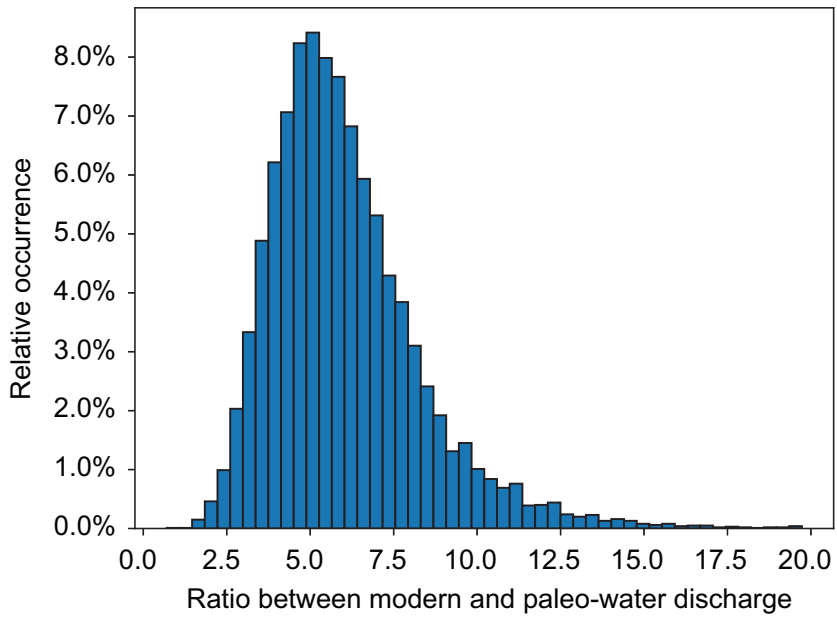
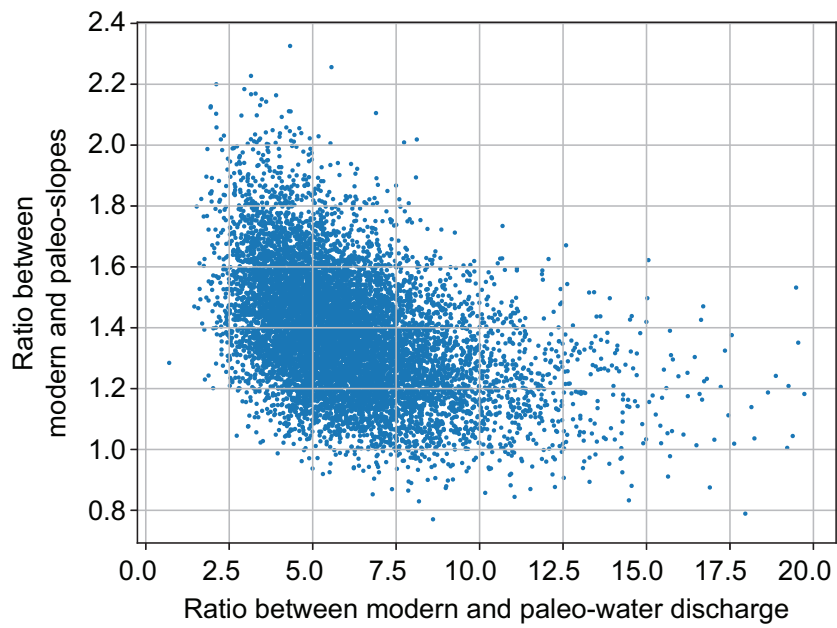


Figure 8

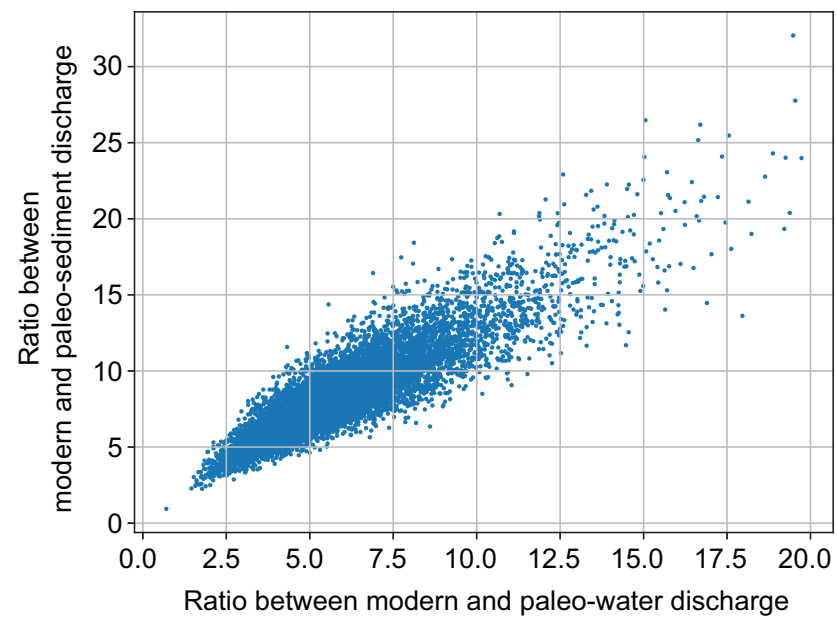
Figure 9



a



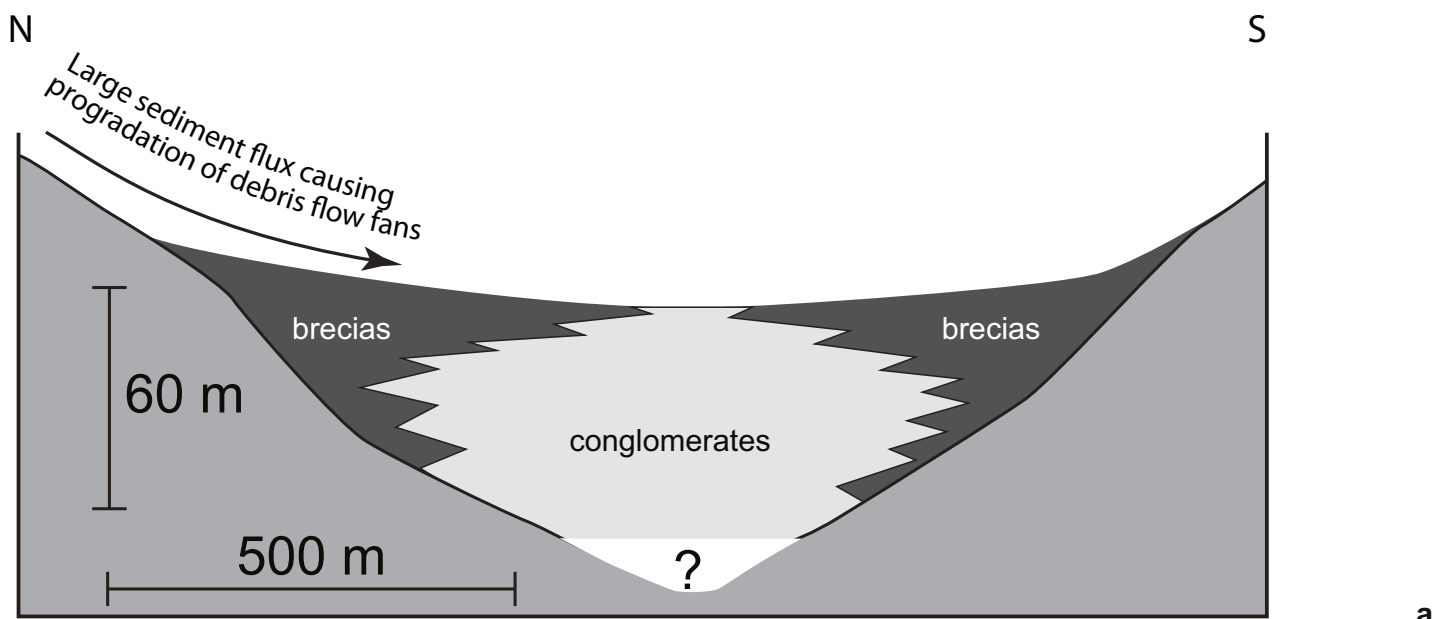
b



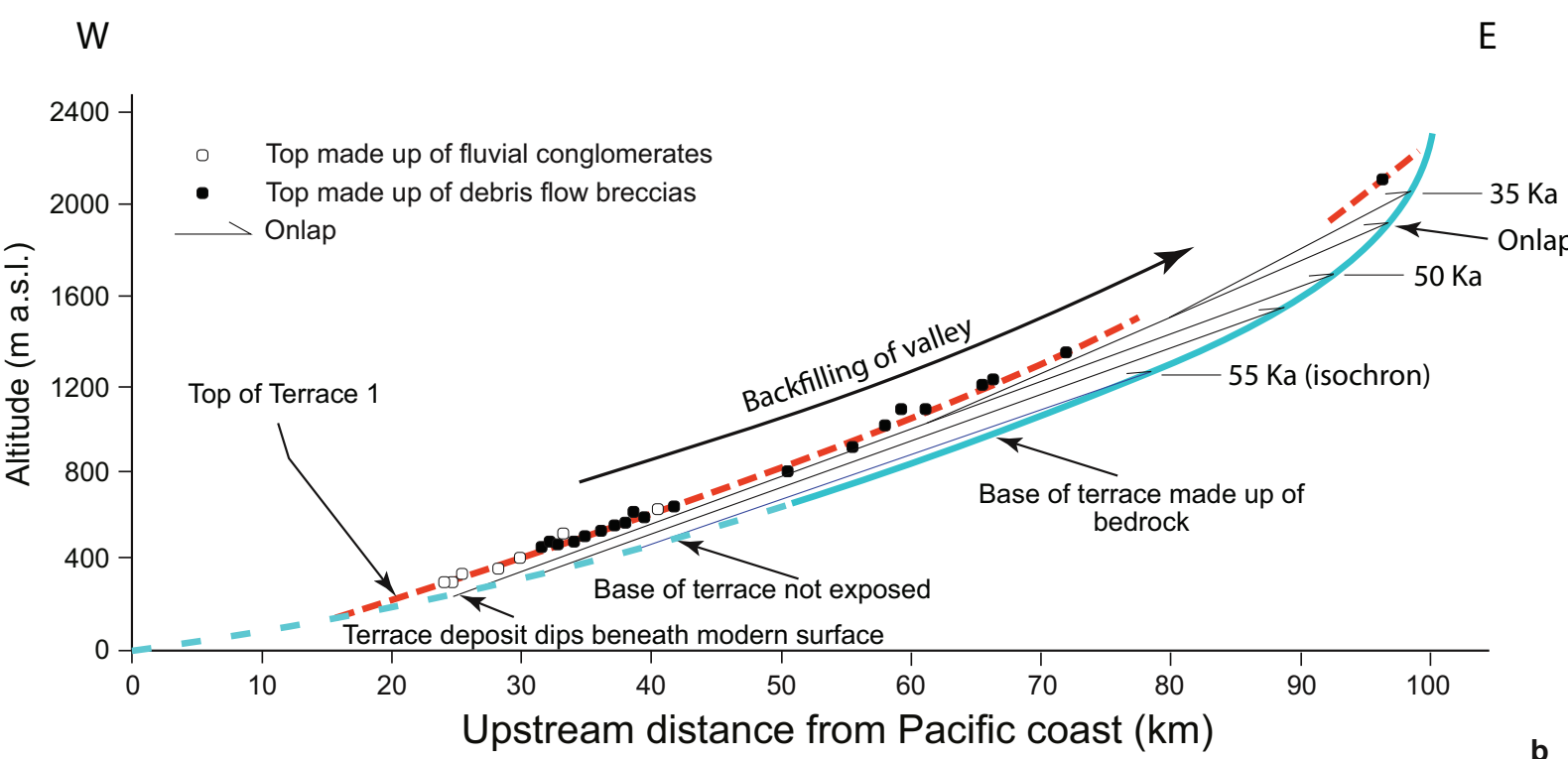
c

Figure 9

Figure 10



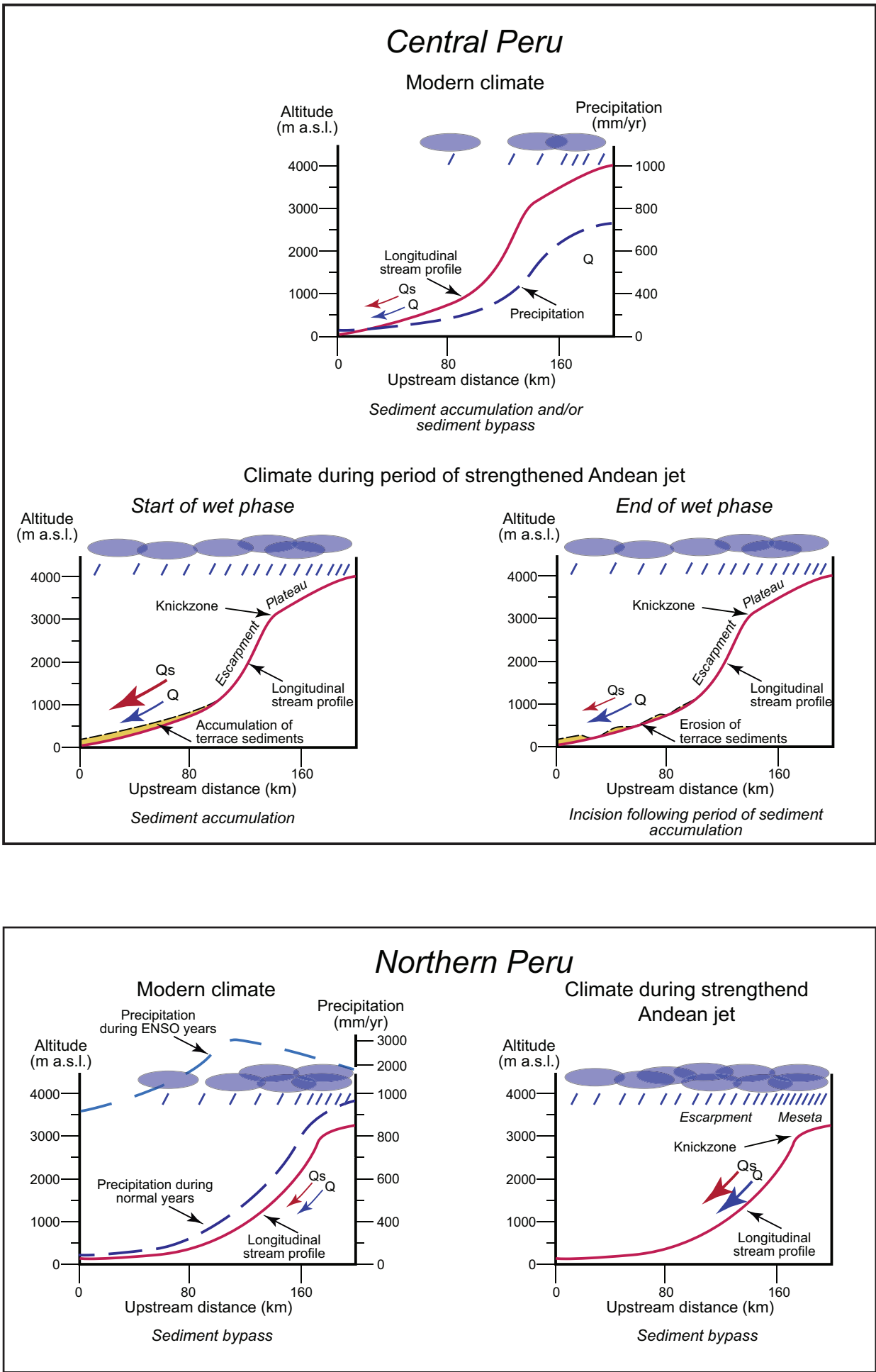
a



b

Figure 10

Figure 11



a

b

Figure 11

Figure 12

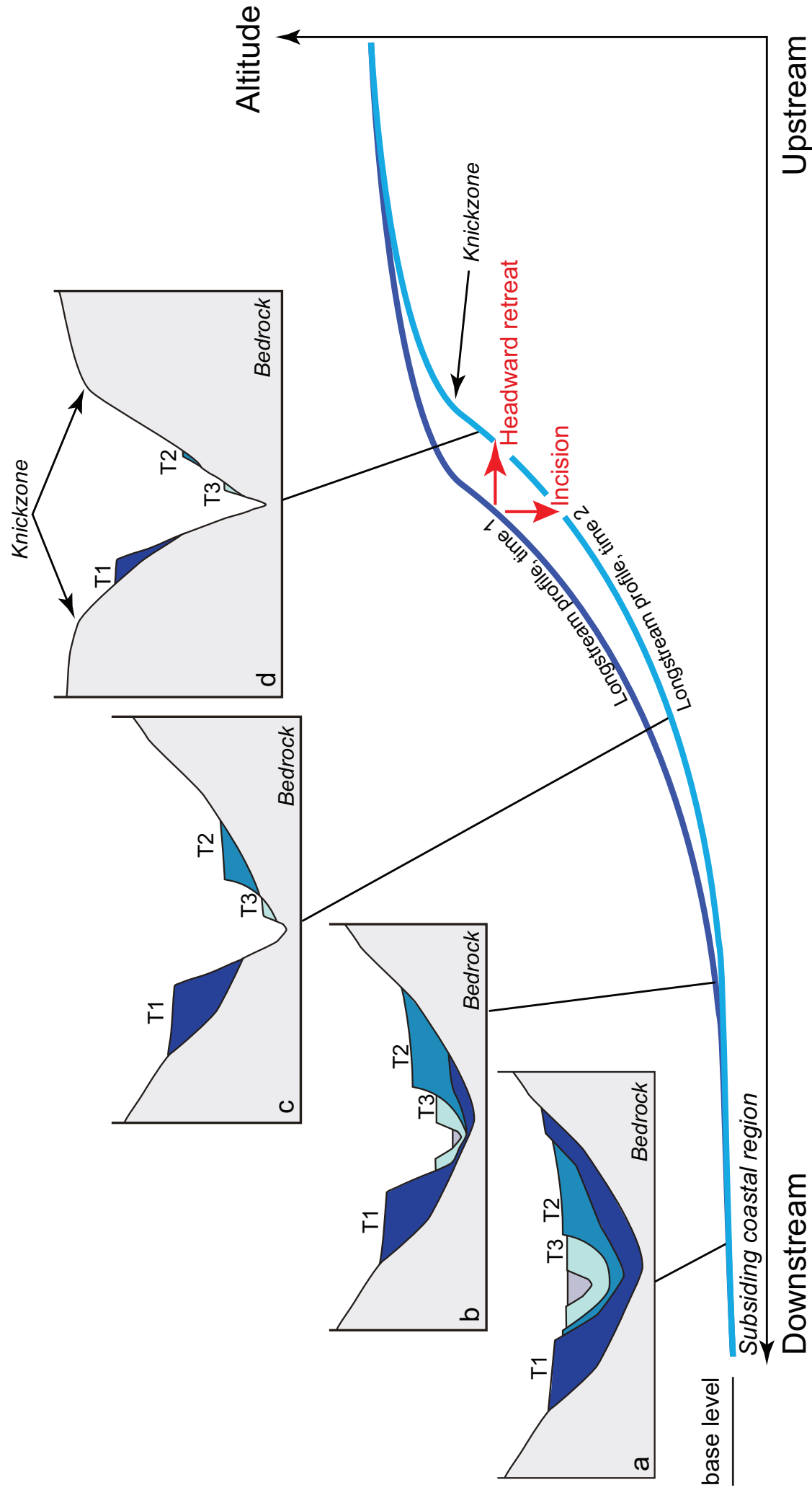


Figure 12



[Click here to access/download](#)

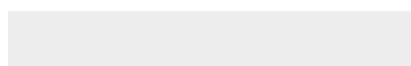
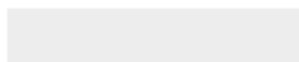
Supplementary material for online publication only
Supplimentary Files S1 and S2.eps

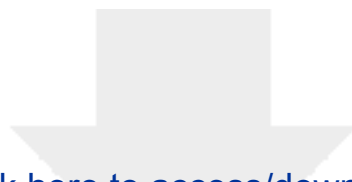




[Click here to access/download](#)

Supplementary material for online publication only
Supplementary File S3.eps





[Click here to access/download](#)

Supplementary material for online publication only
Supplementary Files S4 and S5.eps



Declaration of interests

The authors declare that they have no known competing financial interests or personal relationships that could have appeared to influence the work reported in this paper.

The authors declare the following financial interests/personal relationships which may be considered as potential competing interests:

Fritz Schlunegger reports financial support was provided by Swiss National Science Foundation. Fritz Schlunegger reports a relationship with Swiss National Science Foundation that includes: funding grants.